



ROMA TRE UNIVERSITY

Doctoral School in Engineering

**Section of Engineering of Biomedical Electronics,
Electromagnetism and Telecommunications**

PhD thesis : XXIII course

**Use of GPR techniques for Landmines
Detection and Road monitoring**

Célestin Twizere

A.A. 2010/2011

Supervisor: **Prof. Giuseppe Schettini**

Cordinator: **Prof. Lucio Vegni**

To Donatille, my beloved wife who encouraged me a lot and endured my absence.

To Lisa, my daughter for her silent encouragement and her innocence

Content

Introduction	1
Chapter 1: Ground Penetrating Radar and the Electromagnetic Scattering.....	4
1.1.Scattering of the electromagnetic waves by buried objects.....	4
1.1.1. Introduction.....	4
1.1.2.Geometry of the problem.....	5
1.1.3.Theoretical Analysis.....	7
1.2. The Finite Difference Time - Domain Method.....	18
1.2.1 Introduction.....	18
1.2.2 Finite difference time domain method.....	18
1.2.3 Yee's algorithm.....	21
1.2.4 Courant's condition	25
1.2.5 Numerical dispersion.....	26
1.2.6 Bérenger's PML	29
1.2.7 The FDTD simulation	30
1.3. Ground Penetrating Radar	31
1.3.1.Introduction	31
1.3.2 Physical base	34
1.3.3.Data acquisition	35
1.3.4. Soil dielectric properties	37
1.3.5 Penetration depth	43
1.3.6 Resolution	44
Chapter 2: FDTD Simulations and GPR Measurements for Land-Mine Detection.....	45
2.1.Introduction	45
2.2.FDTD Simulation of GPR Measurements in a Laboratory Sandbox	

for Landmine detection	47
2.2.1.Introduction	47
2.2.2.Simulation Setup	47
2.2.3. Results	50
2.3.GPR Measurements and Tree-dimensional FDTD Simulations.....	62
2.3.1.Introduction	62
2.3.2.Experimental Setup	63
2.3.3.Numerical Simulations	64
2.3.4.Results	66
Chapter 3: Evaluation of clay content in substrate and road foundation with GPR.....	75
3.1. Introduction	75
3.2. Materials and Methods	76
3.2.1.Acquisition of the starting material: the mixed of Magliana.....	77
3.2.2. Mixing Protocol	78
3.2.3.The density of reference: protocol compaction	78
3.2.4.Basic parameters of mixtures: particle size and limits	79
3.3. Results and Discussion	79
3.3.1. Analysis in Time Domain	80
3.3.2 Analysis in the frequency domain	86
3.2.5. The Trend of the spectrum	89
Chapter 4: Testing moisture with GPR for the stability of the road structure....	92
4.1.Introduction	92
4.2. Time Delay analysis in Time Domain	97
4.3.Amplitude analysis in Time domain	99

4.4. Frequency domain analysis	102
4.4.1. Rayleigh scattering	103
4.4.2. Refractive index and dielectric permittivity.....	104
4.4.3. The relaxation time	106
4.5. Evaluation of volumetric water content with GPR	107
4.5. 1. The road under investigation	108
4.5.2. Used ground penetrating radar	111
4.5.3. Modality of execution of GPR measurements.....	113
4.5.4 Data processing	114
4.5.6. Results and discussion	115
Conclusion	122
Bibliography	124

Introduzione in italiano

Il campo elettromagnetico, il cui comportamento è descritto dalle equazioni di Maxwell e le relazioni costitutive, può essere ottenuta utilizzando tre tipi di approcci non esclusivi: analitico, numerico e sperimentale. Il metodo analitico, ci fa sapere esattamente il valore del campo elettromagnetico, ma appena cresce la complessità del problema, le approssimazioni drastiche dobbiamo considerare se stessi riflettere sulla affidabilità risultato. Il Metodo sperimentale, d'altra parte, fornisce dati attendibili, salvo la precisione degli apparecchi, tuttavia, sono lunghi e costosi.

Infine, i metodi numerici offrono soluzioni la cui accuratezza è data dalla qualità dei modelli matematici utilizzati, in tempi ragionevoli e costi contenuti. Tra questi, ci sono due gruppi principali: i metodi nel dominio del tempo e metodi di dominio della frequenza. In questa tesi, abbiamo usato sia il metodo analitico/numerico, sia il metodo sperimentale per la conferma dei risultati ottenuti.

Il Ground Penetrating Radar (GPR) è entrato in uso negli ultimi 20 anni in ingegneria civile, geologia e archeologia, per la rilevazione di oggetti sepolti e per lo studio delle proprietà fisico-chimiche del suolo. Il rilevamento di mine sepolte è stato anche un tema di notevole interesse, in particolare a causa dei potenziali del GPR per l'individuazione delle mine con involucro di plastica che contengono poco metalli o niente. Oggi, un gran numero di organizzazioni stanno lavorando su sistemi GPR, e tra tutti i sensori proposti per lo sminamento umanitario; il GPR ha avuto di gran lunga il maggiore finanziamento della ricerca e dello sforzo ad esso dedicati.

In questa tesi abbiamo presentato lo scattering elettromagnetico da parte degli oggetti sepolti e sperimentalmente si è dimostrato l'uso delle tecniche GPR nel rilevamento delle mine e la verifica della presenza di materiale inquinante negli strati portanti della pavimentazione stradale. Il mezzo può essere assunto non dispersivo, lineare, omogeneo.

La principale applicazione di questo lavoro è quella della rivelazione di oggetti sepolti o della esplorazione e caratterizzazione del sottosuolo con tecniche elettromagnetiche, con particolare riferimento ai sistemi GPR-UWB (Ground Penetrating Radar- Ultra Wide Band) che utilizzano segnali a banda larga per i loro fini.

I sistemi GPR sfruttano i fenomeni di scattering che si producono per effetto dell'interazione tra l'energia elettromagnetica irradiata e le discontinuità del mezzo di propagazione: i dati rilevati, se ben interpretati, possono dare informazioni sulle caratteristiche elettriche e magnetiche del terreno e sulle dimensioni e sulla disposizione di oggetti ivi sepolti.

L'antenna di un sistema GPR-UWB irradia un segnale di durata compresa tra 0.1 e 50ns (la larghezza di banda è dell'ordine dei GHz). Importanti parametri caratteristici dei sistemi GPR sono la risoluzione e la profondità di penetrazione.

Per quanto riguarda le caratteristiche di risoluzione di questi sistemi, si possono distinguere una risoluzione verticale, che indica la capacità di riconoscere due oggetti a diversa profondità, ed una risoluzione orizzontale, che si riferisce all'abilità di rilevare separatamente due oggetti alla medesima distanza dalla superficie del sottosuolo.

L'azione che il terreno svolge sulla radiazione incidente è quella di operare un filtraggio passa basso del suo spettro: all'aumentare della frequenza il segnale penetra di meno nel terreno.

D'altra parte, però, avviene che la risoluzione migliora al crescere della frequenza. La scelta da effettuare per l'impulso d'eccitazione si fa di volta in volta in base alle specifiche del caso, cercando di coniugare il più possibile questi due aspetti contrastanti.

In questa tesi, lo scopo era quello di utilizzare sperimentalmente le tecniche GPR per la rilevazione delle mine e la verifica della presenza di materiale inquinante negli strati portanti della pavimentazione stradale.

Nel capitolo 1 dopo aver descritto brevemente lo scattering delle onde elettromagnetiche da oggetto sepolto, e il metodo delle differenze finite nel dominio del tempo (FDTD) che è un metodo numerico per risolvere le equazioni di Maxwell, abbiamo parlato del sistema GPR (Ground Penetrating Radar), che è la strumentazione utilizzata in tutti gli esperimenti in questa tesi. La prima sezione di questo capitolo è stata dedicata allo scattering delle onde elettromagnetiche da oggetto sepolto.

La seconda sezione analizza il metodo FDTD fornendo le formule che sono direttamente implementati nel programma di simulazione. È stato discusso anche su come il dominio computazionale è costruita, come i calcoli sono effettuati e quali sono le condizioni che rendono i risultati della simulazione affidabili.

La terza sezione analizza la teoria del sistema GPR e la sua applicazione principale nel rilevamento di mine e la verifica della presenza di materiale inquinante negli strati portanti della pavimentazione stradale con la teoria di come può essere possibile ottenere e risolvere alcuni parametri del segnale elettromagnetico come la costante dielettrica e umidità nel terreno.

Nel secondo capitolo, lo studio della rivelazione delle mine in un ambiente controllato si è basata sulle simulazioni in due e tre dimensioni con il programma GPRMax che implementa nel suo codice il metodo FDTD. Le misure con lo strumento GPR hanno completato lo studio per confermare le simulazioni. I confronti tra risultati delle simulazioni e misure GPR coincidono.

Nel terzo capitolo, dove ho fatto gli esperimenti nel laboratorio, ho studiato una valutazione del contenuto di argilla in sottofondo e fondazione stradale con GPR. In

questo capitolo si cerca di dimostrare sperimentalmente il metodo di calcolo della costante dielettrica in situazione di presenza di umidità nella pavimentazione stradale.

Il capitolo quattro è stato dedicato ad un esperimento realmente in una strada esistente in cui si valuta il tasso di umidità con GPR per la stabilità della struttura stradale. I risultati sono molto interessanti e possono essere una base di dati per la struttura viaria per i futuri studi in questo campo.

Publicazioni

1. M. Balsi, S. Esposito, F. Frezza, P. Nocito, L. Porrini L. Pajewski, G. Schettini, **C. Twizere**, FDTD Simulation of GPR Measurements in a Laboratory Sandbox for Landmine Detection, 5th International Workshop on Advanced Ground Penetrating Radar (*IWAGPR 2009*), 27 – 29 may, 2009, Granada, Spain
2. M. Balsi, S. Esposito, F. Frezza, P. Nocito, P. M. Barone, S. E. Lauro, E. Mattei, E. Pettinelli, G. Schettini, **C. Twizere**, GPR Measurements and FDTD Simulations for Landmine Detection, XIII International Conference on Ground Penetrating Radar, Lecce, 21 – 25 June 2010
3. M. Balsi, S. Esposito, F. Frezza, P. Nocito, P. M. Barone, S. E. Lauro, E. Mattei, E. Pettinelli, G. Schettini, **C. Twizere**, FDTD Simulations and GPR Measurements for Land-Mine Detection in a controlled Environment, XVIII RINEM, Benevento, 6th September 2010.
4. F. Tosti , **C. Twizere**, Potentiality of GPR for evaluation of clay content in soils, European Geosciences Union General Assembly 2011 (EGU2011), Vienna, Austria, 03 - 08/04/ 2011
5. A. Benedetto, F. Tosti, G. Schettini, **C. Twizere** Evaluation of geotechnical stability of road using GPR, 6th International Workshop on Advanced Ground Penetrating Radar 2011, Aachen, Germany.

Introduction

Electromagnetic field, whose behavior is described by Maxwell's equations and constitutive relations, can be obtained using three types of not exclusive approaches: analytical, numerical and experimental methods. Analytical methods let us know the exact field but, as soon as the complexity of the problem grows, the drastic approximations we need to consider reflect themselves on result's reliability. Experimental methods, on the other hand, provide us with reliable data, within the accuracy of the apparatus; however, they're time-consuming and expensive. Finally, numerical methods offer solutions whose accuracy is given by the quality of the used mathematical models, at reasonable time and cost. Among them, there are two main groups: time domain and frequency domain methods.

Ground Penetrating Radar (GPR) has come into use over the last 20 years in civil engineering, geology and archaeology, for the detection of buried objects and for soil study. The detection of buried landmines has also been a subject of considerable interest, in particular due to radar's potential for the detection of plastic-cased mines which contain little or no metal. Today, a large number of organizations are working on different parts of GPR systems, and among all the sensors proposed for humanitarian demining; GPR has had by far the greatest research funding and effort dedicated to it.

In this thesis we have presented an electromagnetic scattering by the buried object and experimentally we demonstrate to use of the GPR techniques in landmine detection and road monitoring. The medium can be assumed linear, homogeneous and non dispersive.

The main application of this thesis is that of detecting buried objects or the exploration and characterization of the subsurface electromagnetic techniques, with particular reference to the UWB-GPR (Ground Penetrating Radar-Ultra Wide Band) signals using broadband to their purposes.

Systems exploit the GPR scattering phenomena that occur as a result of the interaction between the electromagnetic energy radiated and discontinuities of the means of propagation: the data collected, if properly interpreted, can provide information on electrical and magnetic characteristics of the soil and size and layout of objects buried there.

The antenna of a UWB-GPR system radiates a signal of duration between 0.1 and 50 ns (the bandwidth is of the order of GHz). Important characteristic parameters of GPR systems are the resolution and depth of penetration.

Regarding the characteristics of resolution of these systems, we can see a vertical resolution, which is the ability to recognize two objects at different depths, and horizontal resolution, which refers to the ability to detect two separate objects at the same distance from surface of the soil.

The action takes place on the ground that the incident radiation is to operate a low-pass filtering of its spectrum: the frequency increases the signal penetrates less into the ground.

On the other hand, however, is that the resolution improves with increasing frequency. The choice to be made for the impulse excitation is done from time to time according to the specifications of the case, trying to combine as much as possible these two contrasting aspects.

In this thesis who the scope was to use the GPR techniques for Landmines detection and road monitoring, is an experimental thesis.

In chapter 1 after describing briefly the scattering of electromagnetic waves by buried object, and the finite difference time domain who is the numerical method to resolve the Maxwell equation, we told about the Ground penetrating radar who is the instrumentation used in all experiment in this thesis. The first section in this chapter was the scattering of the electromagnetic waves by buried object. The second section analyzes FD-TD method providing formulas to be directly implemented in the simulator program. How computational domain is built, how calculations are carried out and which are the conditions that make simulation results reliable are discussed, too. The third section analyzes the GPR theory and his main application in landmine detection and road monitoring with the theory of how it can be possible to obtain and resolve some parameters of the electromagnetic signal like dielectric constant and moisture content in a ground.

In the second chapter, it can be seen that after a simulation in two dimensions, an experiment measurement was made with a GPR and compared with the simulations in the three dimensions with FDTD.

In chapter three, who the experiment was done in a laboratory, we study an evaluation of clay content in substrate and road foundation with GPR. In this chapter we try to demonstrate experimentally the method of calculation of the dielectric constant in situation of the presence of moisture in road pavement.

The chapter four was dedicated to an really experiment in an existing road where we evaluate the moisture with GPR for the stability of the road structure. The results are very interesting and can be a data base for others road structure for future study in this domain.

Chapter 1: Ground Penetrating Radar and the Electromagnetic Scattering

1.1. Scattering of the electromagnetic waves by buried objects

1.1.1. Introduction

The electromagnetic scattering problem from buried objects is a subject with important applications to the remote sensing of the earth internal structure, to the detection of explosive mines, of pipes, conduits and tunnels, to the communication through the earth, or to biomedical imaging. For this reason, it has been widely discussed by many authors in the past, both from a theoretical and a numerical point of view.

The study of this problem, involve the knowledge of many techniques. It is particularly important to have the availability of affordable analytical and numerical models that can simulate also complicated environments. The algorithms for solving the inverse problem give, in fact, results with some approximations: the possibility of using an accurate method for the solution of direct scattering is important to help the understanding of the buried scenarios.

Among other possible methods, I decide to study and present here the so-called Cylindrical Wave Approach(CWA), for the possibility of working with analytical formulas and physics understanding at the same time. This method revealed to be accurate and flexible in application to various practical scenarios.

For example, plane-wave scattering by a perfectly-conducting or dielectric circular cylinder, in a homogeneous and isotropic medium, is a classical problem and has been studied by many authors [1]. Such problem takes a more complex form in the presence of a planar discontinuity for the electromagnetic constants, and several resolving techniques have been developed for the scattering by objects above a dielectric half-space or buried in it.

A more general characterization of scattering by buried objects can be dealt with by considering a multilayered medium. Such a problem turns out to be a really hard task, since multiple reflections occurring between the scatterers and the interfaces must be taken into account. Different methods are reported in the literature, for a general multilayered medium and for the particular case of objects embedded in a slab between two half-spaces.

In this section, the study of the electromagnetic scattering problem with a rigorous solution to the two-dimensional scattering problem of a plane wave by a set of circular cylinders, with infinite length and parallel axes, buried in a half-space, is presented. The Cylindrical Wave Approach (CWA) [2] employed in [3] and [4], to solve scattering by objects buried in a semi-infinite medium, is here applied to a layered geometry[5].

1.1.2. Geometry of the problem

The involved media are assumed linear, isotropic, homogeneous, dielectric, lossless, and separated by planar interfaces. The scatterers have parallel axes and they are parallel to the planar interfaces of separation between the media. The whole structure infinitely extends along the direction of the cylinders axes, and the propagation vector

of the incident wave lies in the plane orthogonal to the interfaces and the cylinders axes. Thus, the problem can be considered two dimensional.

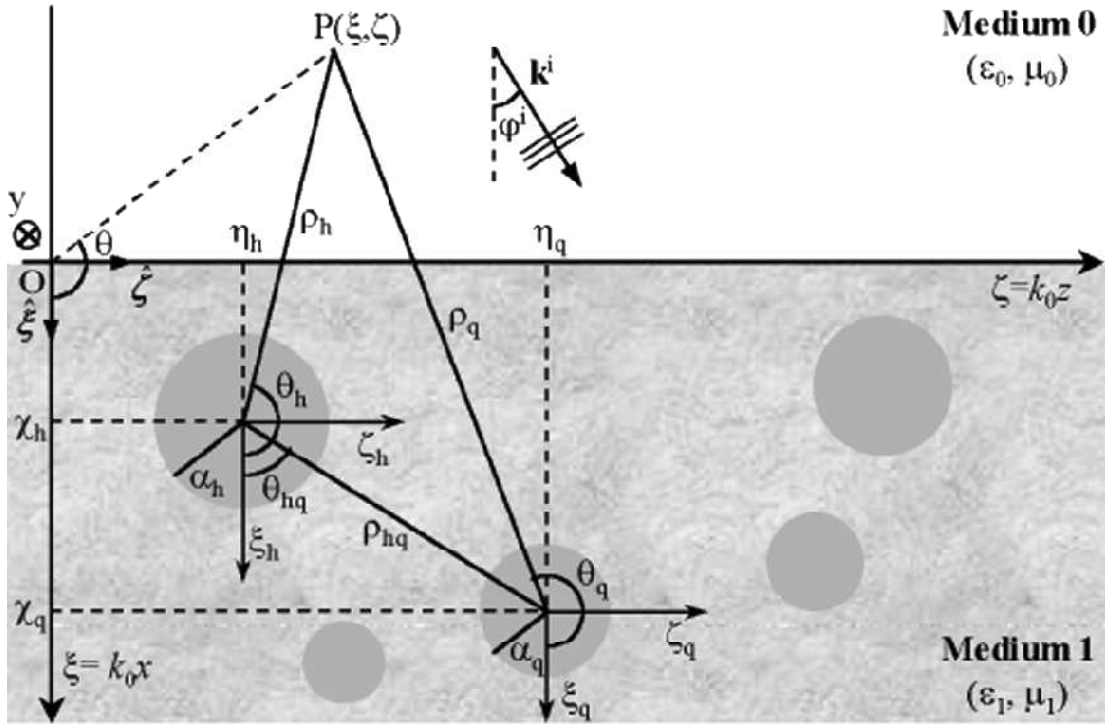


Figure 1.1. Geometry of the scattering problem

Two states of linear polarization for the incident field are dealt with, since any other state of polarization can be expressed by the superimposition of:

- E or TM polarization - The electric field is parallel to the cylinders axes. The magnetic field and the propagation vector lie in the plane orthogonal to the cylinders axes. For this reason, the E polarization is also called transverse magnetic (TM), being the magnetic field transverse to the axes of the cylindrical scatterers.
- H or TE polarization - The magnetic field is parallel to the cylinders axes. With the electric field lying in the orthogonal plane, the H polarization is also called transverse-electric (TE).

Each component of the electromagnetic field can be obtained by Maxwell equations, once known the field component parallel to the cylinders axes, which coincides with the electric and magnetic field for E and H polarization, respectively. In the whole analysis, this field component is represented by a scalar function V , which in each medium of the structure takes into account all the interactions. A time dependence $e^{-i\omega t}$, being ω the angular frequency, is assumed for the fields, and will be omitted.

1.1.3.Theoretical Analysis

The geometry of the scattering problem is shown in figure 1.2: N circular cylinders (conductors or dielectric) with possibly different radii are buried in a linear, isotropic, homogeneous, dielectric, lossless half-space (medium 1, with permittivity $\varepsilon_1 = \varepsilon_0 n_1^2$). A monochromatic plane wave, with wave vector k lying in the xz plane, impinges at an angle φ from medium 0 (a vacuum) on the planar interface with medium 1.

A main reference frame (MRF) $(0, \xi, \zeta)$, with normalized coordinates $\xi = k_0 x$ and $\zeta = k_0 z$, $k_0 = 2\pi/\lambda_0$ being the vacuum wave number is introduced. Moreover, a reference frame RF_q is centered on the q^{th} cylinder axis ($q = 1, 2, \dots, N$): both rectangular (ξ_q, ζ_q) and polar (ρ_q, θ_q) coordinates are considered, with $\xi_q = k_0 x_q = \xi - \chi_q$, $\zeta_q = k_0 z_q = \zeta - \eta_q$, $\rho_q = k_0 r_q$. The q^{th} cylinder, with dimensionless radius $\alpha_q = k_0 a_q$, has axis located in (χ_q, η_q) in MRF.

The presence of the planar interface is taken into account by means of its complex plane-wave reflection and transmission coefficients, $\Gamma_{ij}^{TE, TM}(n_{\parallel})$ and $T_{ij}^{TE, TM}(n_{\parallel})$, respectively: the unit vector $\mathbf{n}^i = n_{\perp}^i \boldsymbol{\xi} + n_{\parallel}^i \boldsymbol{\zeta}$ is parallel to the wave vector of the generic plane wave impinging from medium i on the interface with

medium $j(i, j = 0, 1)$. Here and in the following, the symbols \perp and \parallel are used to indicate the orthogonal and parallel (to the interface) components, respectively, of a generic vector. The time dependence of the field is assumed to be $e^{-i\omega t}$, where ω is the angular frequency, and will be omitted throughout this section.

The solution to the scattering problem is carried out in terms of $V(\xi, \zeta)$, which represents the y -component of the electric/magnetic field: $V = E_y(\xi, \zeta)$ for $\text{TM}^{(y)}$ polarization and $V = H_y(\xi, \zeta)$ for $\text{TE}^{(y)}$ polarization. Once $V(\xi, \zeta)$ is known, it is possible to derive all the other components of the electromagnetic field by using Maxwell's equations.

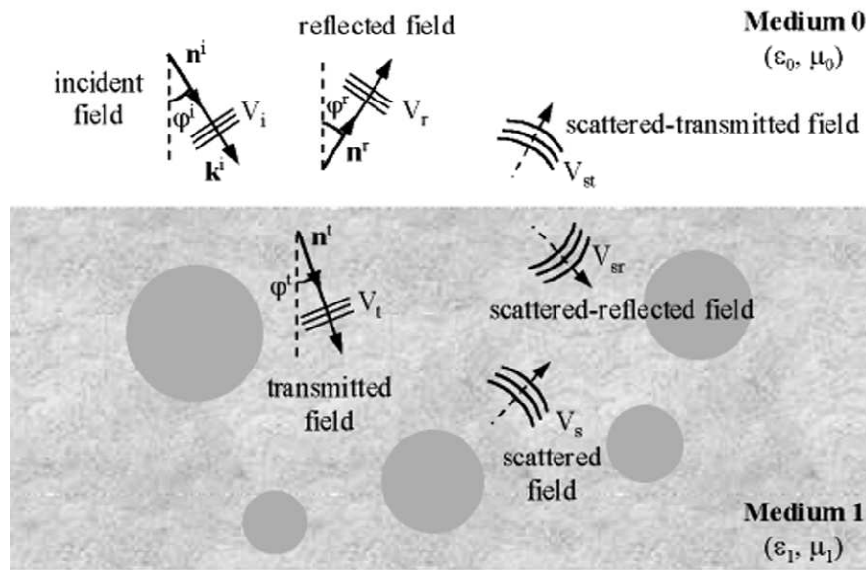


Figure 1.2. Decomposition of the total field.

In order to obtain a rigorous solution for $V(\xi, \zeta)$, the total field is expressed as the superposition of the following six terms, produced by the interaction between incident field, interface and cylinders (figure 1.2):

- $V_i(\xi, \zeta)$: incident plane-wave field;

- $V_r(\xi, \zeta)$: reflected field, due to the reflection in medium 0 of V_i by the interface;
- $V_t(\xi, \zeta)$: transmitted field, due to the transmission in medium 1 of V_i by the interface;
- $V_s(\xi, \zeta)$: field scattered by the cylinders in medium 1;
- $V_{sr}(\xi, \zeta)$: scattered-reflected field, due to the reflection in medium 1 of V_s by the interface;
- $V_{st}(\xi, \zeta)$: scattered-transmitted field, due to the transmission in medium 0 of V_s by the interface. The explicit expressions of V_i , V_r , and V_t can be seen in [6].

The scattered field V_s can be written as the sum of the fields scattered in medium 1 by each cylinder, expressed by a superposition of cylindrical functions with unknown coefficients C_{hl} .

$$V_s(\xi, \zeta) = \sum_{h=1}^N \sum_{l=-\infty}^{+\infty} V_0 c_{hl} i^l e^{-il\varphi_t} CW_l(n_1 \xi_h, n_1 \zeta_h) \quad (1.1)$$

In (1.1), V_0 is the incident plane-wave amplitude, φ_t is the angle of the transmitted plane wave, according to Snell's law, $CW_l(n_1 \xi_h, n_1 \zeta_h) = H_l^{(1)}(n_1 \rho_h) e^{il\theta_h}$, where $H_l^{(1)}$ is the first kind Hankel function of integer order l ; the term $i^l e^{-il\varphi_t}$ has been introduced for symmetry with the expression of V_t . Note that (1.1) gives the field associated to the point having coordinates (ξ, ζ) in MRF as a function of the coordinates (ξ_q, ζ_q) in RF_q, being $\xi = \chi_q + \xi_q$ and $\zeta = \eta_q + \zeta_q$.

Making use of the addition theorem of Hankel functions [7], we can express in the RF_q a cylindrical wave emitted by the h^{th} cylinder, as

$$H_l^{(1)}(n_1 \rho_h) e^{il\theta_h} = e^{il\theta_{hq}} \times \sum_{m=-\infty}^{+\infty} (-1)^m H_{l+m}^{(1)}(n_1 \rho_{hq}) e^{im\theta_{hq}} J_m(n_1 \rho_q) e^{-im\theta_q} \quad (1.2)$$

After some manipulations, the following expression for the scattered field in RF_q is obtained:

$$V_s(\xi, \zeta) = V_0 \sum_{m=-\infty}^{+\infty} J_m(n_1 \rho_q) e^{im\theta_q} \sum_{h=1}^N \sum_{l=-\infty}^{+\infty} c_{hl} i^l e^{-il\varphi_t} \times \left[CW_{l-m}(n_1 \xi_{hq}, n_1 \zeta_{hq})(1 - \delta_{hq}) + \frac{H_m^{(1)}(n_1 \rho_q)}{J_m(n_1 \rho_q)} \delta_{hq} \delta_{ml} \right] \quad (1.3)$$

where δ_{hq} and δ_{ml} is the Kronecker symbols. Note that (1.3) gives the field associated to the point having coordinates (ξ_q, ζ_q) in MRF as a function of the coordinates (ρ_q, θ_q) in RF_q , being $\xi = \chi_q + \rho_q \cos \theta_q$ and $\zeta = \eta_q + \rho_q \sin \theta_q$.

To express the fields V_{sr} and V_{st} , the presence of the planar surface is taken into account by considering the reflection and transmission of each elementary plane wave constituting the Fourier spectrum F_l of the cylindrical function CW_l . Such Fourier spectrum is defined as follows:

$$F_\ell(u, n_\parallel) = \int_{-\infty}^{+\infty} CW_\ell(u, v) e^{-in_\parallel v} dv \quad (1.4)$$

with explicit expression

$$F_\ell(u, n_\parallel) = \frac{2}{\sqrt{1-n_\parallel^2}} e^{i|u|\sqrt{1-n_\parallel^2}} \begin{cases} e^{-i\ell \arccos n_\parallel} (u \geq 0) \\ e^{i\ell \arccos n_\parallel} (u \leq 0) \end{cases} \quad (1.5)$$

The scattered-reflected field V_{sr} is given by the sum of the fields scattered by each buried cylinder and reflected by the interface. After some algebra calculus we have:

$$V_{sr} = \sum_{h=1}^N \sum_{\ell=-\infty}^{+\infty} V_0 c_{h\ell} i^\ell e^{-i\ell\varphi_t} RW_\ell[n_1(-2\chi_h - \xi_h), n_1\zeta_h] \quad (1.6)$$

where $RW_\ell(u, v)$ are the reflected cylindrical functions [15], defined by

$$RW_\ell(u, v) = \frac{1}{2\pi} \int_{-\infty}^{+\infty} \Gamma_{10}(n_\parallel) F_\ell(u, n_\parallel) e^{ivn_\parallel} dn_\parallel \quad (1.7)$$

Starting from (1.6), making use of (1.7), (1.5) and of the expansion of a plane wave in terms of first-kind Bessel functions, after some manipulations we obtain V_{sr} as a function of the coordinates (ρ_q, θ_q) in RF_q

$$V_{sr}(\xi, \zeta) = V_0 \sum_{m=-\infty}^{+\infty} J_m(n_1 \rho_q) e^{im\theta_q} \sum_{h=1}^N \sum_{\ell=-\infty}^{+\infty} c_{h\ell} i^\ell e^{-i\ell\varphi_t} \times RW_{m+\ell}[-n_1(\chi_h + \chi_q), n_1(\eta_q - \eta_h)] \quad (1.8)$$

The scattered-transmitted field is given by the sum of the fields scattered by each buried cylinder and transmitted to medium 0

$$V_{st}(\xi, \zeta) = \sum_{h=1}^N \sum_{\ell=-\infty}^{+\infty} V_0 c_{h\ell} i^\ell e^{-i\ell\varphi_t} TW_\ell(\xi_h, \zeta_h, \chi_h) \quad (1.9)$$

The TW_ℓ are the transmitted cylindrical functions [8], defined by

$$TW_\ell(u, v, \chi) = \frac{n_1}{2\pi} \int_{-\infty}^{+\infty} T_{10}(n_\parallel) F_\ell(-n_1 \chi, n_\parallel) \times e^{-i\sqrt{1-(n_1 n_\parallel)^2}(u+\chi)} e^{in_1 n_\parallel v} dn_\parallel \quad (1.10)$$

Once the expressions of all the fields have been given, the boundary conditions on the cylinder surfaces have to be imposed: due to the hypothesis of perfectly conducting cylinders, the tangential component of the total electric field must vanish. The following equation has to be written for TM polarization:

$$V_t + V_s + V_{sr}|_{\rho_q=k_0 a_q} = 0 \quad \text{with } q = 1, \dots, N \quad (1.11)$$

In the TE case, using Maxwell's equations we have

$$\frac{\partial}{\partial \rho_q} (V_t + V_s + V_{sr})|_{\rho_q=k_0 a_q} = 0 \quad \text{with } q = 1, \dots, N \quad (1.12)$$

By using the orthogonal property of the exponential functions, after some manipulations, it is possible to obtain a linear system for the unknown coefficients c_{hl} , for both TM and TE cases

$$\sum_{h=1}^N \sum_{\ell=-\infty}^{+\infty} A_{m\ell}^{hq(TM,TE)} c_{h\ell} = B_m^{q(TM,TE)} \quad m=0, \pm 1, \dots, \pm \infty \quad q=1, \dots, N \quad (1.13)$$

with

$$A_{m\ell}^{hq(TM,TE)} = i^{\ell-m} e^{-i\ell\varphi_t} \left\{ [(1 - \delta_{hq}) CW_{\ell-m}(n_1 \xi_{hq}, n_1 \zeta_{hq}) + RW_{\ell+m}(-n_1 \chi_q - n_1 \chi_h, n_1 \eta_q - n_1 \eta_h)] \times G_m^{(TM,TE)}(n_1 \alpha_q) + \delta_{hq} \delta_{\ell m} \right\} \quad (1.14)$$

$$B_m^{q(TM,TE)} = -T(n_{\parallel}^i) e^{in_1(n_{\perp}^t \chi_q + n_{\parallel}^t \eta_q)} e^{-im\varphi_t} G_m^{(TM,TE)}(n_1 \alpha_q) \quad (1.15)$$

where $G_m^{(TM)}(x) = J_m(x)/H_m^{(1)}(x)$ and $G_m^{(TE)}(x) = J'_m(x)/H_m^{(1)'}(x)$.

Once the system (1.13) has been solved, the total electromagnetic field is completely determined in any point of the space and for both polarizations.

Although no approximations have been introduced in the theoretical basis of this method, dealing with numerical procedures it is obviously necessary to truncate the series in (1.13) to a finite number of elements

$$\sum_{h=1}^N \sum_{\ell=-\infty}^{+\infty} A_{m\ell}^{hq(TM,TE)} c_{h\ell} = B_m^{q(TM,TE)} \quad m=0, \pm 1, \dots, \pm \infty \quad q=1, \dots, N \quad (1.16).$$

The choice of the truncation index as $M \cong 3n_1 \alpha$, where α is the maximum dimensionless radius $\alpha_q (q = 1, \dots, N)$, usually reveals an efficient truncation criterion, showing a good compromise between accuracy and computational heaviness [9].

A check of such criterion is shown further. However, in all the performed computations we required a convergence on the third significant figure: to this aim, in some cases we had to use larger values of M .

The evaluation of the generalized cylindrical reflected and transmitted wave functions $RW_l(u, v)$ and $TW_l(u, v, \chi)$ has to be numerically carried out. In fact, in all practical cases, the expressions of the reflection and transmission coefficients Γ and T do not allow an analytical evaluation of the integrals in (1.7) and (1.10). In order to develop an efficient integration algorithm, one has to take into account the infinite extension of the integration domain, since the solution cannot neglect the evanescent components of the spectrum. Moreover, the spectrum of the cylindrical-wave functions shows a highly oscillating behavior as the expansion order l increases. A suitable algorithm for the integration of the $RW_l(u, v)$ functions has been developed in [10] and [11], where adaptive techniques of Gaussian type have been employed, together with convergence acceleration procedures. Successively, the algorithm has been generalized to integrate also the $TW_l(u, v, \chi)$ functions [12].

To validate the employed approach, one of the many cases founded in literature we consider the mutual interaction of two buried cylinders placed as in figure 1.3. The study of multiple scattering by two objects has been the subject of several papers [13].

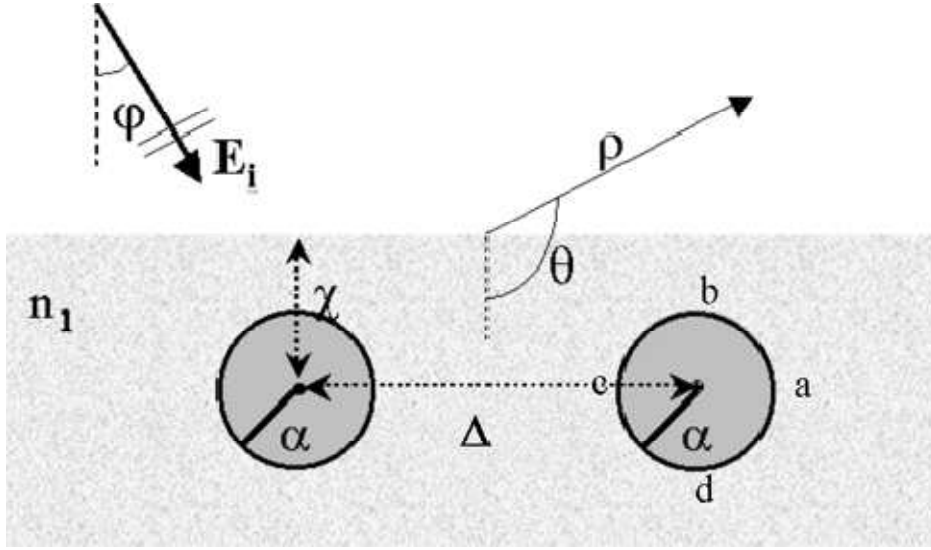
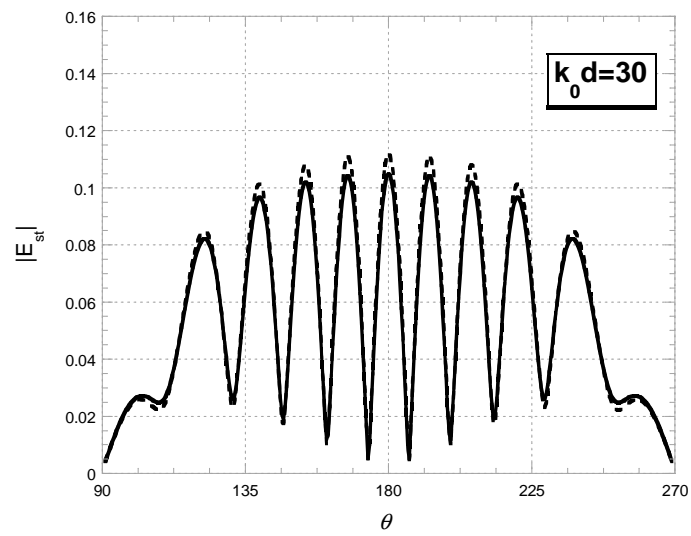
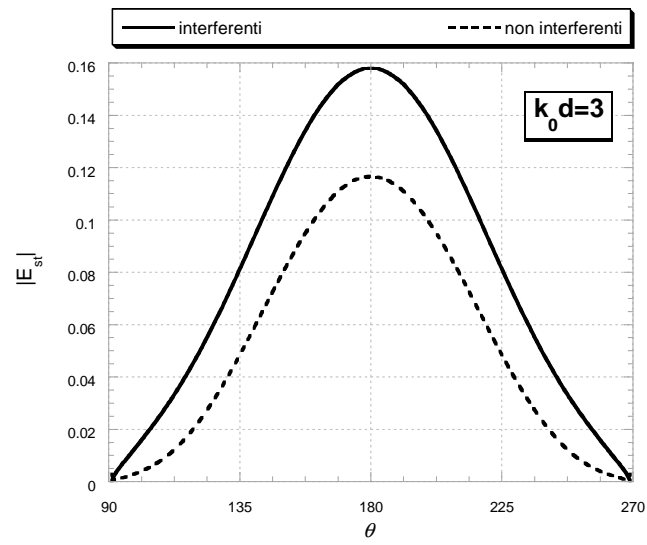


Figure 1.3. Geometrical layout for the study of two interacting buried cylinders

Many of them dealt with scatterers in a homogeneous medium but, to our knowledge, in the literature similar studies for the case of scatterers buried in a dielectric half-space are not present. When the scatterers are far enough from each other so that the mutual interaction can be neglected, the total scattered intensity should look like the one obtained by non interacting cylinders, but the resemblance should be reduced as their distance decreases. Such expected behavior is actually obtained with our simulations which are shown in figure 1.4, where $|E_{st}|$ is plotted as a function of θ , for four different values of the normalized distance $\Delta = k_0 d$, when $n_1=2$, $\alpha=1$, $\phi^i=0^\circ$, $\chi=2.6$, $\rho=50$ and for TM polarization.



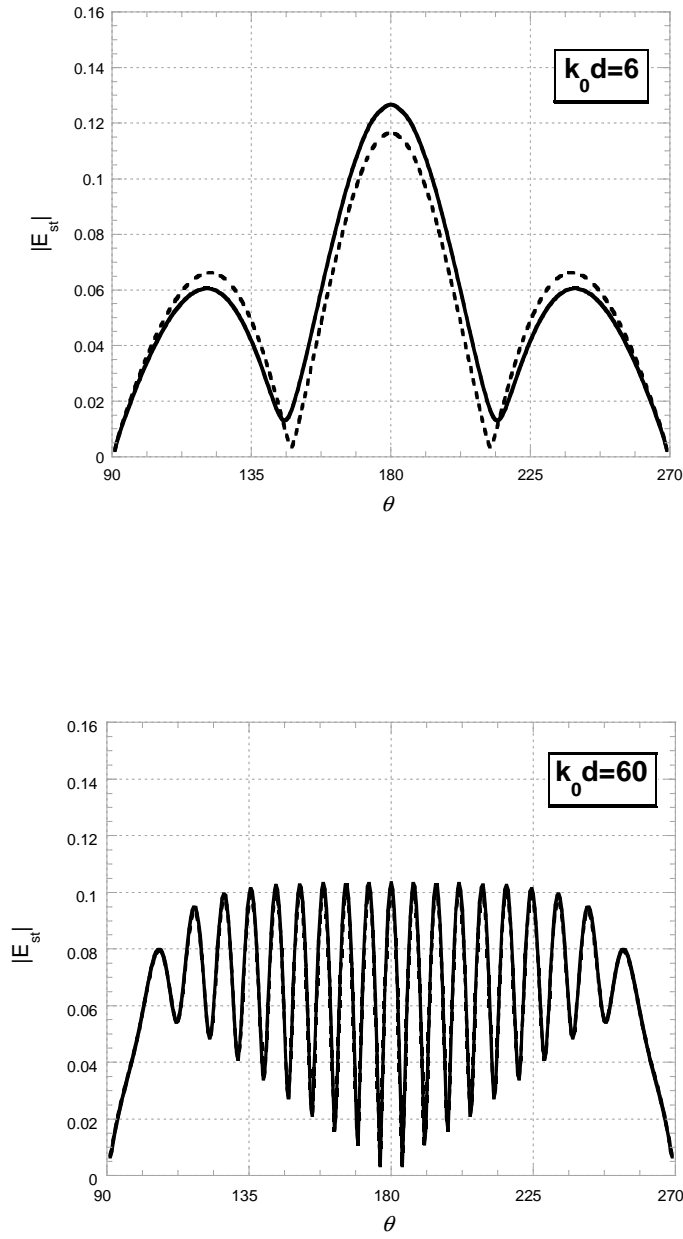


Figure 1.4. The effect of the distance Δ on the scattered-transmitted field, for the configuration of the figure 1.3.

In the same figure the corresponding pattern for non interacting cylinders is reported, too (dashed curves).

We have considered the 2-D plane-wave scattering problem by a set of perfectly conducting circular cylinders buried in a dielectric half-space. The proposed method may deal with both TM and TE polarization cases and yields results in both the near- and the far-field zones. Moreover, it may be applied for any value of the cylinder size and of the distance between the obstacles and the surface.

The presented technique could be used for the characterization of suitable scenarios in the context of Ground Penetrating Radar applications (GPR) [14], which usually employ purely numerical FDTD techniques [15]. Furthermore, our method may be employed in iterative algorithms for the solution of inverse problems, where fast, efficient and accurate forward solvers are needed, since the forward problem has to be solved repeatedly [16].

Convergence checks and a self-consistency test have been performed. Comparisons have been made with available results presented in the literature, with very good agreement. The multiple scattering between two buried cylinders has been considered in some detail.

In this section we generalize the scattering problem solved using the CWA approach. In the following it was developed a FDTD method that was used for simulation in chapter 2. This method was seen accurate and versatile for resolution of the Maxwell's equation in time domain and with an accurate FFT it was easy to have also the frequency domain.

1.2. The Finite Difference Time - Domain Method

1.2.1 Introduction

Electromagnetic field, whose behavior is described by Maxwell's equations and constitutive relations, can be obtained using three types of not exclusive approaches: analytical, numerical and experimental methods. Analytical methods let us know the exact field but, as soon as the complexity of the problem grows, the drastic approximations we need to consider reflect themselves on result's reliability. Experimental methods, on the other hand, provide us with reliable data, within the accuracy of the apparatus; however, they're time-consuming and expensive. Finally, numerical methods offer solutions whose accuracy is given by the quality of the used mathematical models, at reasonable time and cost. Among them, there are two main groups: time domain and frequency domain methods.

1.2.2 Finite difference time domain method

The finite difference time domain method (FD-TD) is a numerical method that performs all necessary calculations using a discretized version of Maxwell's equations applied to the finite discretized region where electromagnetic field is to be solved for. FD-TD relies mainly on Yee's algorithm, which describes how[17]:

- Maxwell's equations are modified;
 - space region is discretized to obtain the computational domain;
 - calculations are carried out on electromagnetic field component with respect to time.
- To completely define the method, an analysis of the following aspects should be done, too:
- numerical stability;

- numerical dispersion;
- boundary conditions.

FD-TD, like every numerical method, has strengths and weaknesses but nowadays, because of the increased capacity of current computers, the weakness of the FDTD method like memory and time consuming, and eventual post-processing are managed without any problem. It is for that FD-TD method become more powerful method and is used by many authors.

In fact, FD-TD is versatile and intuitive because the computational domain that represents the electromagnetic device to be studied is built up like an experimental apparatus. As a result, the method can be used to predict unexpected effects beforehand. It must be stressed how FD-TD algorithm relies heavily on the choice of simulation parameters, such as resolutions and their respective ratio, even for two very similar devices. Those parameters are indeed important to gain a simulated behavior that truly reflects the real one and to make FD-TD a valid tool for describing the electromagnetic field variations the same way as it would be done in real life experiments.

FD-TD is wide-frequency ranged because the algorithm it uses behaves like a linear system within the limits given by the computational domain resolution and the contour conditions quality, in particular the radiation boundary condition (RBC) mathematical model. In addition, since Maxwell's equations are applied in each point of the electromagnetic system to be solved for, \mathbf{E} and \mathbf{H} are known everywhere. Most important, the device can assume any shape and build up using any material (as long as the respective expression for Maxwell's equations are adopted in the mathematical description of the electromagnetic field). The only limit is the resolution and shape of the lattice adopted: if there are curved surfaces in a computational domain that uses cubic elementary cells, an approximation is unavoidable.

Since an open system has an infinite extension and calculation introduces limits for domain dimension and calculation time, it's necessary to simulate the radiation condition at infinite distance, exactly as it happens in an anechoic chamber. Unavoidable reflections are introduced in the system: conceptually, if no dissipative materials are adopted and power is continuously put in the device, the energy contained in the computational domain will diverge. Fortunately, there are RBCs models that make this process very slow compared to the time needed to reach steady condition with very good accuracy, too.

FD-TD method, was accused to be memory and time consuming. In fact, the entire computational domain must be discretized and memorized. Since elementary cells must be small compared to the smallest wavelength that needs to be considered (higher resolutions, i.e.: number of cells for each wavelength, imply smaller numerical errors) and smallest element inserted in the device (i.e.: constitutive parameters should change slowly over a small number of cells). Moreover, a bigger computation domain means longer simulation time: the number of calculations for each time interval and the time intervals needed to reach steady condition grows as the number of cells increases. Thus, for instance, if the electromagnetic field at far distance (i.e.: Fraunhofer region) is to be calculated, a certain amount of post-processing is needed otherwise computational domain dimension would increase exceeding memory resources and plausible calculation time. And for this issue, computers are powerful and reduced the calculation time.

1.2.3 Yee's algorithm

The computational domain is a lattice made up by unit cells, whose surface contains all field components.

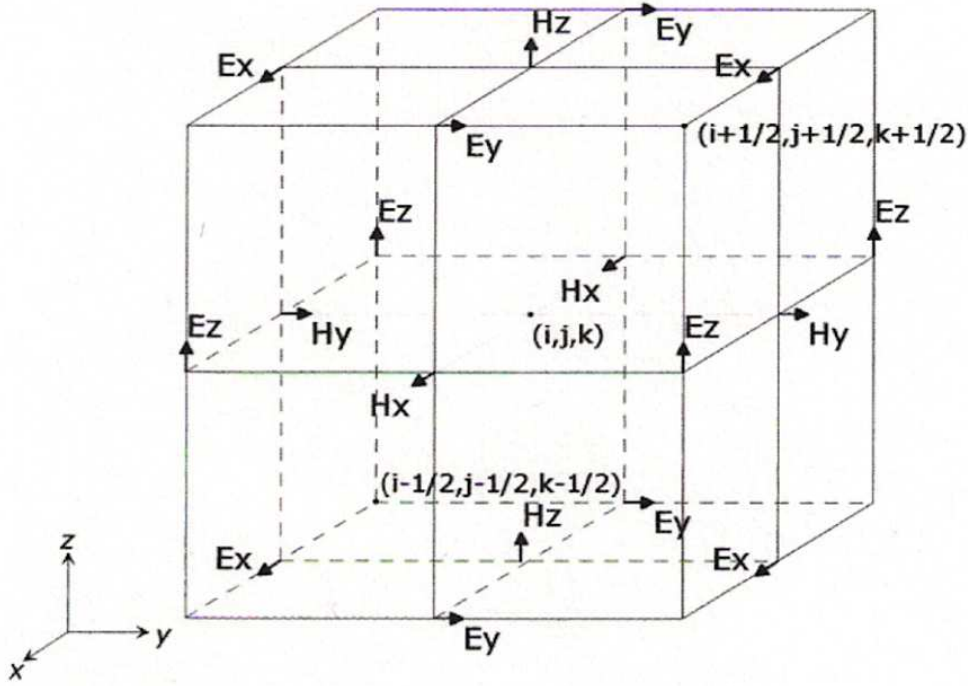


Figure 1.5. Yee's unit cell. On the faces of the imaginary cube, it can be observed how the field components are arranged to obtain circuits.

The direction of all vectors is chosen identical to reference axes. If Δx , Δy and Δz are the lengths of the elementary cell, each cell in the computational domain is uniquely identified by three integers i , j and k :

$$P = (i\Delta x, j\Delta y, k\Delta z) \quad (1.17)$$

Since \mathbf{E} and \mathbf{H} are also functions of time, supposing Δt to be the interval used to discretize time, one can write:

$$\mathbf{E}(P, t) = \mathbf{E}(i\Delta x, j\Delta y, k\Delta z, n\Delta t) \quad (1.18)$$

$$\mathbf{H}(P, t) = \mathbf{H}(i\Delta x, j\Delta y, k\Delta z, n\Delta t) \quad (1.19)$$

with n integer. In a more compact form:

$$\mathbf{E}(P,t) = \mathbf{E}(i, j, k, n) \quad (1.20)$$

$$\mathbf{H}(P,t) = \mathbf{H}(i, j, k, n) \quad (1.21)$$

Yee's algorithm uses a "leap-frog" approach to update all field components in each time interval, Δt . For instance, if the electromagnetic field is completely known until time t , to obtain how it evolves until time $t + \Delta t$, the magnetic field at $t + \Delta t/2$ is calculated starting from electric field at time t , and the electric field at time $t + \Delta t$ is calculated using the magnetic field previously obtained. Thus:

$$\mathbf{H}(i, j, k, n + 1/2) = \mathbf{F}_H\{\mathbf{E}(o, p, q, n)\} \quad (1.22)$$

$$\mathbf{E}(i, j, k, n + 1) = \mathbf{F}_E\{\mathbf{H}(o, p, q, n + 1/2)\} \quad (1.23)$$

with o, p and q , all possible indices in the computational domain and $\mathbf{F}_E, \mathbf{F}_H$ the two functions that let calculate one field from the other, in other words Maxwell's equations combined with constitutive equations, boundary conditions and impressed fields. Using this approach, the whole electromagnetic field is updated as each Δt elapses and an "actual state – future state" approach is not required, thus saving precious memory resources. However, the leap-frog approach doesn't let us know both electric and magnetic field at the same instant of time; in fact, if \mathbf{H} is known at generic time instant $n + 1/2$, \mathbf{E} is known at time instant n or $n + 1$.

Maxwell's equations need to be modified to work on the defined computational domain; specifically, they are to be discretized with respect to space and time. The second order accurate algorithm central-difference formula is adopted, in this thesis, to represent both time and space derivatives. As a result, if $f = f(h)$, its derivative can be approximated with:

$$f'(h) \cong \frac{f(h + \frac{\Delta h}{2}) - f(h - \frac{\Delta h}{2})}{\Delta h} \quad (1.24)$$

Assuming an isotropic material, Maxwell's equations can be written as:

$$\frac{\partial}{\partial t} \mathbf{H} = -\frac{1}{\mu} \nabla \times \mathbf{E} - \frac{\rho'}{\mu} \mathbf{H} \quad (1.25)$$

$$\frac{\partial}{\partial t} E = \frac{1}{\varepsilon} \nabla \times H - \frac{\sigma}{\varepsilon} E \quad (1.26)$$

where μ is the magnetic permeability, ρ' is the magnetic conductivity, ε is the electric permittivity or dielectric constant and σ is the electric conductivity.

Considering \mathbf{H}_x and applying the central-difference formula for all derivatives in (1.25):

$$\begin{aligned} & \frac{H_x(i,j,k,n+1/2)+H_x(i,j,k,n-1/2)}{\Delta t} = \\ & \frac{1}{\mu(i,j,k)} \left(\frac{\varepsilon_y(i,j,k+1/2,n)+\varepsilon_y(i,j,k-1/2)}{\Delta z} - \frac{\varepsilon_z(i,j+1/2,k,n)+\varepsilon_z(i,j-1/2,k,n)}{\Delta y} - \right. \\ & \left. \rho'(i,j,k).H_x(i,j,k,n) \right) \end{aligned} \quad (1.27)$$

To calculate $\mathbf{H}_x(i, j, k, n)$, which the algorithm, because of the leap-frog approach, doesn't memorize, the "semi-implicit" approximation is used:

$$H_x(i,j,k,n) = \frac{H_x(i,j,k,n+1/2)+H_x(i,j,k,n-1/2)}{2} \quad (1.28)$$

Such process has been demonstrated to be numerically stable and accurate for each value of $\rho'(i, j, k) \in (0, +\infty)$, in (1.27). Substituting and rearranging (1.27):

$$\begin{aligned} H_x \left(i, j, k, n + 1/2 \right) &= \frac{\left(1 - \frac{\rho'(i,j,k).\Delta t}{2.\mu(i,j,k)} \right)}{\left(1 + \frac{\rho'(i,j,k).\Delta t}{2.\mu(i,j,k)} \right)} H_x \left(i, j, k, n - 1/2 \right) + \frac{\frac{\Delta t}{\mu(i,j,k)}}{\left(1 + \frac{\rho'(i,j,k).\Delta t}{2.\mu(i,j,k)} \right)} \cdot \\ & \left(\frac{E_y(i,j,k+1/2,n)+E_y(i,j,k-1/2,n)}{\Delta z} - \frac{E_z(i,j+1/2,k,n)+E_z(i,j-1/2,k,n)}{\Delta y} \right) \end{aligned} \quad (1.29)$$

The following coefficients can be defined:

$$C_a(i,j,k) = \frac{\left(1 - \frac{\sigma(i,j,k).\Delta t}{2.\mu(i,j,k)} \right)}{\left(1 + \frac{\sigma(i,j,k).\Delta t}{2.\mu(i,j,k)} \right)} ; C_b = \frac{\frac{\Delta t}{\varepsilon(i,j,k)}}{\left(1 + \frac{\sigma(i,j,k).\Delta t}{2.\mu(i,j,k)} \right)}$$

$$D_a(i, j, k) = \frac{\left(1 - \frac{\rho'(i, j, k) \Delta t}{2 \mu(i, j, k)}\right)}{\left(1 + \frac{\rho'(i, j, k) \Delta t}{2 \mu(i, j, k)}\right)} \quad ; \quad D_b(i, j, k) = \frac{\frac{\Delta t}{\mu(i, j, k)}}{\left(1 + \frac{\rho'(i, j, k) \Delta t}{2 \mu(i, j, k)}\right)} \quad (1.30)$$

Applying the same procedure to all **E** and **H** components and adopting the coefficients in (1.30):

$$H_x\left(i, j, k, n + \frac{1}{2}\right) = D_a(i, j, k)H_x(i, j, k, n - \frac{1}{2}) + D_b(i, j, k) \cdot \left(\frac{E_y(i, j, k + \frac{1}{2}, n) - E_y(i, j, k - \frac{1}{2}, n)}{\Delta z} - \frac{E_z(i, j + \frac{1}{2}, k, n) - E_z(i, j - \frac{1}{2}, k, n)}{\Delta y}\right) \quad (1.31)$$

$$H_y\left(i, j, k, n + \frac{1}{2}\right) = D_a(i, j, k)H_y(i, j, k, n - \frac{1}{2}) + D_b(i, j, k) \cdot \left(\frac{E_z(i + \frac{1}{2}, j, k, n) - E_z(i - \frac{1}{2}, j, k, n)}{\Delta x} - \frac{E_x(i, j, k + \frac{1}{2}, n) - E_x(i, j, k - \frac{1}{2}, n)}{\Delta z}\right) \quad (1.32)$$

$$H_z\left(i, j, k, n + \frac{1}{2}\right) = D_a(i, j, k)H_z(i, j, k, n - \frac{1}{2}) + D_b(i, j, k) \cdot \left(\frac{E_x(i, j + \frac{1}{2}, k, n) - E_x(i, j - \frac{1}{2}, k, n)}{\Delta y} - \frac{E_y(i + \frac{1}{2}, j, k, n) - E_y(i - \frac{1}{2}, j, k, n)}{\Delta x}\right) \quad (1.33)$$

$$E_x\left(i, j, k, n + \frac{1}{2}\right) = C_a(i, j, k)E_x(i, j, k, n - \frac{1}{2}) + C_b(i, j, k) \cdot \left(\frac{H_z(i, j + \frac{1}{2}, k, n) - H_z(i, j - \frac{1}{2}, k, n)}{\Delta y} - \frac{H_y(i, j, k + \frac{1}{2}, n) - H_y(i, j, k - \frac{1}{2}, n)}{\Delta z}\right) \quad (1.34)$$

$$E_y\left(i, j, k, n + \frac{1}{2}\right) = C_a(i, j, k)E_y(i, j, k, n - \frac{1}{2}) + C_b(i, j, k) \cdot \left(\frac{H_x(i, j, k + \frac{1}{2}, n) - H_x(i, j, k - \frac{1}{2}, n)}{\Delta z} - \frac{H_z(i + \frac{1}{2}, j, k, n) - H_z(i - \frac{1}{2}, j, k, n)}{\Delta x}\right) \quad (1.35)$$

$$E_z\left(i, j, k, n + \frac{1}{2}\right) = C_a(i, j, k)E_z(i, j, k, n - \frac{1}{2}) + C_b(i, j, k) \cdot \left(\frac{H_y(i+1/2, j, k, n) - H_y(i-1/2, j, k, n)}{\Delta x} - \frac{H_x(i, j+1/2, k, n) - H_x(i, j-1/2, k, n)}{\Delta y}\right) \quad (1.36)$$

Having described how the discretized time-space domain is built up and the calculations needed to be performed on the electromagnetic field, stability, accuracy and boundary conditions are to be discussed to make a simulation possible.

1.2.4 Courant's condition

To avoid numerical instability, the smallest time increment, δt , must satisfy Courant's condition, which states:

$$\delta t \leq \delta t_{min} = \frac{1}{v_{max} \sqrt{\left(\frac{1}{\Delta x}\right)^2 + \left(\frac{1}{\Delta y}\right)^2 + \left(\frac{1}{\Delta z}\right)^2}} \quad (1.37)$$

being v_{max} the maximum expected wave velocity in the simulation domain and Δx , Δy and Δz the dimensions of Yee's elementary cell.

The condition can be obtained from Maxwell's equations as described in the appendices; it's worth noticing that Courant's stability criterion is strictly related to the derivative model adopted, central-difference formula[18]. Choosing δt very near to δt_{min} , as defined in (1.37), allows reaching steady condition in a smaller number of time increments and, as a consequence, a smaller numerical error; in fact, the more time increments are performed, the more calculations are done and the longer the simulation lasts. Since every machine floating point calculation involves rounding-off and is based on all past calculations, error is a monotonically increasing quantity. In addition, if any RBC is adopted, its model introduces more spurious reflections as time elapses. On the other hand, to have a bigger δt_{min} , is necessary increasing Yee's unit cell dimension and a coarser discretization of space region. Since discretization

directly affects the model accuracy, overall simulation accuracy is consequence of a trade-off among all simulation parameters, fixed after all mentioned considerations. Parameters choice, as a result, is a matter of experience, exactly as it happens when developing an experimental apparatus.

1.2.5 Numerical dispersion

Numerical algorithms that use Maxwell's equations (in time domain) cause a "dispersion"; in other words, a phase velocity variation occurs when a wave propagates in the computational lattice exactly as it happens in dispersive media. Generally, phase velocity of modes obtained numerically, differs from light speed in open space, c , because of wavelength variations, propagation direction, discretization type and eventual anisotropies.

Normally, the phase velocity deviation, alias numerical dispersion, introduced by FD-TD algorithm is caused by the propagation direction of the generic wave front that it's not necessarily parallel to Yee's unit cells sides. In other words, if we suppose a spherical wave originating from a point in the lattice, electromagnetic field propagates at different phase velocities for different directions.

In [17] the numerical dispersion evaluation of an FD-TD implementation that uses central-difference formula and semi-implicit approximation is shown. Numerical dispersion is given as a function of wave propagation angle measured with respect to the normal of Yee's unit cell generic face, θ , and R , the adopted resolution. It can be noted that wavelengths in dielectric substances are generally smaller than open space.

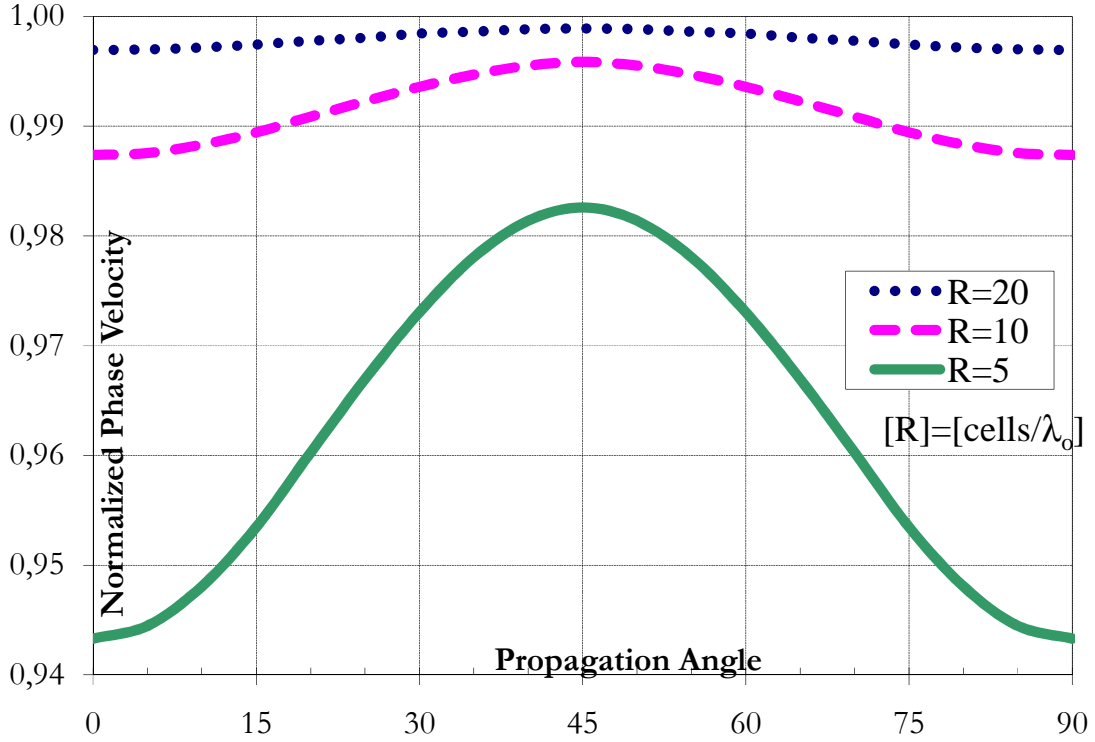


Figure 1.6 Numerical dispersion expressed as Normalized Phase Velocity, that is the ratio between the simulated phase velocity and the real one (speed of light, for open space).

If numerical dispersion is not properly accounted for, inaccurate results can be generated because of latencies, phase errors, imprecise interference (e.g.: multiple paths), anisotropy and pseudo-diffraction. So, before running an FD-TD simulation, after the maximum phase error to be tolerated is fixed, a good evaluation of discretization resolution should be obtained. Obviously, the special resolution must be, in any case, adequate to represent the highest spatial frequency to be accounted for (i.e.: sampling theorem). The phase error can be thought in terms of the path difference occurring between the real and simulated wave:

$$\Delta\varphi = 2\pi \frac{\Delta l}{\lambda_0} \quad (1.38)$$

being λ_0 the radiation wavelength.

To get a rough expression that relates phase error to resolution, the following relationship for the path difference can be considered; supposing a wave traveling in open space:

$$\frac{\Delta l}{\Delta t} \approx c - v \quad (1.39)$$

The formula (1.39) expresses the difference between the distance that the actual wave covers at the speed of light, c , and the one traveled by simulated wave at speed, v , in the smallest time increment Δt .

Substituting for Δl in (1.39):

$$\Delta\varphi = \frac{2\pi}{\lambda_0} \Delta t \cdot (c - v) \quad (1.40)$$

Letting η be the normalized phase velocity, as defined in figure 1.6, v / c :

$$\Delta\varphi = \frac{2\pi}{\lambda_0} \Delta t \cdot c \cdot (1 - \eta) \quad (1.41)$$

Considering one dimension:

$$\Delta t = \frac{\Delta x}{v} N_x = \frac{\Delta x}{\eta c} N_x \quad (1.42)$$

where N_x is the proportionality constant that represents the distance covered by wave front scaled by the unit cell side dimension, Δx .

$$\Delta\varphi = \frac{2\pi}{\lambda_0} \cdot \frac{\Delta x}{\eta c} N_x \cdot c \cdot (1 - \eta) = 2\pi \frac{\Delta x}{\lambda_0} N_x \left(\frac{1-\eta}{\eta} \right) \quad (1.43)$$

If $R = \Delta x / \lambda_0$, representing the adopted resolution, is the number of cells needed to cover a wavelength distance in x direction.

$$\Delta\varphi = 2\pi \frac{N_x}{R} \left(\frac{1-\eta}{\eta} \right) \quad (1.44)$$

Supposing that $\eta = \eta(\theta, R)$, as done to represent figure 1.6:

$$\Delta\varphi = 2\pi \frac{N_x}{R} \left(\frac{1-\eta(\theta, R)}{\eta(\theta, R)} \right) \quad (1.45)$$

Phase error is linearly increasing with distance, and inversely proportional to discretization resolution. To consider the worst case it's necessary picking out the

minimum value of normalized phase velocity, that occurs at $\theta = 0$ (or $\theta = \pi / 2$).

Therefore:

$$\Delta\varphi_{max} = 2\pi \frac{N_x}{R} \left(\frac{1-\eta(0,R)}{\eta(0,R)} \right) = 2\pi \frac{N_x}{R} \left(\frac{1-\eta_{min}(0,R)}{\eta_{min}(0,R)} \right) \quad (1.46)$$

In FD-TD method application, it's often necessary an expression of the maximum length of computational domain related to the allowed maximum phase error. Rearranging (1.46):

$$N_{x_{max}} = \frac{\Delta\varphi_{max}}{2\pi} \left(\frac{1-\eta_{min}(R)}{\eta_{min}(R)} \right) R \quad (1.47)$$

If numerical dispersion is not accounted for, simulations can give inadmissible or non physical results, caused by multiple spurious reflections and refractions.

Because expressions (1.46) and (1.47) have been found for one direction, care must be taken when not-cubic unit cells are used for discretization. As a rule of thumb, taking account of numerical dispersion considering the lowest resolution adopted is a good assessment.

1.2.6 Bérenger's PML

If at least one dimension of an electromagnetic system is not finite (e.g.: a device which radiates in open space, such as an antenna), since resources are limited, the computational domain must be truncated and, as a consequence, a contour condition that lets waves trespassing truncation radiate as it does in open space is necessary. There are lots of RBC models and many of them use the concept of *one-way* operator [19], a method that, in theory, allows propagation in one direction only. Other models simulate open space radiation through a surface employing layers made up of particular materials, even not real. This approach was used by Bérenger to realize his perfectly matching layer (PML) in 2D case [20], lately extended to 3D by Katz [21].

The system to be simulated is surrounded by PML, a non physical dissipative material characterized by high losses, which is then wrapped in a PEC surface. Usage of correctly implemented PMLs, can help obtaining simulations with reflection ratios smaller than -50dB , comparable to most anechoic chambers. In practical situations, there is more than a PML, with different material constants, which follow an arbitrary profile pattern: usually, the more layers are used, the overall back reflection is lowered.

1.2.7 The FDTD simulation

The calculation of an electromagnetic problem by the FDTD method is divided into several phases:

- 1) The system under study is analyzed taking into account all the elements that determine the minimum spatial resolution;
- 2) having decided on the spatial resolution, we build the computational domain consists of Yee cells and determines the sampling interval of time;
- 3) the different boundary conditions are imposed on the structure;
- 4) the discretized version of Maxwell's equations is applied cyclically with the leap-frog scheme injecting the forcing term due to field sources;
- 5) finished the calculation; the results are collected and are subject to possible post-processing.

In the first phase is determined by the quality of the calculation: in addition to the geometric complexity of the system to be analyzed, it is necessary to determine the frequency ranges of the radiation that it will invest and what effects may be prevalent.

In this section, we described the FDTD method for solving Maxwell's equations. This method is used for the problem of detecting buried objects and is the basis of the principle of resolution of GPRMax software that has been used for FDTD simulation in chapter 2. Next section will discuss in details the Ground Penetrating Radar with his application in Land Mines detection and Road monitoring.

1.3. Ground Penetrating Radar

1.3.1.Introduction

The basic theory behind the ground penetrating radar system has been in use since the early 1900's. The first known use of electromagnetic signals to locate remotely buried objects is attributed to Hulsmeyer with a German patent in 1904[22]. The system that Hulsmeyer used was a continuous wave transmission radar system. The pulse radar system, very much like present GPR systems, was not developed until the mid 1900's. In 1962, Husenbeck developed the first pulsed radar system to investigate buried features[23]. Today, pulse GPR systems are manufactured commercially for use in many geophysical fields.

Ground Penetrating Radar (GPR) has come into use over the last 20 years in civil engineering, geology and archaeology, for the detection of buried objects and for soil study. The detection of buried landmines has also been a subject of considerable interest, in particular due to radar's potential for the detection of plastic-cased mines which contain little or no metal. Today, a large number of organizations are working on different parts of GPR systems, and among all the sensors proposed for humanitarian demining; GPR has had by far the greatest research funding and effort dedicated to it.

GPR works by emitting an electromagnetic wave into the ground, rather than into the air as in many radar applications, using an antenna which does not need direct ground contact (in other domains direct contact is often required, e.g. non-destructive testing). GPR systems usually operate in the microwave region, from several hundred MHz to several GHz [24].

Buried objects, as well as the air-ground interface, cause reflections of the emitted energy, which are detected by a receiver antenna and associated circuitry. GPR can produce a fuzzy depth “image” by scanning the suspected area, and/or using an antenna array. The antenna is one of the most crucial parts of a GPR system. What particularly matters for the detection of objects in a background medium, e.g. mines buried in soil, is the difference between the electromagnetic properties of the target (in particular its dielectric constant) and those of the background (the GPR works as a target-soil electrical contrast sensor). The amount of energy reflected, upon which reliable detection is based, also depends on the object’s size and form. Spatial resolution depends on the frequency used, and the resolution needed to cope with the smaller anti-personnel landmines requires the use of high frequency bands (up to a few GHz). These higher frequencies are, however, particularly limited in penetration depth.

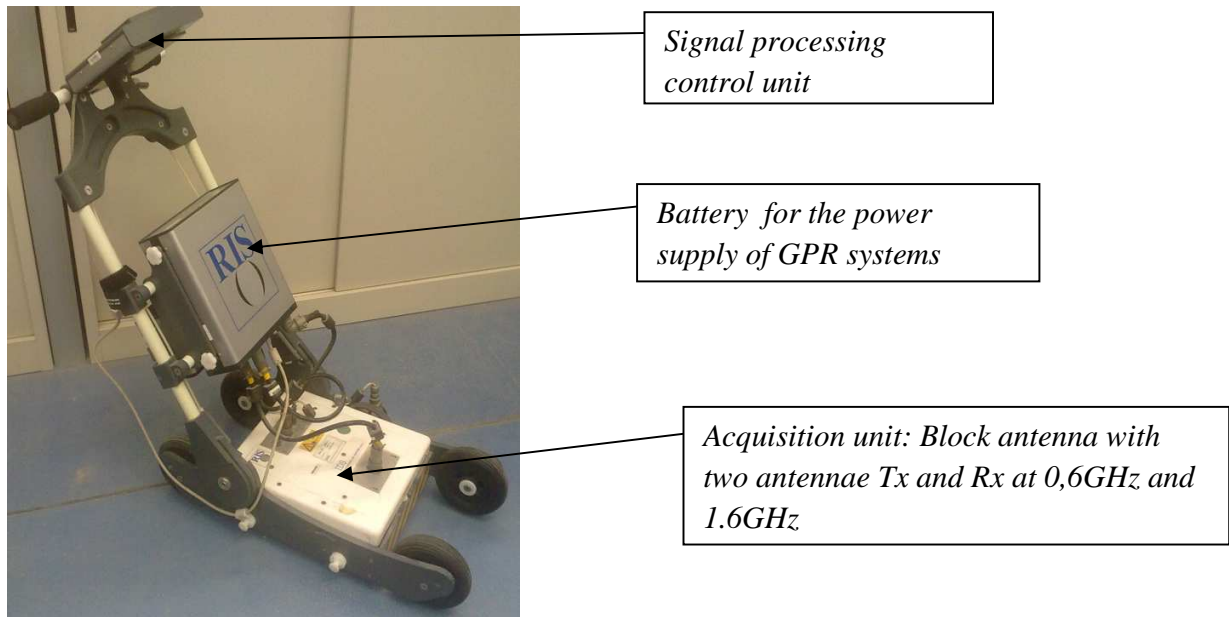


Figure 1.7. A physical GPR systems: impulse time domain

GPR systems can be subdivided into four categories, depending on their operating principle. The first type is an impulse time domain GPR, where the emitted pulse has a carrier frequency, modulated by a nominally rectangular envelope. This type of device operates in a limited frequency range, and has in most cases a mono-cycle pulse. The second type of time domain GPR is the so-called Chirp Radar, which transmits a pulse train waveform where the carrier frequency of each pulse is rapidly changed across the pulse width. Frequency domain GPR transmits a signal with a changing carrier frequency over a chosen frequency range. This carrier frequency is changed, either continuously, for example in a linear sweep (Frequency Modulated Continuous Wave Radar, or FMCW), or with a fixed step (stepped frequency radar). The term Ultra Wide Band (UWB) GPR is generally used for systems operating over a very wide frequency range (in relation to their central operating frequency).

1.3.2 Physical base

The GPR method operates by transmitting a very short electromagnetic pulse into the ground using an antenna. The centre frequency is typically in the range of 10-2000 MHz. Abrupt changes in dielectric properties cause parts of the electromagnetic energy to be reflected back to the ground surface, where it is recorded and amplified by the receiving antenna. The recorded signal is registered as amplitude and polarity versus two-way travel time (figure 1.7). The electromagnetic wave propagates in air with the speed of light (0.3 m/ns). In the ground, the velocity of electromagnetic waves is reduced since it is dependent on the relative dielectric permittivity, ϵ_r , the relative magnetic permeability, μ_r , and the electrical conductivity, σ . The velocity of electromagnetic waves in a host material is given by:

$$v = \frac{c}{\sqrt{\epsilon_r \mu_r \frac{1 + \sqrt{1 + (\frac{\sigma}{\omega \epsilon})^2}}{2}}} \quad (1.48)$$

where c is the electromagnetic wave velocity in vacuum (0.3 m/ns), $\epsilon = \epsilon_r \epsilon_0$ the dielectric permittivity and ϵ_0 the dielectric permittivity in free space ($8,854 \cdot 10^{12} \text{F/m}$), $\omega = 2\pi f$ the angular frequency, where f is frequency, and the expression $\sigma/\omega\epsilon$ is a loss factor. In non-magnetic ($\mu_r = 1$) low-loss materials, such a clean sand and gravel, where $\sigma/\omega\epsilon \approx 0$, the velocity of electromagnetic waves is reduced to the expression

$$v = c / \sqrt{\epsilon_r} \quad (1.49)$$

The equations 1.48 and 1.49 shows that the velocity of electromagnetic waves propagating in the ground is decreased compared to the velocity in the air. In low-loss (i.e. resistive) materials the maximum decrease is a factor of nine, which is the velocity of electromagnetic waves in fresh water (0.034 m/ns). Several processes lead to a reduction of the electromagnetic signal strength. Among the most important processes are attenuation, spherical spreading of the energy, reflection/transmission

losses at interfaces and scattering of energy. Scattering is due to objects with a dimension similar to the wavelength and is therefore most pronounced for higher frequencies. Special attention should be drawn to the attenuation, which is a function of dielectric permittivity, ϵ , magnetic permeability, μ , and electrical conductivity, σ , as well as the frequency of the signal itself, $\omega=2\pi f$. The attenuation coefficient is expressed as:

$$\alpha = \omega \sqrt{\epsilon \mu \frac{\sqrt{1 + (\frac{\sigma}{\omega \epsilon})^2} - 1}{2}} \quad (1.50)$$

In low-loss materials, where $\sigma/\omega\epsilon \approx 0$, the attenuation coefficient is reduced to

$$\alpha = \frac{\sigma}{2} \sqrt{\frac{\mu}{\epsilon}} \quad (1.51)$$

The attenuation is proportional to the electrical conductivity, which leads to high attenuation in materials with high electrical conductivity.

1.3.3.Data acquisition

Doing the measurements with GPR, it is necessary to describe what is the methodology to have the data. The following section gives the comprehensive advice and good practice in GPR field techniques.

Reflection profiling

In reflection profiling mode the antennae are kept at constant separation, while they are moved along a profile (figure 1.7). The electromagnetic pulses are transmitted at fixed time or distance interval. The signal is recorded and displayed immediately on a computer screen as GPR profiles, in which the vertical axis is two way travel time in nanoseconds and the horizontal axis is distance along the measured profile. The GPR

data are either collected along a single profile or in a grid of profiles to obtain 2D or pseudo 3D information on structures in the ground. The GPR data can also be acquired along lines so densely spaced that the line spacing equals the step size along the line. This leads to a 3D data cube, where data also can be displayed as time or depth slices.

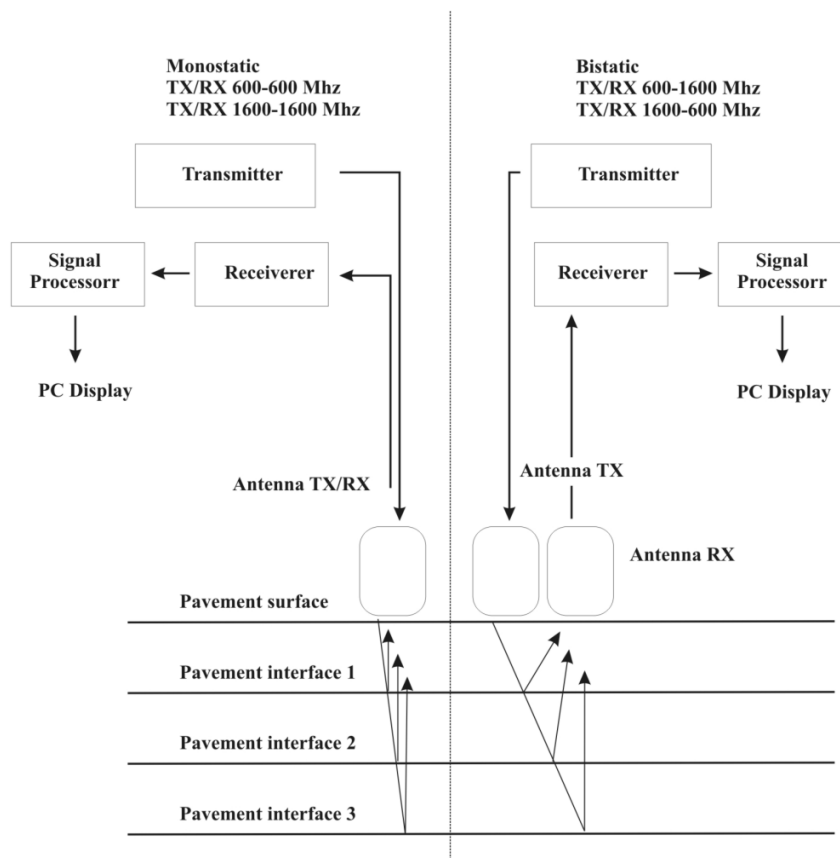


Figure 1.8. Principles of GPR in reflection profiling mode.

To ease the work in the field, the GPR system can be mounted on a car or sledge which is towed by a person or an all-terrain vehicle. The acquisition speed is comparable to walking speed for the most systems. The productivity per field day depends on the individual survey setup and the accessibility in the field. If there are topographic changes along the GPR profiles it is important that the topographic

variation is surveyed precisely, so that the GPR profiles can be displayed with correct topography. As a result the reflections will be displayed with the true dip and geometry.

Common mid point

A common midpoint (CMP) dataset is also called a velocity sounding, since the technique is commonly used for signal velocity establishment. In CMP mode the antennae separation is increased for each recording, while they are kept over a common midpoint.

A CMP plot contains the direct wave transmitted in the air above the ground, the direct wave transmitted in the ground and waves reflected from interfaces in the ground, where the dielectric properties change[25]. This is related to the fact that the electromagnetic wave velocity in a medium decreases with depth, together with increasing water content with depth.

1.3.4. Soil dielectric properties

Dielectric medium properties are a critical parameter for most methods, because the dielectrics control the contrast between the object of study and the medium it is buried in. Additionally the dielectric medium properties control propagation, attenuation, and reflection of electromagnetic waves. The dielectric properties of materials are a function of (among others): texture, bulk density, mineralogy, organic matter content, and frequency, but especially water content [26].

Soil data from a wide range of environmental settings (temperate, tropical, and desert), show that soil water content varies widely and over distances of less than one meter [27]. This variability has important implications for sensors that are affected by

the soil water content, as their performance may be variable over short distances. The performance of a sensor under specific soil conditions can be predicted using a thorough understanding of the physics of the soil-mine-sensor system.

To predict the performance of electromagnetic sensors it is common to use models that estimate the soil dielectric properties. Although a wide variety of models, each with its own characteristics, has been proposed, no complete model is available that can describe the dielectric properties of a soil for all its variables. This makes it a challenge to select the best model for each occasion.

1.3.3.1. Phenomenological models

Phenomenological models such as Cole-Cole [28] and Debye [29] relate characteristic relaxation times to frequency dependent behavior of a material. These models allow for assessment of complex dielectric properties for specific frequencies. The Cole-Cole relaxation model describes the induced polarization effects as a function of frequency. The complex dielectric permittivity can be described as [30]:

$$\varepsilon^*(f) = \left[\varepsilon_\infty + \frac{\varepsilon_s - \varepsilon_\infty}{1 + (jf/f_{rel})^{1-\beta}} \right] - \frac{j\sigma_{dc}}{2\pi f \varepsilon_0} \quad (1.52)$$

where ε_s and ε_∞ are the static value of the dielectric permittivity and the high-frequency limit of the real dielectric permittivity, respectively. For water ε_s and ε_∞ equal 80 and 4.22, respectively, depending on temperature. ε_0 is the dielectric permittivity of free space ($8.854 \cdot 10^{-12}$ F/m) [31]. f_{rel} is the dielectric relaxation frequency of the material (17.1 GHz for water [32]), σ_{dc} is the electrical conductivity and β is an empirical parameter to describe the spread in relaxation frequencies, which increases with the complexity of the mixture[33]. For distilled water, or other pure liquids with a single relaxation frequency, β is zero, resulting in the original Debye model[34]. For tap water and moist sandy soils β is 0.0125 and 0.3 according

to Heimovaara [35] and Roth et al[36], respectively. Some other values for β are reported in literature [37].

According to the Cole-Cole model the complex resistivity or impedance can be expressed as:

$$R^*(\omega) = R_0 \left\{ 1 - m \left(1 - \frac{1}{(1+j\omega\tau)^c} \right) \right\} \quad (1.53)$$

where R_0 is the dc resistivity, m is a variable (0.1-1.0) depending on the mineral content, ω is the (radial) frequency, τ (range 10^{-4} - 10^4) is the time constant, and c is a variable (0.2-0.6) depending on the grain size distribution. Roth et al. report a value of 8 for τ in moist sandy soils [38]. τ values for different materials have been reported in the literature[39].

As seen from the formulations above phenomenological models need recalibration for each specific material. Therefore, it is difficult to use these models to describe the dielectric differences between varying soil types.

1.3.3.2. Volumetric models

Volumetric models describe the dielectric properties of a soil based on the relative amounts of the different soil constituents and their individual dielectric characteristics. The basic input parameters to all models include solid matter, pore space, and volumetric water content. Depending on the model, input variables such as organic matter and bound water may provide additional accuracy for specific conditions. Usually, frequency dependence is not taken into account.

The models have been calibrated, for example, by time-domain reflectometry. Over the years different volumetric mixing models have been proposed [40] that can be grouped in different types such as Arithmetic Average, Harmonic Average, Liechtenecker - Rother, and Time-Propagation [41]. The Complex Refractive Index

(CRI) model or exponential model, which is based on the Liechtenecker-Rother model, is one of the most popular methods[42]. The CRI model for a material with n components can be written as:

$$\varepsilon_m^\alpha = \sum_{i=1}^n v_i \varepsilon_i^\alpha \quad (1.54)$$

where v_i is the volume fraction of the i^{th} soil constituent, and α is an empirical variable (0.5 according to some authors[43]). The scaling factor α gives CRI and other volumetric mixing models a semi-empirical nature. The α parameter can theoretically vary from -1 to $+1$ but for multiphase mixtures such as soils values between 0.4 and 0.8 have been found. Other values for α reported in the literature are 0.3345, 0.46 for three-phase systems and 0.65 for four phase systems including bound water. Several attempts have been made to give more physical basis to the scaling factor. It has been shown that the value of α also (inversely) correlates with the measurement frequency[44].

Recently, a new volumetric mixing equation based purely on the depolarization factors of different soil constituents has been introduced. This model has a strong theoretical basis and tries to overcome some problems that exist in other volumetric mixing models. In this approach the measured permittivity is related to the volume-weighted, sum of the permittivity of the individual material constituents. A depolarization factor (S) is introduced to account for electric-field refractions at the material interfaces. In this mixing equation:

$$(\varepsilon - 1) = \sum_{i=1}^n (\varepsilon_i - 1) S_i v_i \quad (1.55)$$

where v_i is the volume fraction of the i^{th} soil constituent, S is related to the electric field refraction in soil, which is in turn a function of the shape and surface roughness of the grains. Theoretically, the depolarization factor can be calculated for all materials but currently this is only possible for homogeneous materials with regular shaped grains.

1.3.3.3. (Semi-) Empirical models

Empirical models are mathematical descriptions of the relationship between dielectric properties and other characteristics of a medium, especially volumetric water content and texture information. There is not necessarily a physical basis for the mathematical description. Therefore, an empirical model may only be valid for the data that were used to develop the relationship. Many empirical models have originated in the field of time-domain reflectometry (TDR), and were originally used to predict the soil water content from the velocity of electromagnetic signals along TDR probes in the soil.

The classic Topp model uses a third order polynomial to describe the relation between soil volumetric water content (θ) and bulk or apparent relative permittivity (K_a) for measurements taken below the relaxation frequency of water:

$$K_a = 3.03 + 9.3\theta + 146\theta^2 - 76.7\theta^3 \quad (1.56)$$

The regression is an average of TDR measurements integrated over a frequency range of 1 MHz to 1 GHz for several soils and has proved very successful for a wide range of different soils and soil moisture conditions. Ledieu et al.[45] propose a linear relationship between soil water content and K_a , which can be used to expand the Topp model for higher water contents. The model functions especially well for frequencies

around 100 MHz. At higher frequencies and moisture contents close to saturation ($\theta \sim 0.4$) the Topp-model over-predicts the bulk relative permittivity by up to 20%.

At very low water contents the Topp-model does not perform well, especially for soils with large clay content. There exist various empirical models similar to equation (1.56) that are suitable for specific soil conditions. The bulk density has a profound effect on the relation between θ and K_a . Soils with high content in organic matter usually have a lower bulk density. Conversion functions have been proposed to account for the bulk density and porosity variations between organic and mineral soils. Dielectric measurements of samples high in organic matter content show that equation (1.56) may under-predict θ by about 30%. An alternative function has been proposed to account for this effect. The presence of aligned ellipsoidal particles, for example in bedding planes of sedimentary deposits, also has an effect on the effective permittivity.

Brisco et al. [45] present results for measurements with a field portable dielectric probe (PDP) at different frequencies ranging from 0.45 to 9.3 GHz. The measurement variability is rather large and the number of soils studied is small. As a result, the third-order polynomial functions that are presented for each frequency may contain a significant error. At frequencies below around 50 MHz the dielectric permittivity depends strongly on soil type. Based on measurements of 6 soils at 1, 5, and 50 MHz it is shown that at the lower frequencies the soil type has a strong impact on both ϵ' and ϵ'' .

Third-order polynomial functions for the data measured at 1 MHz and 50 MHz are given. Also data presented show that the effects of changes in volumetric water content and soil water temperature on the relationships between frequency (1-50 MHz) and ϵ^* . Semi-empirical models are powerful and useful hybrids between empirical models and volumetric models. These models often use a volumetric mixing model as their base and have been calibrated for a specific set of soils. The

models include information of physical background of dielectric behavior. They are sometimes able to describe frequency dependent behavior, but may only be valid for the data that were used to develop the relationship. The models by Dobson and Peplinski use input of the percentage of clay and sand in a soil, as well as the volumetric water content and bulk density to calculate the complex frequency dependent properties of field soils. The model by Hilhorst uses Debye relaxation parameters, which is related to textural characteristics, and a semi-empirical parameter S , to calculate the complex frequency dependent soil properties.

1.3.5 Penetration depth

The penetration depth is controlled by the GPR centre frequency, the electrical conductivity and the attenuation of the subsurface deposits. In low-loss deposits, a low centre frequency achieves a large penetration depth whereas a high centre frequency results in a lower penetration depth. The literature on GPR investigations in sediments reports on penetration depths of up to about 30-40 m for 40–50 MHz, of 10–25 m for 100 MHz, 5–15 m for 200 MHz and only a few meters for 500– 1000 MHz. The maximum penetration depths are obtained in dry clean sand and gravel [46] or sandstone [47].

How fast the GPR signal is attenuated depends primarily on the electrical conductivity of the ground [48]. In pure dielectric materials the signal is attenuated very slowly, whereas in conductive materials such as clay or deposits with saline pore water the attenuation is very fast and the penetration depth is decreased significantly. Using a 100 MHz GPR system on clayey deposits, the penetration depth is limited to a few meters. Application on a deposit with saline pore water allows a penetration of a few centimeters only.

In the landmine detection, field GPR have shown that soil can have a very effect on the performance of GPR systems for buried landmine detection. Under some soil conditions the landmine signature is of high quality while under others no signature can be detected at all.

1.3.6 Resolution

The vertical resolution depends primarily of the wavelength, λ , of the propagating electromagnetic wave, which is determined by the GPR frequency, f , and velocity, v , of the ground material as $\lambda=v/f$. Theoretically, the distance between two reflectors should at least be $\frac{1}{4} - \frac{1}{2}$ of the wavelength to be resolved [49], though in practice the distance should be $\frac{1}{2} - 1$ wavelength [50]. Using a $\frac{1}{2}$ wavelength, the vertical resolution in dry sand with a velocity of 0.15 m/ns is about 1.5 m, 0.75 m and 0.19 m for a 50 MHz, 100 MHz and 400 MHz centre frequency, respectively. In saturated sand with a lower velocity of about 0.06 m/ns, the vertical resolution is 0.6 m, 0.3 m, and 0.075m for a 50 MHz, 100 MHz and 400 MHz centre frequency, respectively. The lateral resolution depends on more than the wavelength of the propagating electromagnetic wave. The depth to the target as well as the antennae focusing plays a part. Neal[51] discusses in detail the different aspects that have to be taken into account in the evaluation of the lateral resolution. In the following chapters, we will discuss largely on the field application of the GPR in landmine detection and in the road monitoring.

Chapter 2: FDTD Simulations and GPR Measurements for Land-Mine Detection

2.1.Introduction

In the last decades, many countries have been affected by wars that have left the territory plagued by Explosive Remnants of War (ERW), like mines, cluster bombs and unexploded objects: Afghanistan, Angola, Burundi, Cambodia, Democratic Republic of Congo, Iran, Iraq, the former Yugoslavia, Pakistan, and Rwanda are only a few examples. Clearing terrains from ERWs, is a difficult and dangerous task, that is made harder by variability of environmental variables (e.g.: earth composition and humidity, climate, and vegetation) and by modifications happening over time (displacement and covering of objects).

Cost of clearance (typically \$300-1000 per item removed) is a limiting factor that prevents substantial progress (200,000 mines removed each year, compared to some 100,000,000 on the ground). Such cost, as well as slowness and danger of clearing operations, is largely determined by the difficulty of locating buried ERW, especially those that have very low metal content. As a result, different sensors, active or passive, have been used to analyze soils: transducers that measure electromagnetic fields, vibrations, thermal anomalies, and even molecular properties have been employed or proposed. Particular interest has been focused on Ground Penetrating Radar (GPR) systems[52], they are versatile and can work in conjunction with other techniques to reduce probability of false alarms. Moreover, they can successfully detect buried non-metallic objects because they can see the contrast among materials characterized by different dielectric constants.

Ground Penetrating Radars (GPRs) have been considered by several authors for antipersonnel mine detection [53] and tested on the field with encouraging results. Optimization of GPR performance for such tasks, in terms of probability of detection and discrimination, requires full comprehension of the scattering mechanisms of mines and confounders, and knowledge of the intrinsic limits of the technology, appropriately related to soil properties. Thorough characterization of ideal performance may be obtained from parametric simulation in a wide range of configurations, based on reliable modeling of the soil-mine/confounder system, which must be validated through experimental measurements.

To improve antipersonnel mine detection, the use of a GPR system is foreseen. However, an assessment of electromagnetic scattering due to the finite volume of the soil sample in the indoor laboratory had to be performed. In fact, the discontinuities among soil, wood walls, air, and concrete basement could introduce spurious echoes interfering with buried-object response. Because of its versatility (i.e.: non homogenous materials and wide-band pulses are easily represented) the Finite Difference Time Domain (FDTD) method has been employed to perform the above task: after benchmarking different implementations, giving priority to the ease of use, the freely-available simulator GprMax[54], has been successfully employed to carry out 2D and 3D simulation who whose compared with the GPR measurement in a controlled environment.

2.2.FDTD Simulation of GPR Measurements in a Laboratory Sandbox for Landmine detection

2.2.1.Introduction

The main objective of this section, is to make sure that, could be revealable making GPR measurements, the scattered field by the mine in the laboratory of Cisterna di Latina. In fact, doing the FDTD simulation we can see how is the system response to be compared with the GPR measurements.

2.2.2.Simulation Setup

The figure 2.1. shows the laboratory setup of Humanitarian Demining Laboratory (HDL), where the sandbox contains two buried surrogate mines[55] and other objects of different nature (confounders).

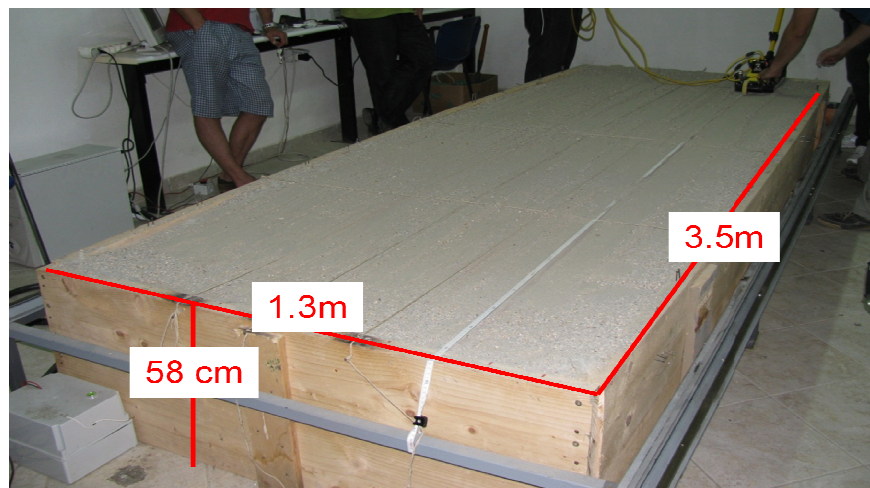


Figure.2.1. The Humanitarian Demining Laboratory box, $(1.3 \times 3.5 \times 0.5) \text{ m}^3$, placed on a concrete basement, filled by sand and confined by wood walls.

Since one dimension, 3.5 m, is larger than the others, assuming the object

sufficiently far from wood walls that contain the sand, and taking into consideration the goal of the simulation, calculations can be performed on the smallest cross section of the sandbox, reducing the number of dimensions to two (figure 2.2). Such simplification decreases simulation time and memory allocation, thus letting us modulate resolution accordingly. As a result, the mine under examination has been represented as in figure 2.3, reasonably modeling a real one [17]. The sandbox cross section, whose size is $(1.3 \times 0.5) \text{ m}^2$, is placed on a concrete basement (relative dielectric constant $\epsilon_r = 6$ and conductivity $\sigma = 5 \times 10^{-3} \text{ S/m}$) between two 0.025 m thick wood walls ($\epsilon_r = 2$, $\sigma = 10^{-4} \text{ S/m}$). The sand has been supposed to be dry ($\epsilon_r = 5$, $\sigma = 10^{-4} \text{ S/m}$): in fact, if it were wet, the electromagnetic field, due to a higher conductivity, would attenuate faster, hiding possible back-scattered undesired components [22].

The virtual monostatic GPR has been placed at 0.02 m above the air-sand interface, point “a” in figure 2.2, at $x = 0.65 \text{ m}$, and the mine at 0.14 m below the transmitting antenna. Electromagnetic field has also been recorded in points “b” and “c” for two reasons: the first one was to check that the moduli of the components were identical due to system and impressed field symmetry, and the second one was to have an evaluation of scattered radiation against a person working nearby. The same holds for locations “e” and “f”. Additionally, the field was recorded in “d” to evaluate the maximum amount of back-scattering due to concrete reflecting back towards the mine.

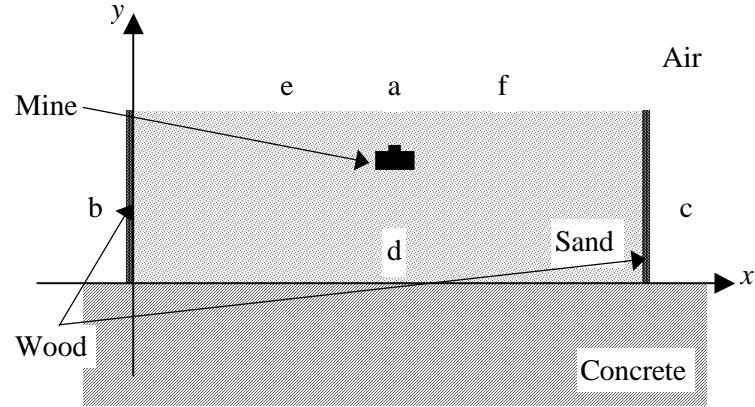


Figure 2. 2. The cross section of the sandbox, $(1.3 \times 0.5) \text{ m}^2$, where an object resembling a mine has been placed 0.12 m below surface. The GPR transmitting and receiving antenna (a) is 0.02 m above the air-sand interface. Additional receiving antennas have been provided for (b, c, d, e, and f).

The modeled mine (figure 2.3) is 0.08 m wide and 0.05 m high and made up by plastic ($\epsilon_r=2$, $\sigma=0$), air, and explosive ($\epsilon_r=3.5$, $\sigma=0$).

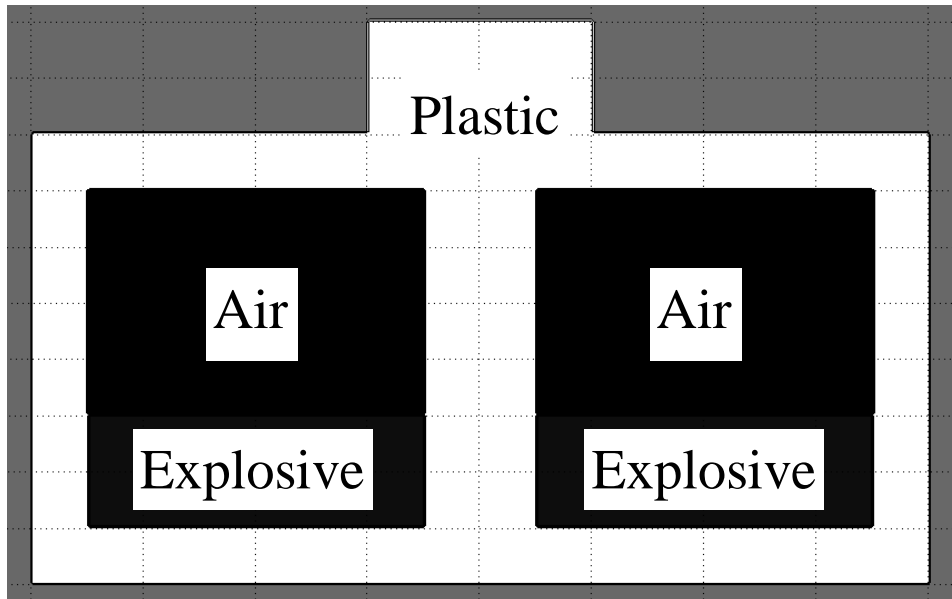


Figure 2. 3. Cross section of the $0.08 \text{ m} \times 0.05 \text{ m}$ cylindrical mine, made up by explosive and air enclosed by a plastic shell into two cavities.

The computational domain has been set up using a two-dimensional grid with

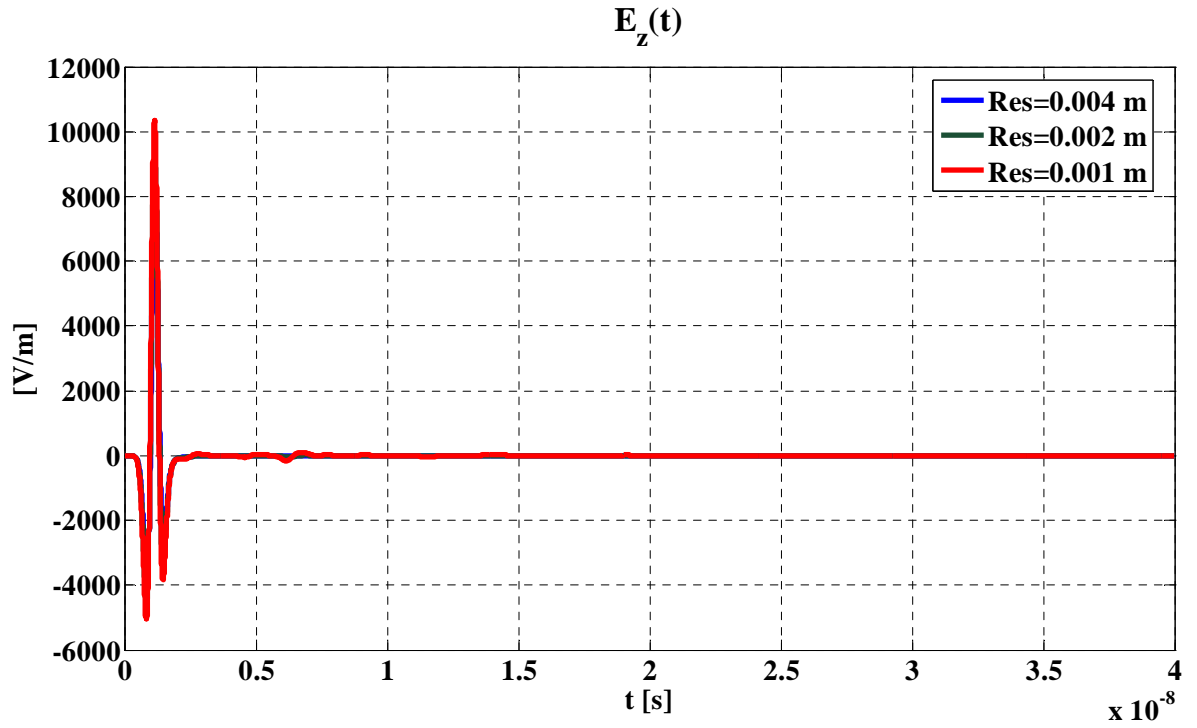
the leap-frog algorithm: because the cross section is on the (xy) plane, the field components that have been calculated as a function of time t , were $H_x(t)$, $H_y(t)$, and $E_z(t)$ [53]. It is possible to obtain the missing components by applying the duality property of Maxwell equations. The GPR transmitter was supposed to be a current line source, excited by a normalized differential Gaussian pulse [56], whose spectrum has its maximum at 900 MHz. Since at about 2 GHz (0.15 m wavelength in vacuum), power spectrum drops by 10 dB, and the smallest dimension in the domain was 0.05 m, start resolution was fixed to 4×10^{-3} m. Every time a simulation was performed, the FDTD-algorithm time step was calculated satisfying the Courant condition [57].

The simulation duration has been chosen to be 4×10^{-8} s, about four times the time needed for light to cover the longest distance in the computational domain supposing it to be filled with the densest dielectric.

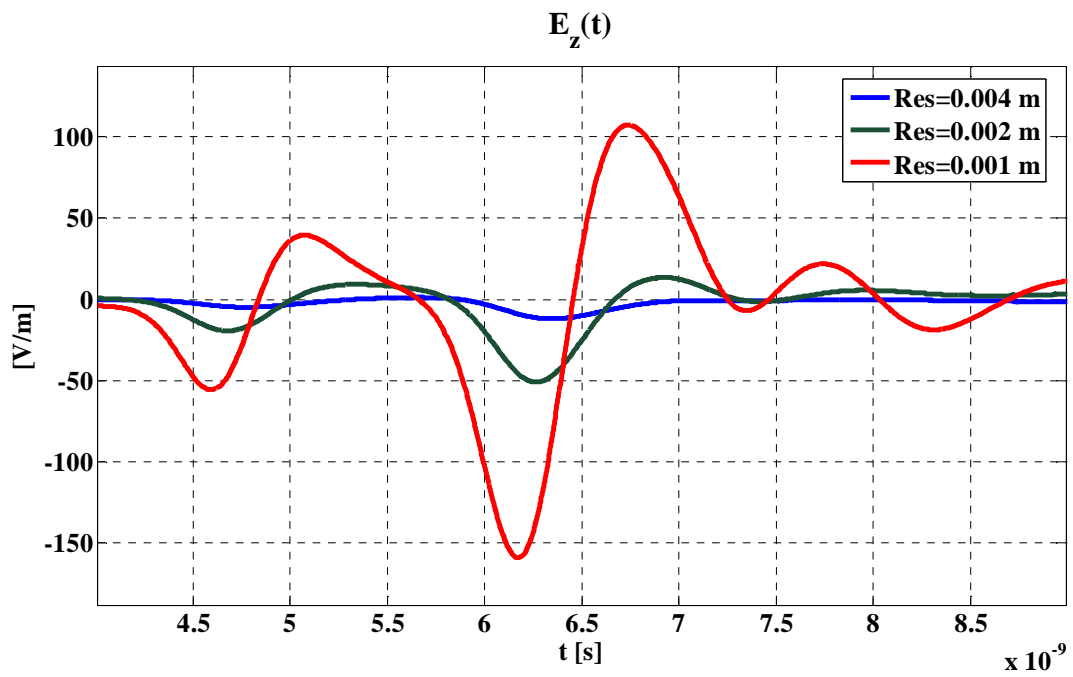
2.2.3. Results

Different simulations were carried out to approach the electromagnetic scattering problem to be solved. First, an ideal situation, where the environment was made up by air ($y \geq 0.5$ m) and sand ($y < 0.5$ m) only, was considered. After that, wood walls and concrete basement were introduced, confining the region filled with sand into a box. If not explicitly specified, all results are recorded in the “a” location (figure 2.2).

In the first stage, calculations in air, air with sand, and air with sand and buried mine were performed. Simulations in air showed a growing unexpected echo, when increasing resolution (figure 2.4. (b)). Since neither the mine nor the sand was in the domain, there was nothing that would cause a reflection.



(a)



(b)

Figure 2.4. Electric field along z axis versus time for different resolutions(a). As resolution increases, a spurious echo appears, as shown in the close-up(b).

The delay of the echo suggested that there could be a problem with the default boundary conditions, which rely on the Higdon model [52]. Switching to the Berenger's Perfectly Matched Layer (PML), the echo disappeared as resolution was being increased.

To obtain the field scattered by the mine, the field recorded for simulations without the buried object is subtracted from the one recorded when the mine is present. So, the result does not take into account the first reflection due to the air-sand interface but depends on how deeply the object is placed.

To have a first appraisal of simulation accuracy, two different sets of results have been obtained:

- for each resolution, from the z -component of the electric field scattered by the mine, $E_z^s(t)$, we subtracted the one recorded for the calculations at the maximum resolution (figure 2.5), obtaining a first assessment of simulation accuracy (figure 2.6) [17];
- for the maximum resolution, the y -component of the magnetic field, $H_y^s(t)$, has been recorded since it gives an evaluation of absolute simulation accuracy.

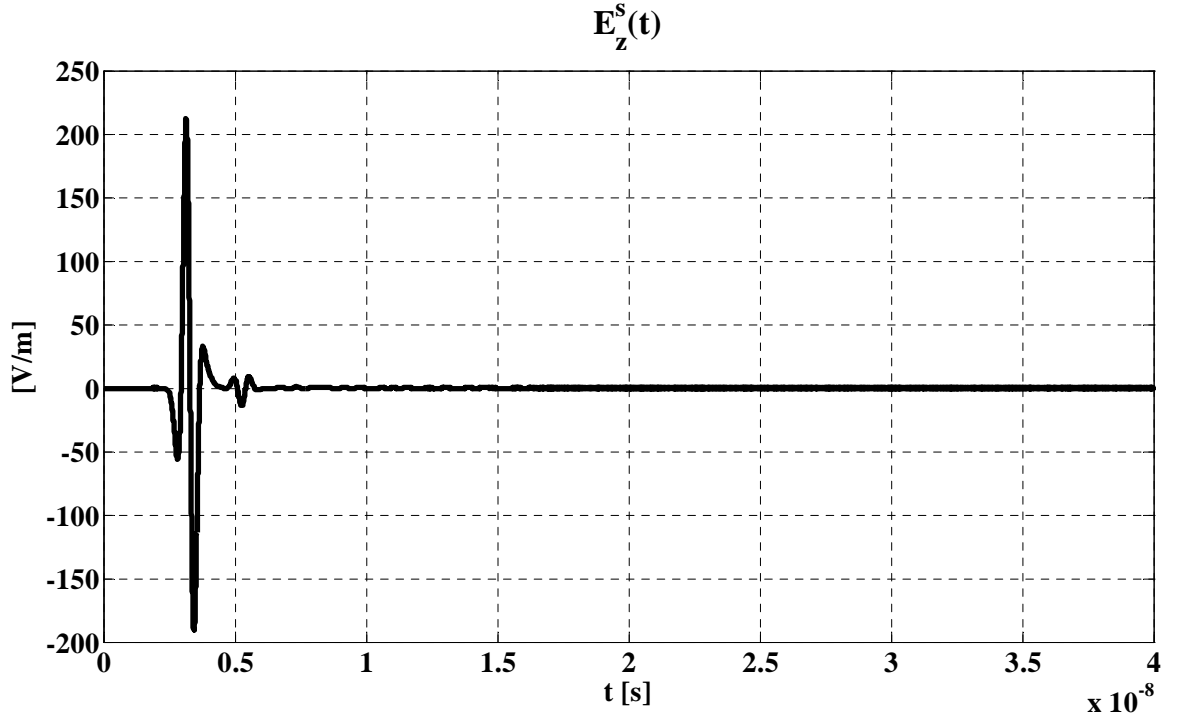


Figure 2.5. z -component of the electric field, $E_z^s(t)$, scattered by the buried mine for the 0.0005 m resolution.

As the computational-domain grid gets denser, the absolute error decreases and spurious echoes like the one at $t=9 \times 10^{-9}$ s disappear (figure 2.6). A close-up of absolute error evaluation has been provided for in figure 2.7.

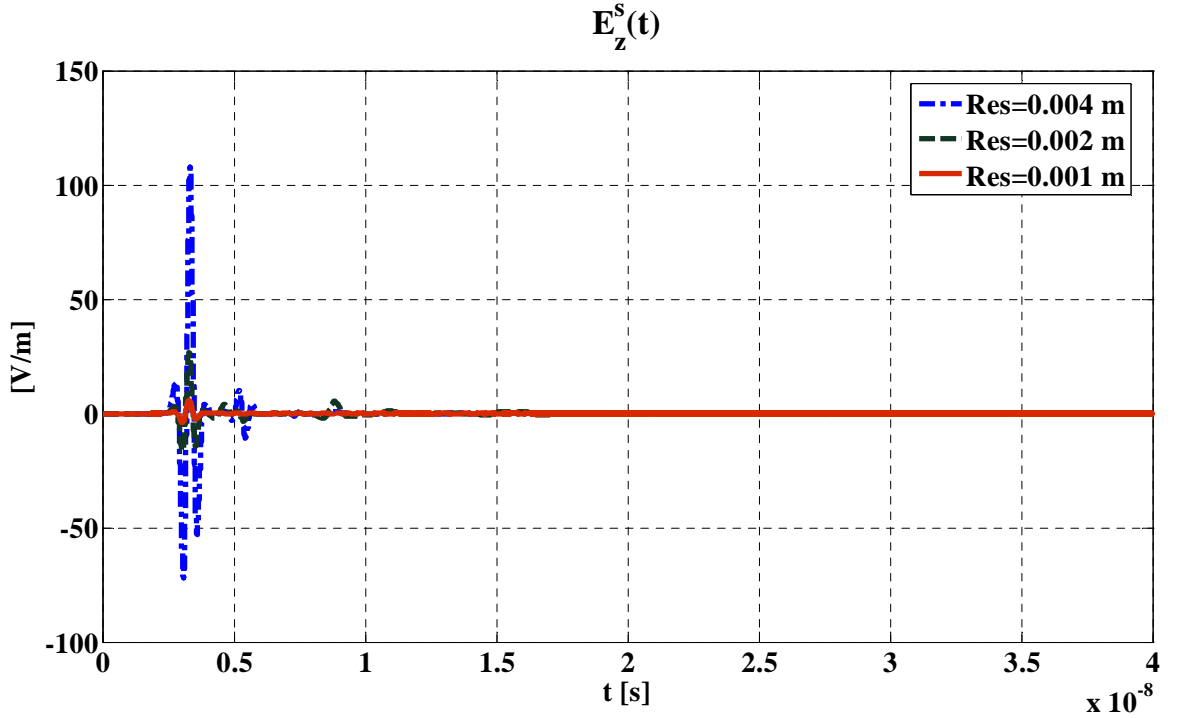


Figure 2.6 Difference between the z -component of the electric field, $E_z^s(t)$, scattered by the buried mine for three resolutions and the one recorded for the 0.0005 m resolution.

An estimate of the simulation accuracy at a given resolution may be calculated dividing the modulus of the maximum of figure 2.6 by the peak modulus of the scattered electric field $E_z^s(t)$, reported in figure 2.5. In this way, for the 0.001 m resolution, the relative error is about 2.8% and it is reasonable to assume that, halving the resolution (0.0005 m), a more accurate simulation may be achieved.

Since the field is recorded in air, the maximum peak, either positive or negative, of $H_y^s(t)$ lets us evaluate the possible absolute accuracy of the simulation (figure 2.8): scaling the magnetic component with free-space impedance, an equivalent 0.1 V/m electric field is obtained. This value is plausible with the orders of magnitude of relative errors previously calculated, since it is about 2% of the maximum value of the estimated absolute error for $E_z^s(t)$ using the 0.001 m resolution (figure 2.6).

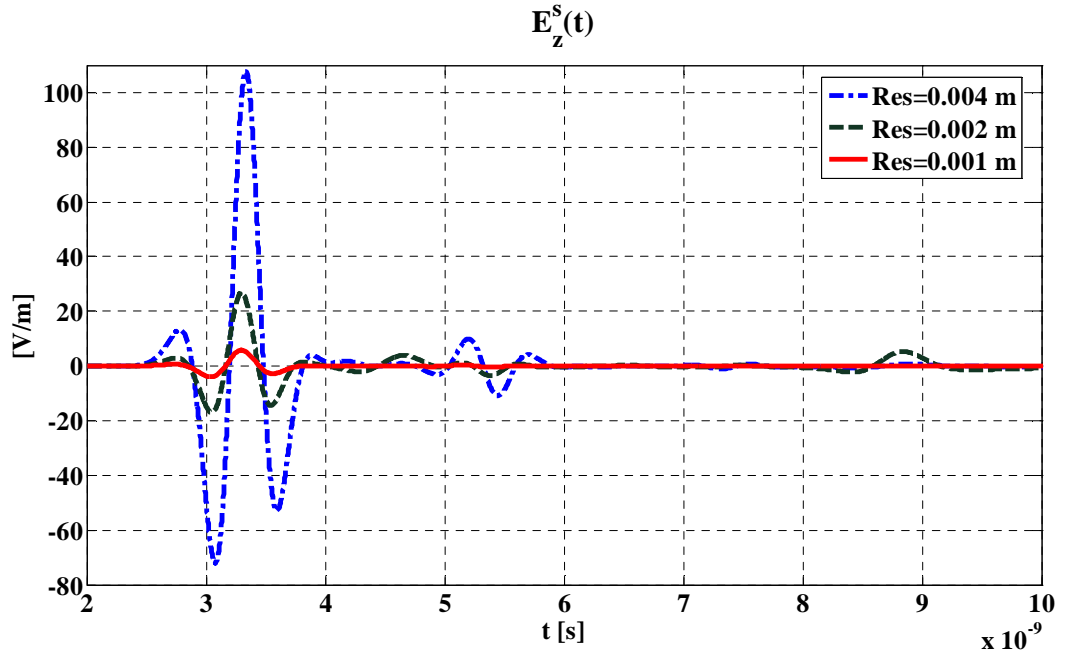


Figure 2.7. Close-up of the difference for the z -components of the electric field, $E_z^s(t)$ in figure 4.6, for $t < 10^{-8}$ s.

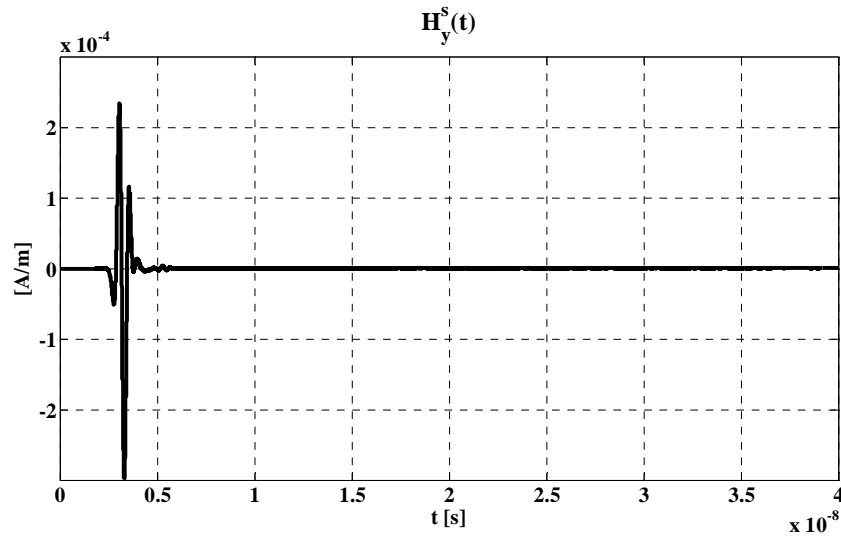


Figure 2.8. y -component of the magnetic field $H_y^s(t)$, scattered by the buried mine for the 0.0005 m resolution.

As a second stage, the presence of sand in the box is considered. Repeating the simulations, a behavior identical to the one in the first stage is obtained as resolution increases. However, because the sand is now confined, spurious echoes are observed (figure 2.9).

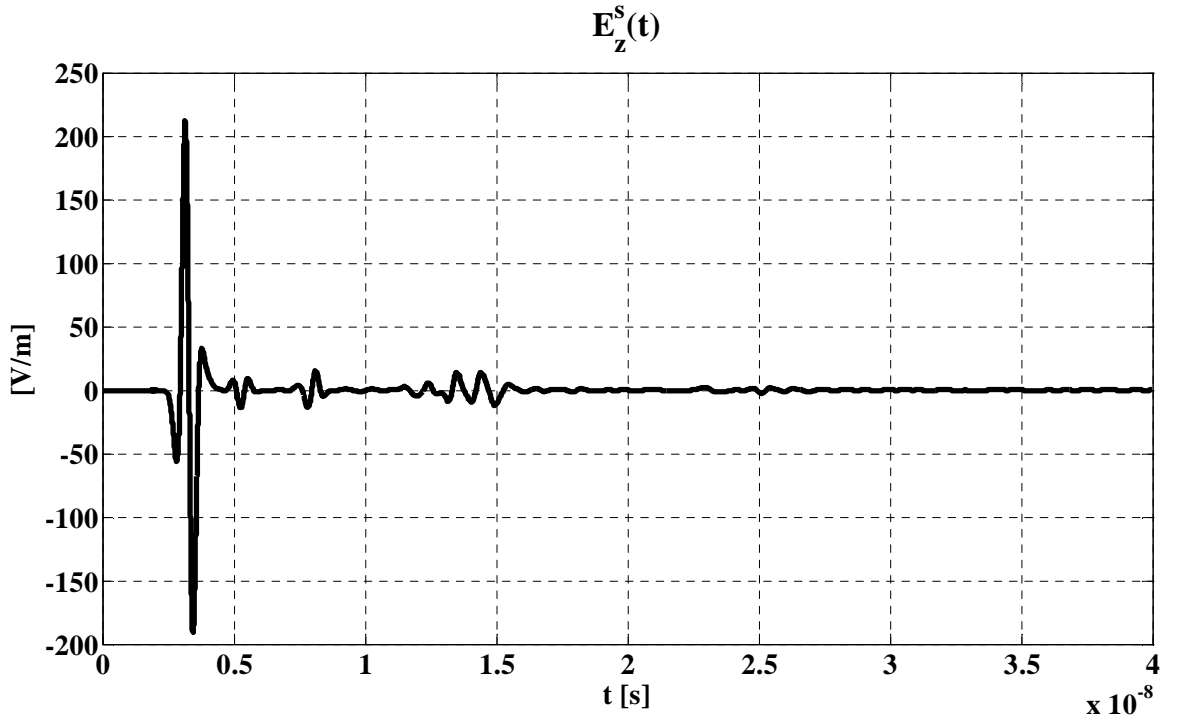


Figure 2.9. z -component of the electric field, $E_z^s(t)$, scattered by the buried mine for the 0.0005 m resolution, in the laboratory setup.

By comparing the results in figure 2.9 and in figure 2.5, it is possible to estimate the effect of the laboratory setup. To this aim, we report in figure 2.10 the difference between $E_z^s(t)$ calculated in the presence of sand inside the box and $E_z^s(t)$ for the case of an empty box.

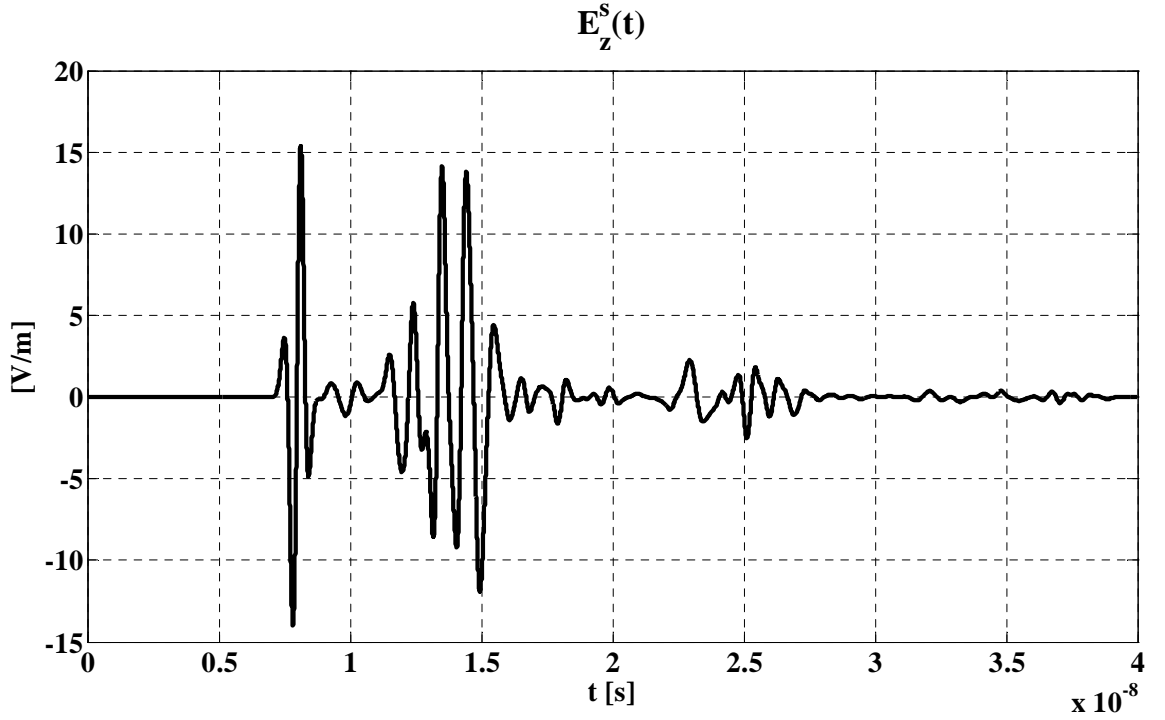


Figure 2.10. Difference between the z -component of the electric field, $E_z^s(t)$, scattered by the buried mine in the laboratory setup, and the one for the first stage (0.0005 m resolution).

The undesired electromagnetic field component maximum amplitude, scattered by the laboratory setup interfaces, is about 7.3% of the mine ideal peak response (figure 2.9). Such value is higher than the estimated error due to the resolution choice, confirming that there is no need to increase the computational-domain grid density.

The speed of light in a material like dry sand ($\epsilon_r=5$) is lower than in the air: to cover 1 m, it takes about 7.5×10^{-9} s, very close to the amount of time necessary for an electromagnetic wave to reach the sand-concrete interface and come back again (figure 2.10 and figure 2.2). Such hypothesis is supported by the measure of $E_z^s(t)$ below the mine (figure 2.11), in location “d” (figure 2.2), where the unwanted echo shows up starting at 4×10^{-9} s.

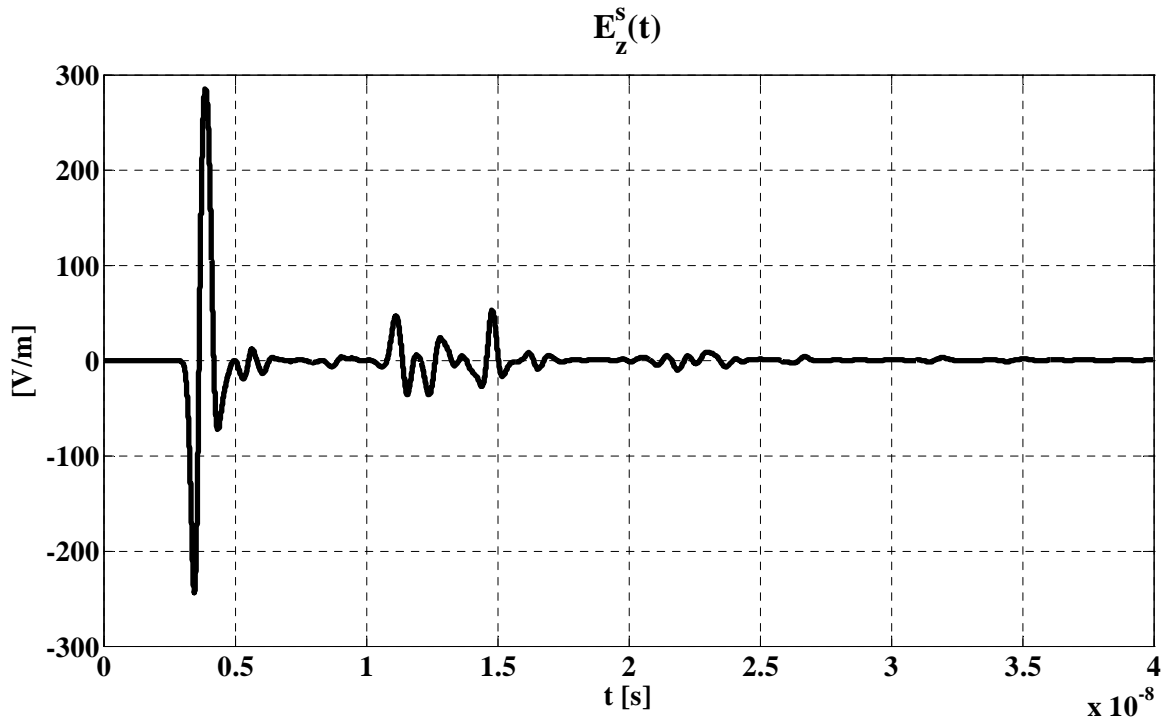


Figure 2.11. z -component of the electric field, $E_z^s(t)$, measured in “d” (figure 2.2), located at 0.1 m above the sand-concrete interface, for the 0.0005 m resolution, in the laboratory setup.

The other unwanted scattered components, for $t > 10^{-8}$ s (figure 2.10), are due to the echoes coming from all the interfaces confining the box: such conclusion can be drawn because the higher peaks’ order of magnitude is the same, whereas the field underneath the mine decreases by a factor of about 4 (figure 2.7).

Comparing figure 2.10 and figure 2.9, it is evident that the undesired echoes coming from all the interfaces are about ten times smaller than the signal indicating the presence of the buried mine (figure 2.9). Antennas in GPR systems are not isotropic on the (xy) plane, as the one considered in this chapter, therefore a higher directivity towards the y direction is to be considered and reflections from the lateral interfaces decrease. On the other hand, it is expected that the ratio between the magnitude of the field back-scattered by the sand-concrete interface and the one scattered by the mine will not change appreciably. So, it is possible to conclude that

figure 2.10 depicts the “worst case”.

In figure 2.12, for $t > 10^{-8}$ s, additional spurious scattered components for $H_y^s(t)$ are observed: comparing their maxima to the ones in figure 2.8, it is clear that all the disturbing echoes due to the laboratory-setup interfaces, do not influence the simulation accuracy.

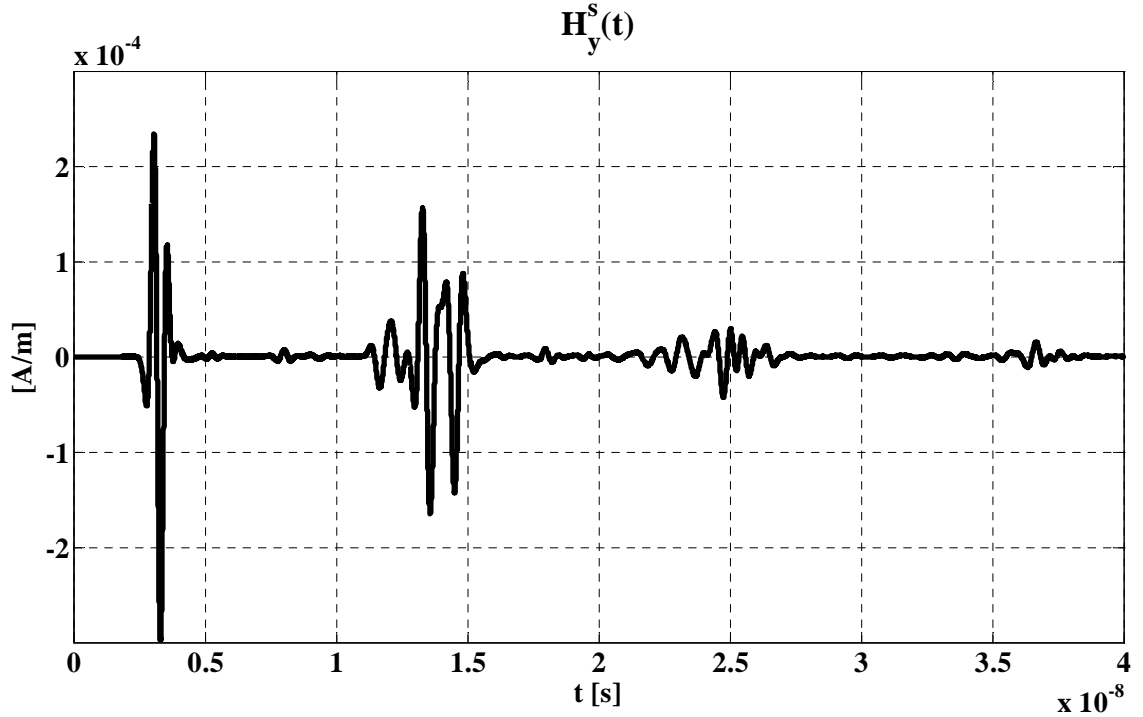


Figure 2.12. y-component of the magnetic field $H_y^s(t)$, scattered by the buried mine for the 0.0005 m resolution, in the laboratory setup.

Comparing the fields calculated for resolution 0.0005 m, at locations “e” and “f” (figure 2.2), the same results are obtained. This happens for “b” and “c”, too.

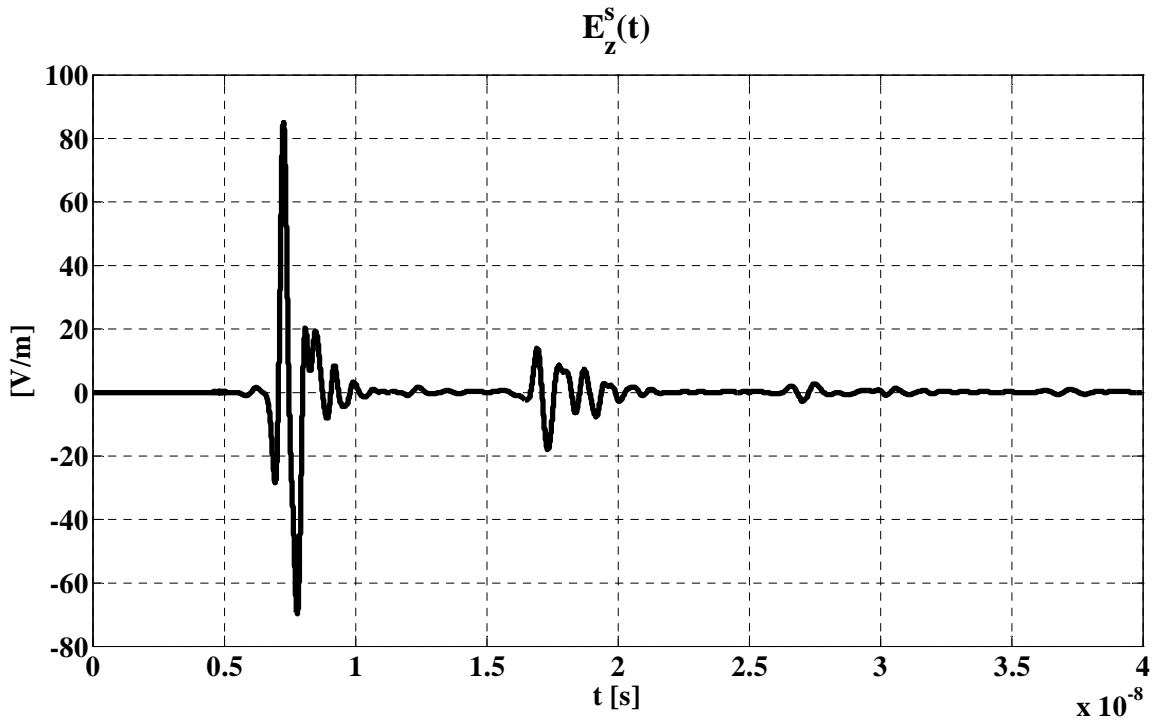


Figure 2.13. z -component of the electric field, $E_z^s(t)$, measured in “b” or “c” (Figure 2. 2), for the 0.0005 m resolution, in the laboratory setup.

The amplitude of the electric field near the wood walls (figure 2.13) is 40 dB lower than the peak of $E_z^s(t)$ in air (b). If the antenna were more directive, the field would be lower accordingly. The evaluation of field attenuation near the wood walls lets us calculate the power at which an operator in the laboratory would be exposed. An observer standing near the GPR device, would experience a field 25% stronger, instead (figure 2.9).

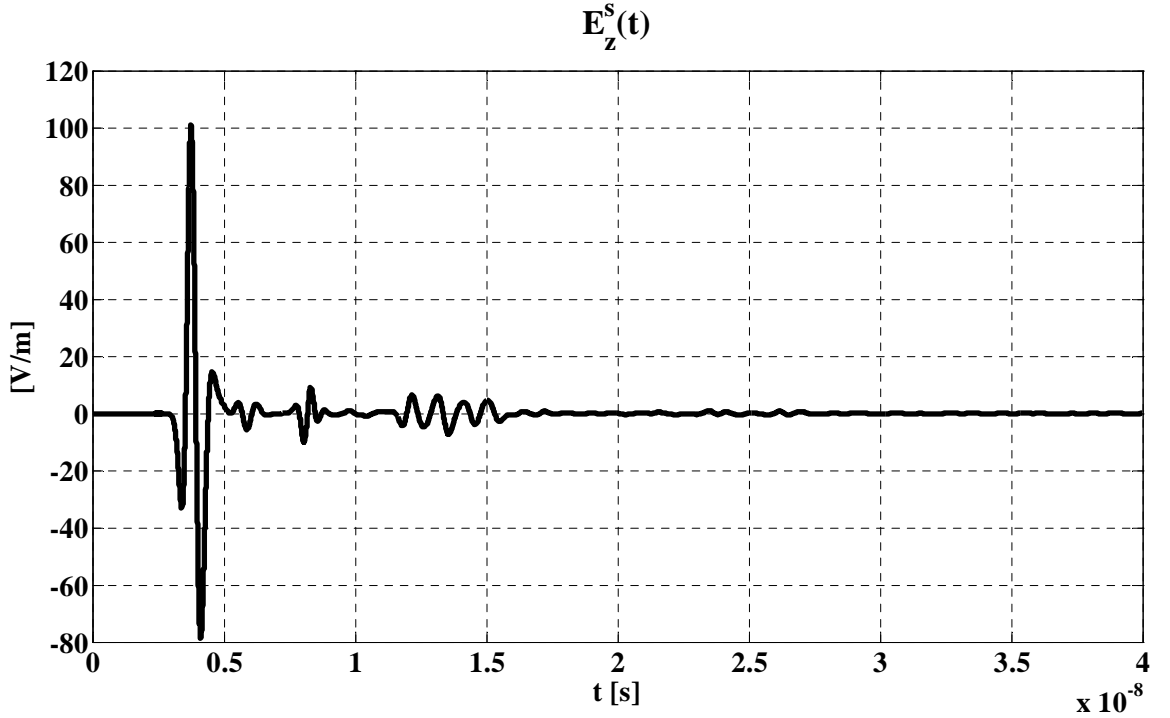


Figure 2.14. z -component of the electric field, $E_z^s(t)$, measured in “e” or “f” (Figure 2. 2), for the 0.0005 m resolution, in the laboratory setup.

As the amplitudes of unwanted backscattered electromagnetic-field contributions due to the experimental setup, with respect to the results obtained for the first stage, are lower than 10%, it is possible to conclude that the sandbox of the Demining Laboratory, “Sapienza” University of Rome, at Cisterna di Latina, Italy, is adequate for benchmarking GPR performances: measurements can therefore be taken into consideration for comparison to the other demining techniques examined in the same facility. For this reason the next section will discuss the comparison of the FDTD simulation with a GPR measurement in a controlled environment.

2.3.GPR Measurements and Tree-dimensional FDTD Simulations.

2.3.1.Introduction

In this section, using three-dimensional Finite Difference Time Domain (FDTD) simulations, the electromagnetic field scattered by five different buried objects (figure 2.15) has been calculated and the solutions have been compared to the measurements obtained by a GPR system on a $(1.3 \times 3.5 \times 0.5) \text{ m}^3$ sandbox, located in the Humanitarian Demining Laboratory at Cisterna di Latina, to assess the reliability of the simulations. A combination of pre-calculated FDTD solutions and GPR scans, may make the detection process more accurate.

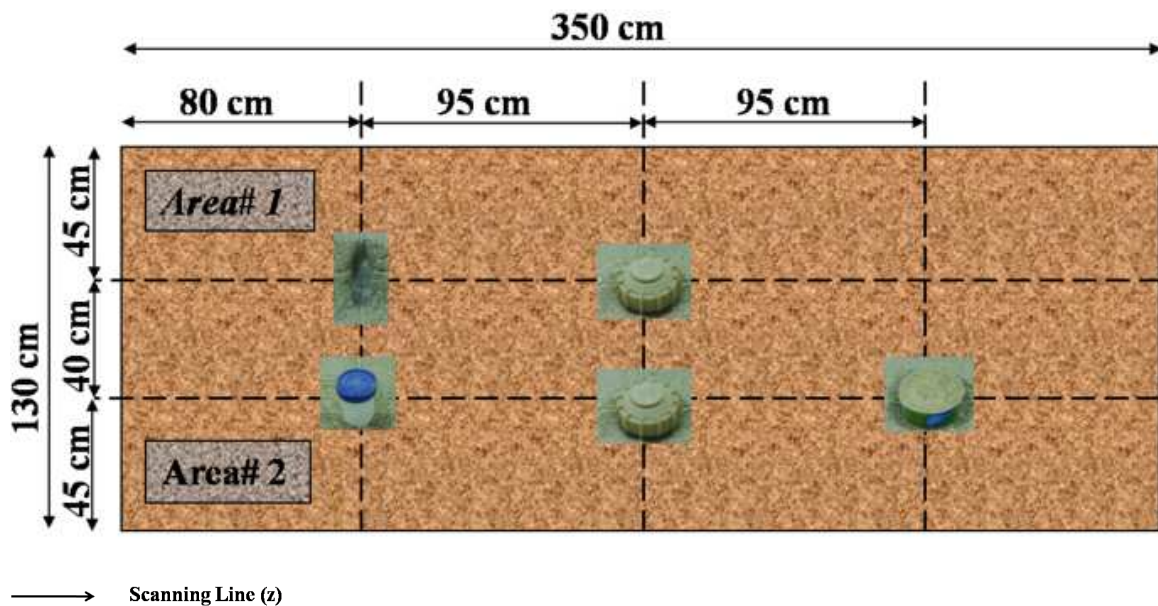


Figure 2.15. Scheme showing where the objects were buried: from left to right and from top to bottom, the hammer head, the mine at 5 cm, the empty container, the mine at 1 cm, and the bees wax.

To assess the GPR measurements capability to detect and distinguish different objects, two dummy mines, the metallic head of a hammer, a cylindrical container filled by bees wax and another empty one, have been chosen. The field scattered from all of them was both calculated and measured in the laboratory. The results have been compared and analyzed by cross-correlation.

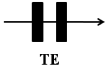


2.3.2.Experimental Setup

Before scanning the sandbox with the GPR, the following five objects were buried below the air-sand interface, as in the scheme shown in figure 2.15:

- a 11 cm long hammer head, at 2 cm below the surface;
- a dummy 8 cm diameter and 5 cm high TS-50 mine (figure 2.16), at 5 cm below the surface;
- an empty 6 cm wide and 7 cm high cylindrical plastic container, at 1 cm below the surface;
- another dummy TS-50 mine, at 1 cm below the surface;
- a 12 cm wide and 5 cm high cylindrical container of bees wax, at 1 cm below the surface.

After having buried the objects in the sand, the scanning process took place: the bistatic GPR system equipped with 1 GHz antennas (PulseEkko Pro – Sensors and Software, figure 2.17) was dragged on the surface in the z direction, gathering the results with a step size of 1 cm. In this section, the scans along line #1, right below Area #1, and along line #2, above Area #2, have been taken in consideration. Scans were repeated each time the polarization of one of the antennas (figure 2.17) was changed. Table I shows how B-Scans have been classified with respect to the transmitting and receiving antennas polarizations.

Table I: B-scans polarizations

		Transmitting antenna	
		x	z
Receiving antenna	x	 TE	 CROSS
	z	-	 TM

When scanning on the sand along the z direction, the distance traveled by the GPR system was recorded using an odometer as shown on the left of figure 2.14.



Figure 2.16. The dummy TS-50 plastic mine, manufactured by Cking Associates LTD.

2.3.3. Numerical Simulations

All the numerical simulations were carried out using the GprMax implementation [58] of the FDTD method[59]. Five $(20 \times 20 \times 50)$ cm³ volumes, extracted from the experimental setup (figure 2.15), were simulated to collect the field back-scattered by

the five items. Each volume, homogeneously discretized using a 2.5 mm resolution to obtain the computational domain, was surrounded by Berenger's Perfectly Matching Layer[60] and simulated twice, with and without the buried object.

The (apparent) relative dielectric permittivity of the sand, was measured using the Time Domain Reflectometry technique (TDR), [61, 62]. The data were acquired with a Tektronix 1502C cable tester equipped with an RS232 interface and connected to a coaxial probe consisting of three stainless-steel rods, having a diameter of 0.4 cm, a distance of 4.5 cm between each couple of rods, and a length of 20 cm. Measurements were taken in different positions of the sand box and an average of 3.5 ± 0.1 was estimated for the dielectric permittivity of the sand [63].

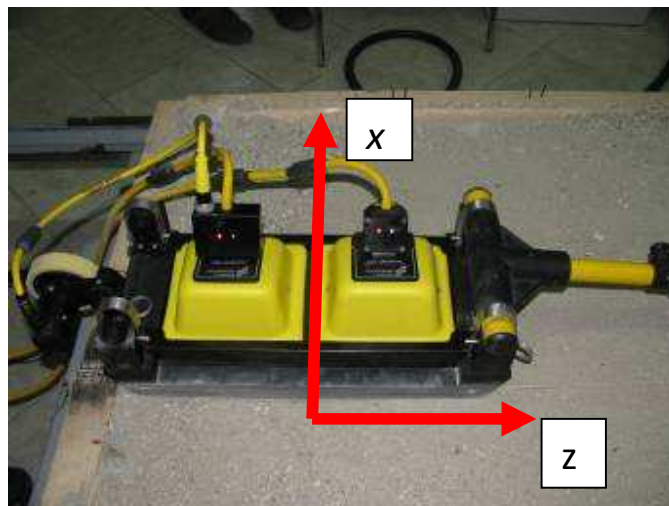


Figure 2.17. The Radar PulseEKKO PRO, the GPR system employed for the experiments. The transmitting and receiving antennas can be oriented either along the x or the z axis: it is possible to obtain measurements for all 4 combinations of polarizations (table I).

To simulate the GPR system with the FDTD method, the field source (transmitter) was synthesized as a dipole, polarized either along the x or the z axis, and the exciting pulse was shaped to cover all the frequency range from 500 MHz to 1.5 GHz. In addition, all the electromagnetic field components were gathered 15 cm

apart from the source (receiver), in the z direction. Multiple simulations were run to obtain B-Scans: both the transmitter and the receiver antennas were moved together along the z axis, at 1 cm step, over the objects.

2.3.4.Results

For all the results described in this section, the numerical B-Scans were obtained sampling the induced current on a dipole that would be placed as if it were the receiver antenna in the experimental setup. The B-Scans from the GPR system were obtained from the raw readings of the instrument. In addition, all B-Scans have been limited to 6.5 ns, twice the time needed by an electromagnetic wave to travel to the bottom of the sand box: at more than 7 ns, a strong echo, caused by the iron in the basement concrete, was recorded.

After simulations and measurements, a good agreement is noticed in the B-Scans. In figure 2.18, at about 80 cm, both methodologies correctly detect the hammer head and, at about 2 m, the fake mine, 5 cm deep. The concavities of hyperbola are similar, too.

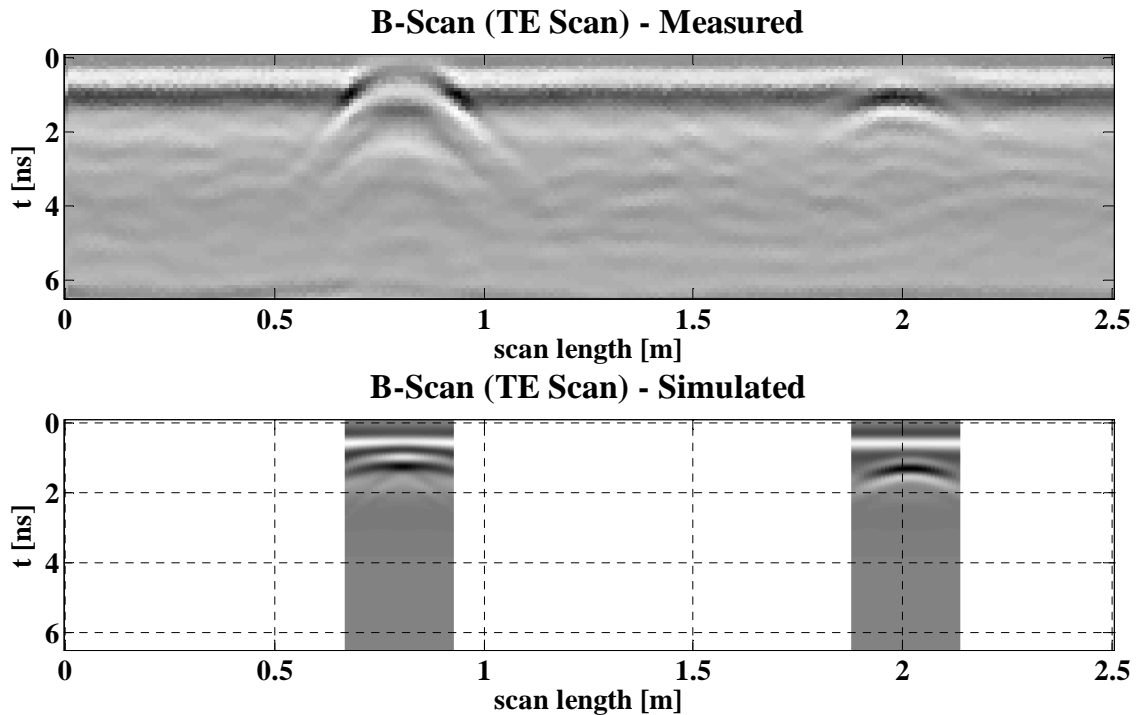


Figure 2.18. TE B-Scans, obtained from scanning line #1, setting both transmitter and receiver polarizations along the x axis. The small volumes that were simulated, are aligned to the corresponding real ones.

As it can be seen in figure 2.18, at the z coordinate where the hammer head was buried, the radar response is very strong and a ringing effect, due to the coupling between the metallic object and the GPR antennas, is clearly visible. Such a feature is not detectable in the simulation, were the signal due to the hammer head is less noisy.

Moving to line #2, a good agreement between simulated and measured results is noticed (figure 2.19). In addition, comparing figures 2.18 and 2.19 at 2 m along the z direction, the radar section shows that the hyperbola is lower because of the deeper location of the mine.

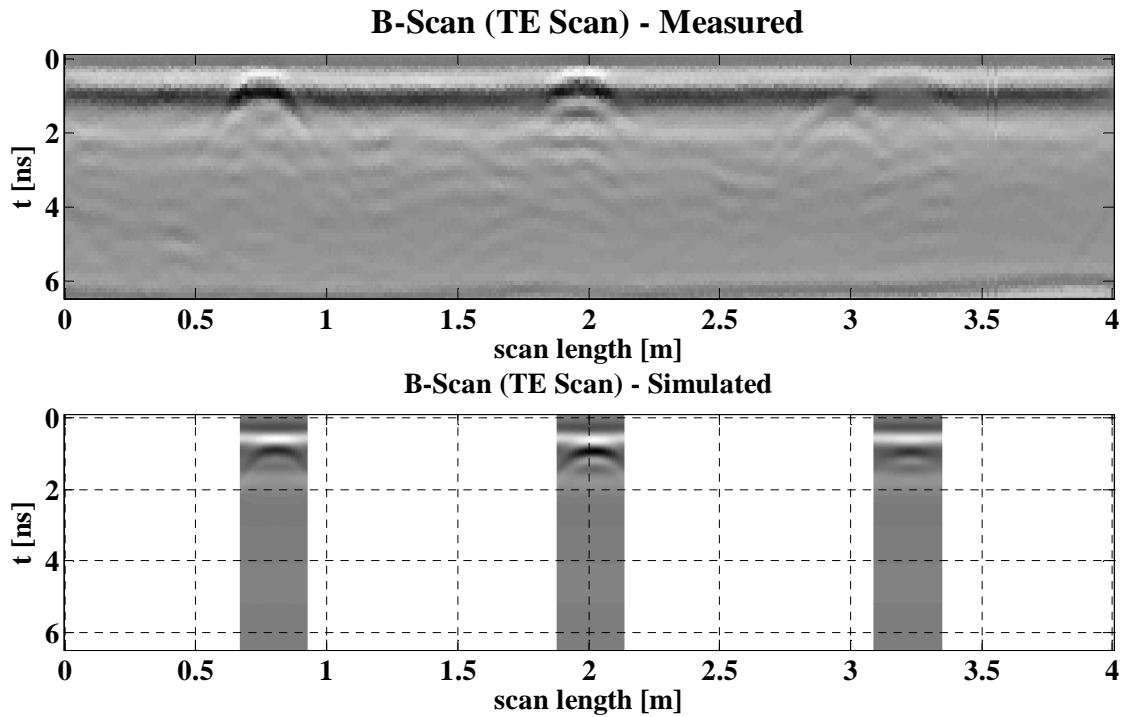


Figure 2.19. TE B-Scans, obtained from scanning line #2, setting both transmitter and receiver polarizations along the x axis.

The back scattered signal recorded for the bees wax is characterized by two close hyperbolas, which may be due to the corners of the box containing the wax. In particular, the second hyperbola located at about 3.2 m in the z direction, shows better when scanning the soil in cross polarization (figure 2.20): probably such a result is caused by some signal polarization effect.

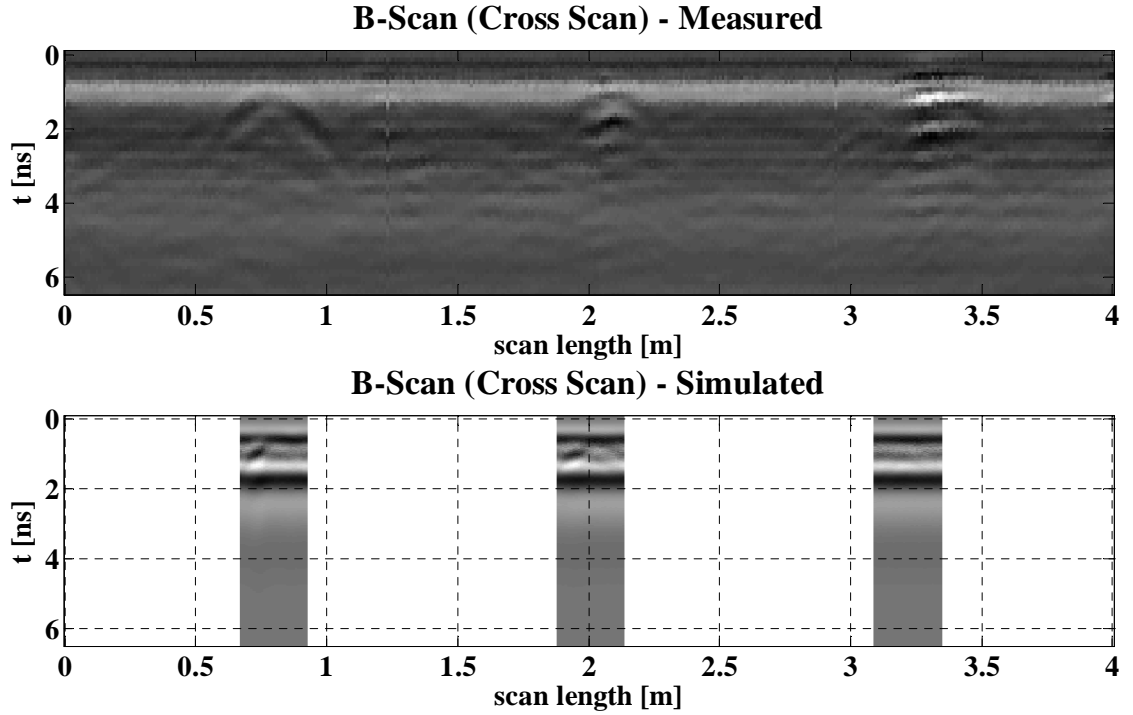


Figure 2.20. Cross B-Scans, obtained from scanning line #2, setting the transmitter polarization along the z axis and the receiver one along the x axis.

The comparison between the different measurements (figure 2.15 and figures from 2.18 to 2.20), points out the problems we had with the buried objects location. In fact, during the acquisition, the antennas had moved the first layer of sand, changing both the vertical and horizontal position of the targets. Moreover, the dry loose sand may have affected the proper functioning of the odometer, introducing a further uncertainty in the horizontal position of the targets. Nevertheless, the B-Scans can still be used for buried object detection.

In this work, the TM scans were also measured and simulated: however, the results have not given additional information (figure 2. 21) with respect to TE scans.

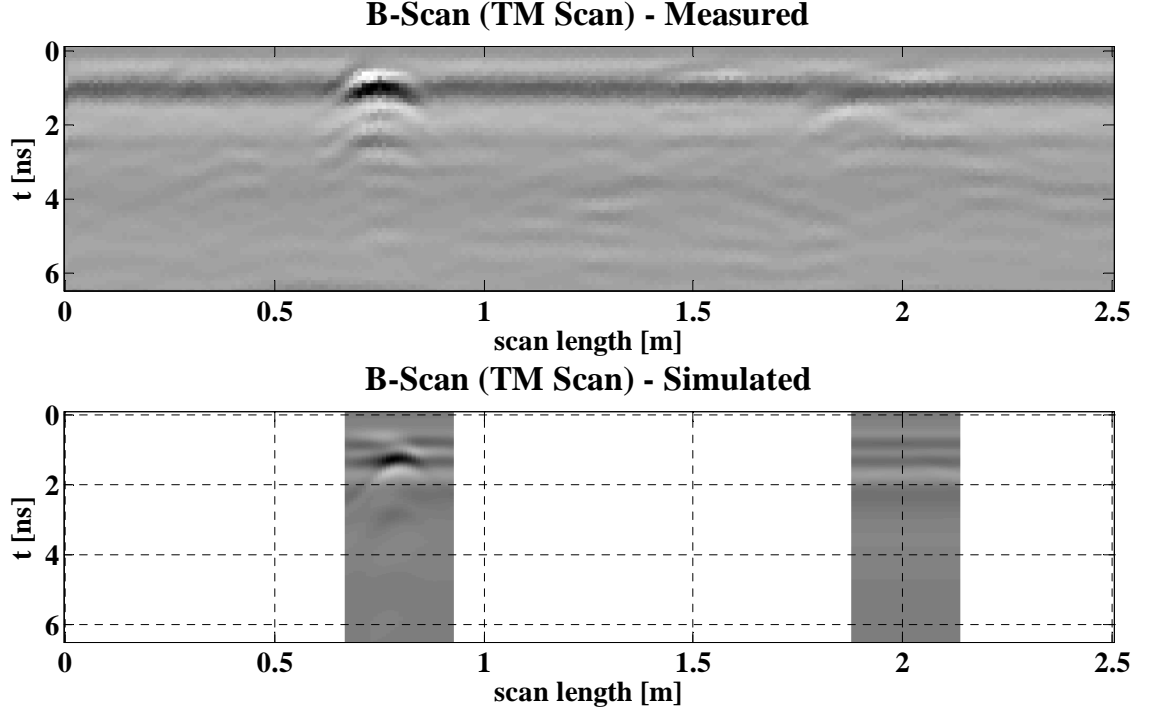


Figure 2.21. TM B-Scans, obtained from scanning line #1, setting both transmitter and receiver polarizations along the z axis.

To measure the degree of similarity between two B-Scans, the cross-correlation operation has been used [64,65]. Each B-Scan may be represented by a matrix, for example S , whose element is $S[i,j]=S(i\Delta t,j\Delta z)$, where Δt ($=0.1$ ns) and Δz ($=1$ cm) are respectively the sampling time and the sampling space intervals (e.g.: a B-Scan over 50 cm for 6.5 ns is discretized on a 65×50 matrix). Considering two different B-Scans, S_1 , $M \times N$, and S_2 , $H \times K$, the cross-correlation matrix may be calculated as follows:

$$r[h,k] = \sum_{m=1}^M \sum_{n=1}^N S_1[m,n] S_2^*[h+m-1,k+n-1] \quad (2.1)$$

$$\forall h \in \{(2-M) \dots H\} \quad \text{and} \quad \forall k \in \{(2-N) \dots K\}$$

where the elements outside the matrices are considered zeroes and both S_1 and S_2 are normalized to their respective standard deviations, being the standard deviation of each matrix calculated from all its elements. Analyzing (2.1), the size of the matrix r is $(M+H-1) \times (N+K-1)$.

The maximum of the cross-correlation gives a measure of how two patterns, represented by S_1 and S_2 , are similar, without taking into account their relative positions:

$$R = \max\{r[h, k]\} \quad (2.2)$$

If S_1 and S_2 are the B-Scans obtained when the field scattered by the soil alone is subtracted from the one of the soil with the buried object, (2.2) may be used to discriminate the type of buried object from simulated results. Before applying (2.1) to the calculated and measured B-Scans, an estimation of how the R parameter is sensitive, when changing the sand relative dielectric permittivity, is needed.

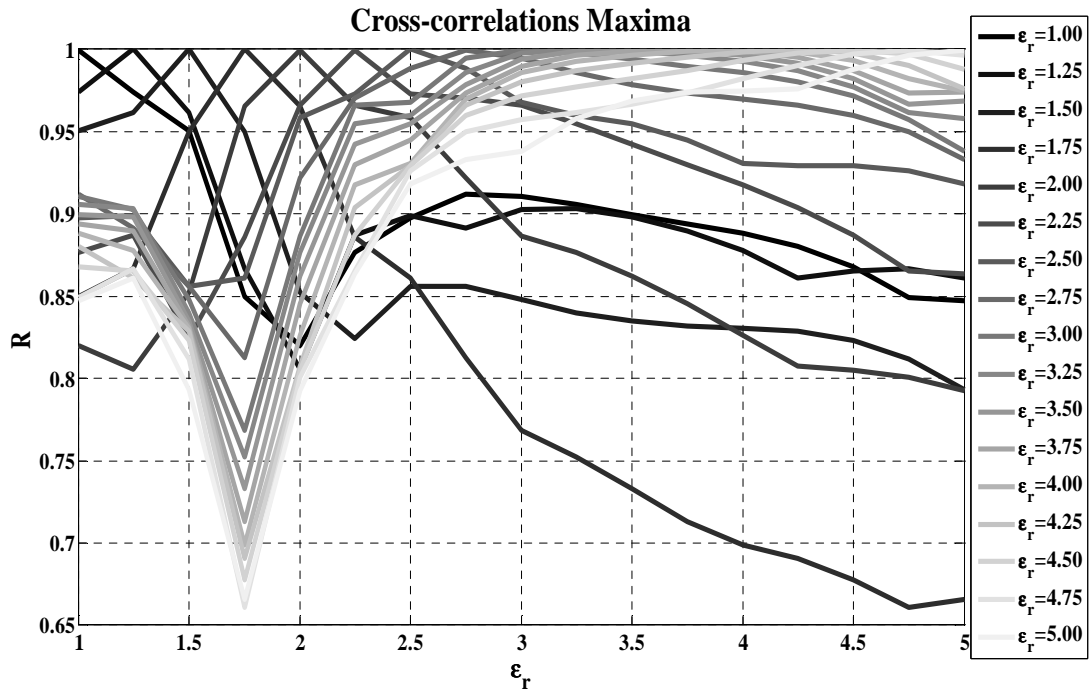


Figure 2.22. As relative permittivity increases, it becomes difficult to decide the sand dielectric relative constant by inter-correlating B-Scans.

Considering the dummy TS-50 at 5 cm below the surface, a first simulation in which the sand relative dielectric constant was fixed, was run, obtaining S_1 . After that, changing the relative permittivity from 1 (vacuum) to 5, at 0.25 steps, a full series of simulations was executed, obtaining several B-Scans and the corresponding $S_2=S_2(\epsilon_r)$. Finally, (2.1) and (2.2) were applied to S_1 and each S_2 , obtaining all the maxima values for cross-correlation. For instance, when S_1 was calculated letting the dielectric permittivity of sand be 1, the line in figure 2.22, whose maximum is located at $\epsilon_r=1$, was generated. If the above operation were repeated for each type of sand, all the lines in figure 2.22 would be obtained.

Clearly, the maximum of cross-correlation is obtained when both S_1 and S_2 are calculated using sands with the same electric density. It is interesting to notice however, that, when increasing the sand relative dielectric permittivity, lines show a wider plateau: the patterns extracted from B-Scans become similar for electrically denser sands. This behavior is probably due to the electrical properties of the explosive partially filling the dummy mine. The sinking of lines for $\epsilon_r=1.75$ may be caused by the composition of the fake TS-50 mine: its average relative dielectric permittivity is, in fact, close to 1.8, as it can be calculated from the model of the mine used in the FDTD simulations.

Restoring the measured values for sand primary constants and considering S_1 and S_2 associated to the simulations of each buried object, all the possible combinations of cross-correlations maxima have been calculated (Table II).

Table II: Cross – correlations maxima (R) among simulated B-scans

		S_1 Simulated				
		<i>Hammer Head</i>	<i>TS-50 at 5cm</i>	<i>Empty Container</i>	<i>TS-50 at 1 cm</i>	<i>Bees wax</i>
S_2 Simulated	<i>Hammer Head</i>	1.000	0.977	0.901	0.867	0.692
	<i>TS-50 at 5 cm</i>	0.977	1.000	0.956	0.917	0.734
	<i>Empty Container</i>	0.901	0.956	1.000	0.847	0.849
	<i>TS-50 at 1 cm</i>	0.867	0.917	0.847	1.000	0.686
	<i>Bees wax</i>	0.692	0.734	0.849	0.686	1.000

When S_1 and S_2 are associated to the same buried object, R reaches its maximum possible value, 1. In addition, because both scattered fields had been simulated, table II is diagonal. The differences among R are sometimes less than 0.1 (10%): discerning between couples of items is an operation that may result difficult in an experimental environment. Such statement is proven when substituting measured values to S_2 (table III): occasionally, objects identification by cross-correlation mistakes (e.g. row 4, bees wax has been recognized as if it were a dummy TS-50).

Table III: Cross – correlations maxima (R) among measured and simulated B-scans

		S_1 Simulated				
		<i>Hammer Head</i>	<i>TS-50 at 5cm</i>	<i>Empty Container</i>	<i>TS-50 at 1 cm</i>	<i>Bees wax</i>
S_2 Measured	<i>Hammer Head</i>	0.425	0.384	0.248	0.344	0.244
	<i>TS-50 at 5 cm</i>	0.448	0.458	0.289	0.412	0.280
	<i>Empty Container</i>	0.477	0.504	0.302	0.457	0.292
	<i>TS-50 at 1 cm</i>	0.481	0.528	0.322	0.508	0.386
	<i>Bees wax</i>	0.490	0.524	0.246	0.404	0.291

Looking at the experimental and numerical results, the sandbox of HDL has been confirmed a valid setup to assess GPR performances. A good agreement has been found between FDTD simulations and measures, and the GPR technique has confirmed its capability to detect buried metallic and non-metallic objects: when compared to other systems, such as the metal detector, GPR scans lead to fewer false alarms and, thus, to cheaper demining.

Even if both the numerical and the experimental results have shown GPR detection accuracy, they have also demonstrated that, deciding the type of buried object by looking at B-Scans similarities by inter-correlation, sometimes leads to errors. To make the recognition process more accurate, different algorithms or multi-sensor techniques should be taken in consideration.

Chapter 3: Evaluation of clay content in substrate and road foundation with GPR

3.1. Introduction

The evaluation of clay content in soils is important for many applications in civil engineering as well as in environmental engineering, agriculture and geology. This study is applied to pavement engineering, but proposes a new approach, method and algorithm that can be used also for other purposes. Clay in sub-base or sub-grade reduces bearing capacity of structural layers of pavement. This induces frequently damages and defects that have a severe negative impact on road operability and safety. Traditionally, the presence of clay in a soil is evaluated in compulsive water content.

In this study we propose a new technique based on Ground Penetrating Radar (GPR) inspection. GPR is yet largely used for pavement engineering applications and this technique could be easily integrated in the existing systems, making the inspection more effective. This method is based on the Rayleigh scattering according to the Fresnel theory. Basically the GPR signal, differently as usual, is processed in the frequency domain. The method has been compared with others to evaluate as it performs.

Ground-coupled Radar antennas were used for GPR analysis. GPR operates with two antennas with central frequencies about 600 MHz and 1600 MHz. Measurements are developed using 4 channels, 2 mono-static and 2 bi-static. The received signal is sampled in the time domain at $dt = 7.8125 \times 10^{-2}$ ns. The

experiments have been carried out in laboratory using typical road material adequately compacted in an electrically and hydraulically isolated box. Clay (montmorillonite) has been gradually added from 2% to 30%. GPR inspections have been carried out for any clay content. The GPR signals have been post-processed both in the time and in the frequency domain.

In the time domain, a real consistency of the results was assessed with those expected to arise from the electromagnetic theory, considering the different signals in terms of time delays between pulses reflections, dielectric constant and amplitude. In the second step, the analysis was carried out in the frequency domain, assuming residual water content of dry clay, by virtue of its strong hygroscopic capacity. As expected, the scattering produces a non-linear frequency modulation of the electromagnetic signal, where the modulation is a function of water content, therefore, indirectly, of the percentage of clay present in the soil material. The frequency spectra have shown a significant negative correlation between the shift of the value of the peak and the clay content in the road material: indeed the results show a decreasing trend in the value of the peak frequency, with a shift equal to the FFT resolution (0.26×10^8 Hz), while the clay content varies from 0 to 30%; further feedback has provided from comparative analysis of spectra, it is possible to evaluate the selective behavior of the clay, compared to specific frequency range. The main benefit of the method is that no preventive calibration process is necessary.

3.2. Materials and Methods

The laboratory of Road belongs to the Sciences of Civil Engineering Department of the University of Roma Tre. The experience in laboratory required the use of a range of instrumentations, listed below:

1. Acquisition unit RIS who is the main instrumentation consisting of a Radar data acquisition and control PC, a block antennas (two dipole antennas at 600 MHz and 1.6 GHz nominal frequency with four channels, two bistatic which transmits at 600MHz and receives the 1600 MHz or vice versa, and two monostatic which transmits and receives at the same antenna) and a wheel metric (encoder resolution of 2.4 cm).

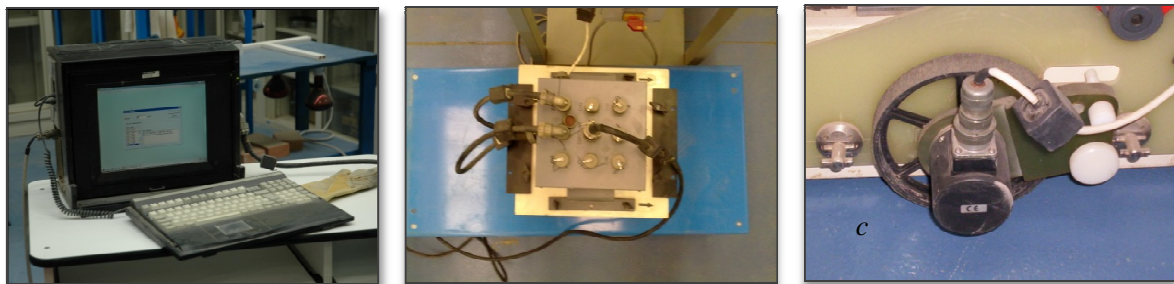


Figure 3.1. Type of GPR used in the laboratory. a) PC Radar for control and acquisition, b) Block antennae and c) Metric wheel

Others equipment was the electronic balance, the formwork and the vibrating table.

3.2.1. Acquisition of the starting material: the mixed of Magliana

To carry out the tests in order to reproduce in the most likely form of road problems, the typical configuration of materials forming the layers of background road foundation and foundation, it was decided to use the mixed of Magliana soil type (0 / 5 mm). The clay used for the laboratory investigations is clay montmorillonitica characterized through a granulometric analysis by wet.

Regarding granulometric characteristics of the clay material used in the experiment, it was considered reasonable to carry out a screening on the same 0.250 mm sieve. In order to make the results of the experiment significant and relevant to

the actual shape of the load-bearing layers of pavement, the field survey through which we proceeded to evaluate the influence of the clay material is selected according to the values provided by standard-CNR UNI 10006 in "Construction and maintenance of roads - Techniques of use of land" for the classification of land for construction of the layers of road structure.

In reference to the fraction passing the 0.075 mm sieve, it was decided to consider a field of investigation for the content of clay in the formwork varying percentages from 0 to 30%.

3.2.2. Mixing Protocol

The considerable extent of the field investigation of the clay material (0-30%) led to question what could be the minimum range of reference such that a mixing process registered in time would provide a satisfactory response in terms of homogeneity of the mixture established. In particular, the issues were attached to two types:

1. looking for a small size material that could somehow get closer to the size of the material clay pollutant;
2. isolation of the same material to see the end of the process of mixing the correspondences with the known value by weight of pollutant introduced upstream of the process.

3.2.3. The density of reference: protocol compaction

Mixtures within the formwork must comply with the normal implementation of the constituent material of the bearing layers of pavement. In this sense it is necessary to provide greater thickening of the material under investigation an operation of compaction. Given the dry conditions of execution of the test campaign, the

immediately indicator who can be referred to the state of densification of the soil on the formwork, after a process of compaction, is found to be the density of the dry sample, who is the ratio between the dry mass of soil and its volume. After defined this indicator, the objective was to see an appropriate response in the same value for the same land, but determined according to standard procedures.

3.2.4. Basic parameters of mixtures: particle size and limits

The various test mixtures were characterized by particle size analysis, at the end of the mixing procedures, and vibration detection signal on formwork, was carried out for each mixture from 0 to 30%, the sample of 700 g of material (4% about average on the total weight of the soil vibrated) in order to optimize the timing of the surveys, the particle sizes were made from the highest percentage of clay and continue around the lower rates until no longer possible to calculate the limits of consistency[66].

The limits of consistency are the moisture of a land conventionally assumed to characterize the transition from liquid to plastic state; the plastic state to semi- solid state and the semi-solid state to solid state. For the purposes of this discussion were analyzed two limits (on mixtures with clayey material between 18 and 30%): the limit of the liquid state, and the plastic.

3.3. Results and Discussion

The analysis of data obtained by GPR IDS, usually in binary format are not readable by a simple spreadsheet like Excel. For the creation of the model, calculation was made in the Matlab environment characterized by a high-performance language for technical computing.

The code makes use of electromagnetic theory and refraction for the extraction of the signal in time domain. To analyze signals in the frequency domain, we used the fast Fourier transform. This allowed the extraction of data matrix on which the various calculations were performed on a spreadsheet.

3.3.1. Analysis in Time Domain

3.3.1.1. The field under investigation

The investigation in the time domain was made in the prospective of seeing how the impact of the clay content in any soil type is. In particular, by reference to the percentage of the clay content, we studied the following parameter:

- Time delays between the peaks of reflection signal;
- The apparent dielectric constant of the material under investigation and
- The signal amplitude.

3.3.1.2. Time delay between the peaks of reflection

The objective of the first survey in the time domain was to analyze the trends of the time delays between the main peaks, considering the fact that the signal in time is subject to phenomena of attenuation, the considerations are related only to the first 4 peaks samples. The delay was calculated according to the reference $dt = 7.8125 \times 10^{-2}$ nanoseconds who is the sampling time of the received signal in time domain.

The comparisons made were of two types:

1. delay between the counter parts peaks related to different configurations mixed soil and clay;

2. delay between the different peaks of the same signal on each of the mixtures created in the qualifying campaign in the laboratory.

The performing of calculation of the delay between two consecutive peaks is to identify the two step sampling values corresponding to the peak amplitude: the distance between them, measured in number of samples on the abscissa was multiplied by the value reference time, thus obtained the desired delay.

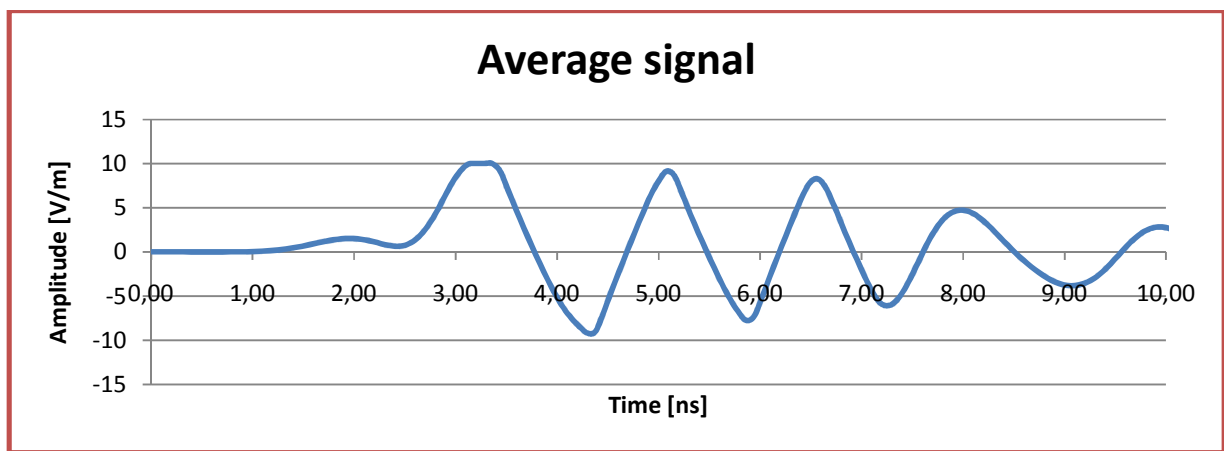


Figure 3.2. The time delays measured for the first four peaks of reflection

The interpretation of the data extracted with the Matlab code, highlighted a problem of signal saturation of the first peak due to two reasons. We know that the digital signal is defined by a series of discrete points, and not continuously, and the resolution of that data is just the time of sampling. If the fluctuation amplitude is so small as to be determined with respect to time under the same sampling, which happens in the middle of the time window, is not seen nothing, and returns the same value of peak amplitude, until the extent of variation of this is not new interpreted by sampling resolution of the radar.

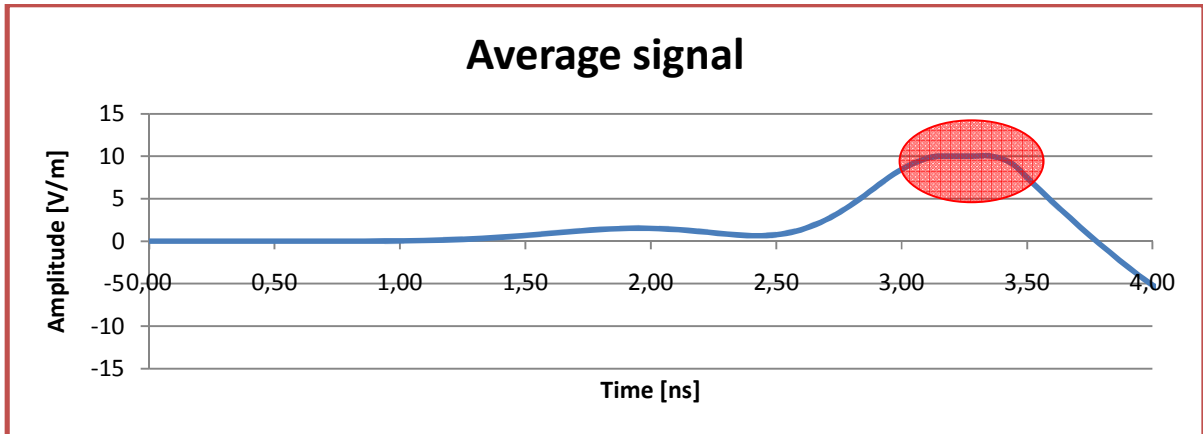


Figure 3.3. The saturation of the signal on the first peak of reflection

The solution was to report back to the first peak, the time abscissa of the central value among the saturation and, if they are equal in number, the reference on the abscissa axis is the average of the corresponding samples.

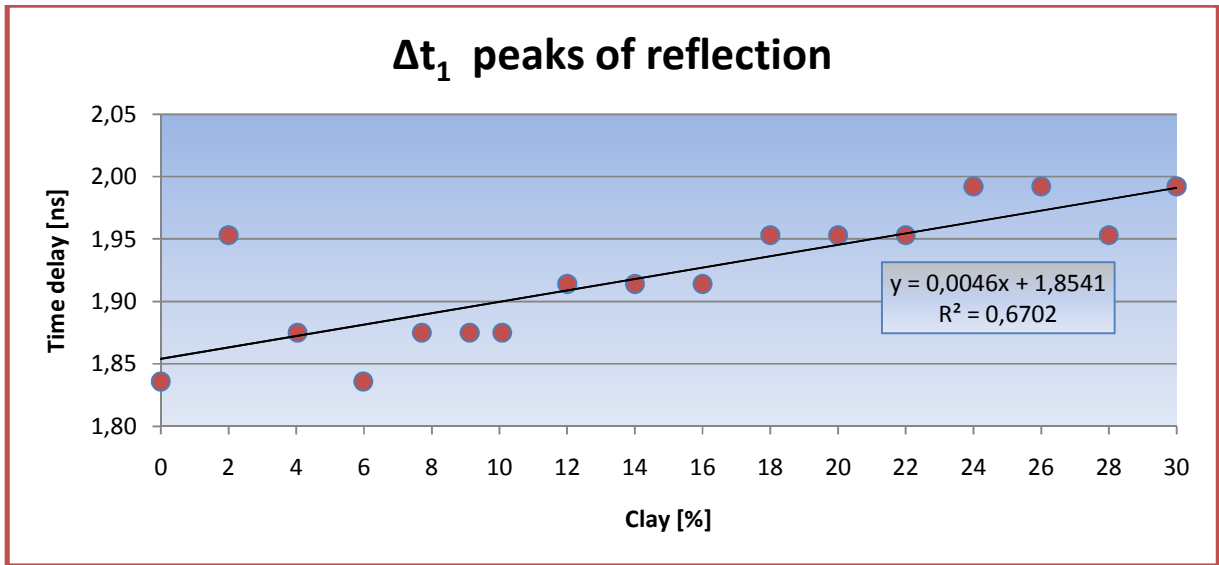


Figure 3.4. Trend of the time delay between the first and the second peak amplitude

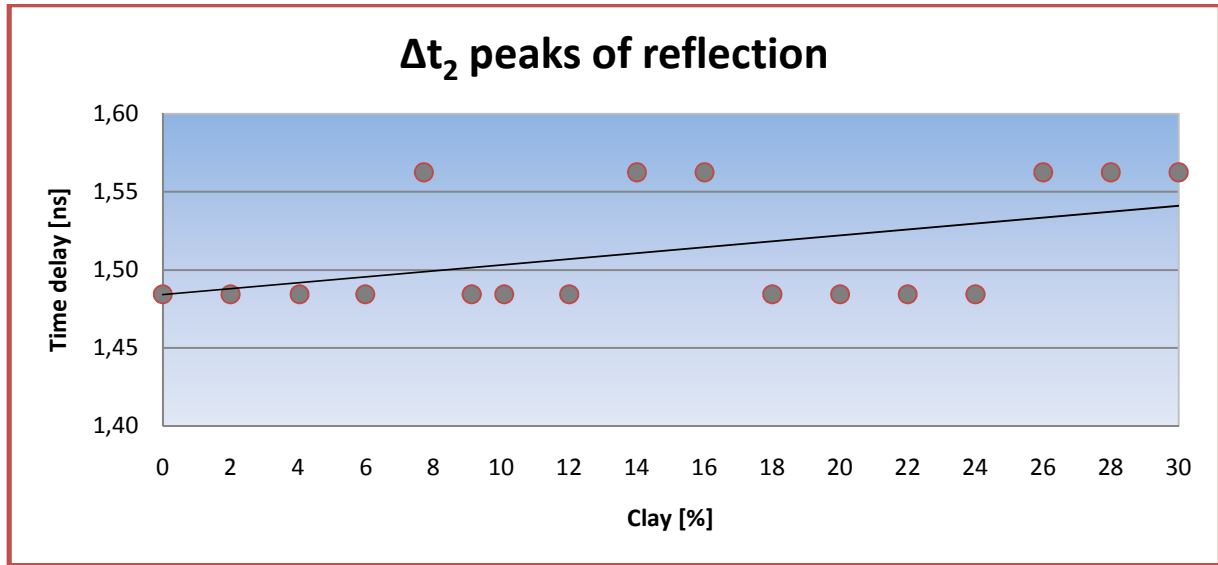


Figure 3.5. Trend of the time delay between the second and the third peak amplitude

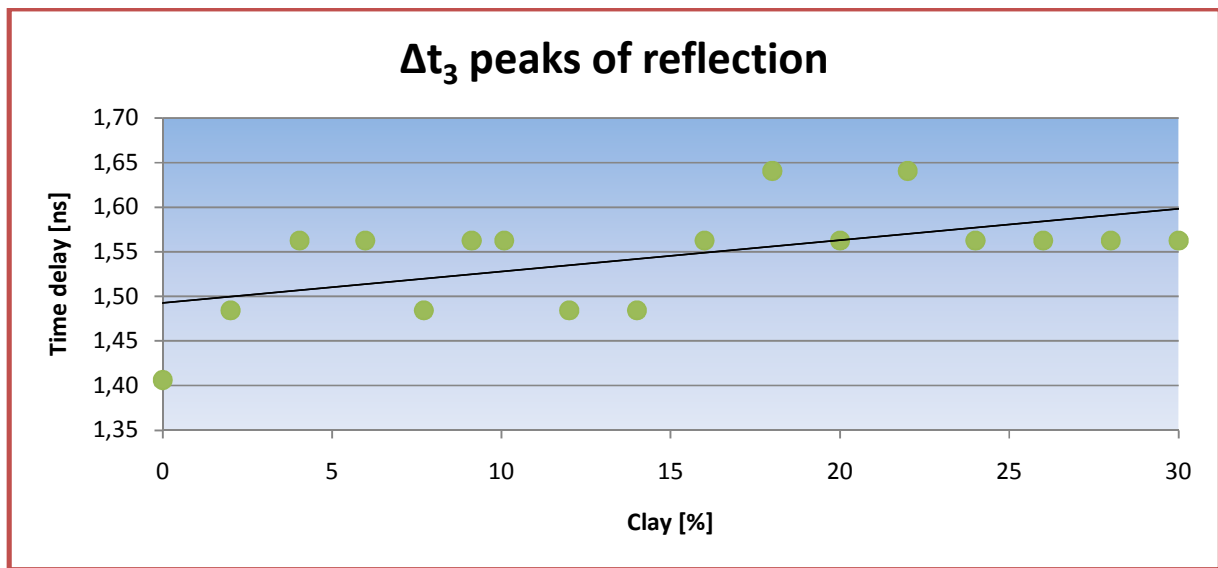


Figure 3.6. Trend of the delay between the third and fourth peak amplitude

The figure above (3.4, 3.5, 3.6) shows how the intervals between peaks for the same signal are not constant, as it would have to expect, because the system is controlled, evidently this feature seems to be related to a problem of signal attenuation.

Regarding the trend of the reflections delay with the increase in the percentage of clay material, it is noted that there is an increase of the same dielectric constant, consistent with what was expected. The increased presence of clay causes an increase in the state of densification of the material, decreasing the contribution of the voids between the suspect and increasing of the solid, dielectric constant greater air does not change the size of the actual dielectric constant to higher values. This results in a decrease in wave velocity in the middle, and a reflection of the signal to higher degrees of densification of the material, with increasing delays.

From the figure, it is evident that the delay is the most significant on the first and second peak of reflection, for which it is taken as a reference linear correlation with a good value of R^2 ; other temporal variations have minor response but basically, although low correlation, also indicate an increase of the phenomenon.

3.3.1.2. The trend of the effective dielectric constant

The compaction of layers road pavement, has the effect of reducing the gaps in the material, and consequently to increase the density. This reduction depends on two main factors:

- grains fit assuming a more compact configuration space;
- Some grains are broken, and the smaller parts produced by this process go to fill in some gaps.

If the material is wet, the behavior is complicated because the water first lubricates the contact between grains, and secondly, it fills the gaps in the incompressible fluid. In the first case, the water helps the compaction, prevents the increase in the density. As described in the objectives of this study, our analysis is directed to the case of material in dry conditions, as suggested by the performance of delays described above, the increase of the clay percentage in the sample will lead to a

decrease in speed of propagation of the signal in the medium, as the area of propagation of this is known and equal to the thickness of the formwork (10 cm). The report resulting from the electromagnetic theory $v = \frac{c}{\sqrt{\epsilon'/\epsilon_0}} = \frac{c}{\sqrt{\epsilon_r'}}$ and the

apparent dielectric constant can be found through inverse formula with the range of variation approximated equal to 2.5 units, and the points identified were interpolated from a linear regression; line with a good correlation coefficient, an index adequate sensitivity of the phenomenon with respect to the parameter in question.

In this regard, it is reasonable to assume that, further evidence developed in the future with the contribution of moisture, can be more aware in terms of dielectric constant: on the other hand this is likely due to the high difference of the dielectric constant of water ($\epsilon_r = 81$) than in the test materials ($\epsilon_r = 5$).

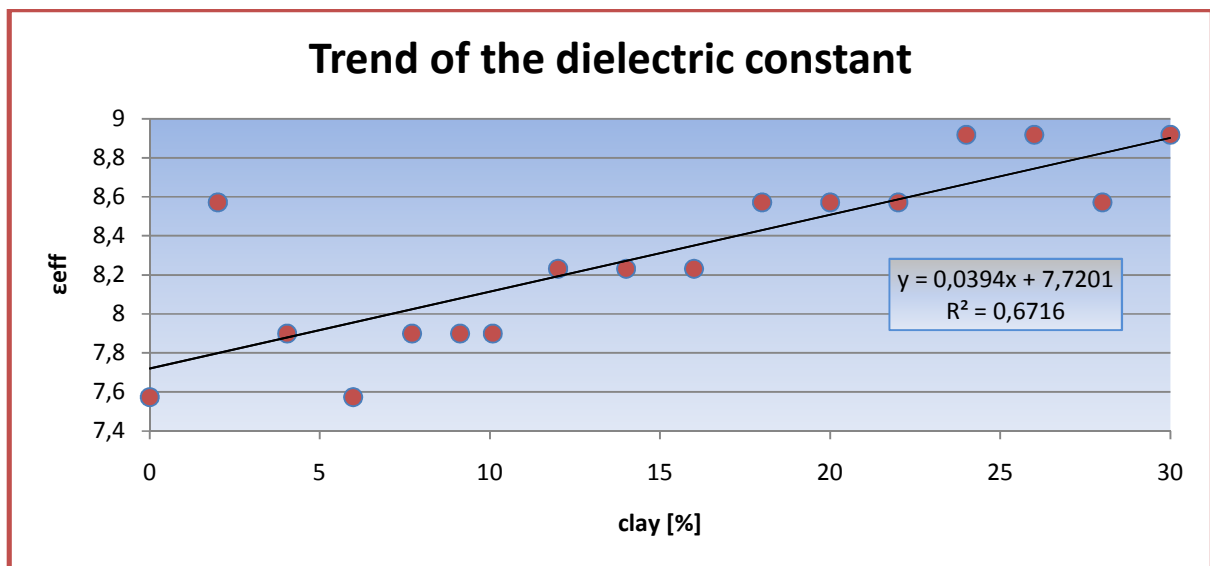


Figure 3.7. The trend of dielectric constant respect to clay variation

In this figure it is seen that respect to the increasing of the clay percentage, the apparent dielectric constant increase. That it was the expectation and fill well with the theory.

3.3.2 Analysis in the frequency domain

The principle under which analysis have been developed for assessment of the percentage of clay through the investigation in the frequency domain, is based on the hypothesis that; assuming the variation of clay content will result in a different absorption of the radar signal as a function of their frequencies. This, correspond to a modulation of the frequency spectrum of the received signal than that transmitted. In the frequency domain, radar signal is well represented by the frequency spectrum or the energy distribution of the signal at different frequencies.

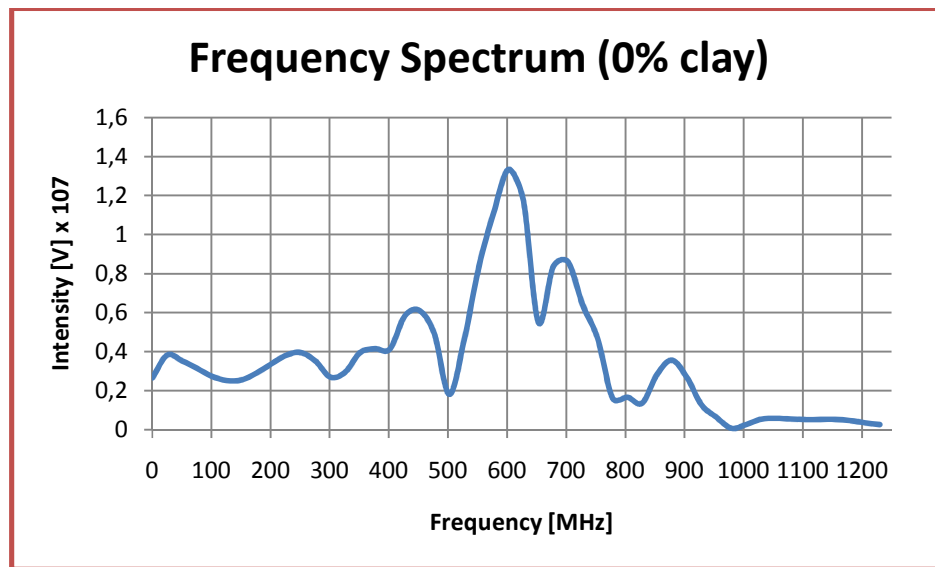


Figure 3.8 Example of frequency spectrum with clay at 0%

The GPR used in the laboratory corresponds to the model with IDS RIS2K centered at 600 MHz operating frequency, then the frequency spectrum transmitted

have a maximum energy density in correspondence of this value. The field of investigation for that domain took into account two fundamental characteristics by which it is possible to make a comparison between different spectra:

- The peak frequency;
- The trend of the spectrum.

For both aspects has been useful to conduct a comprehensive review in parallel with the results obtained in the time domain, to find any evidence to support what is already assumed.

Data processing has essentially tried to highlight what might be the major evidence found, in terms of comparative values of the peaks frequencies, intensity associated with them and the trend of the two variables; with the aim to define parameter sensitivity of the detectors who are compared to the clay content.

To get an overview of the trends of the spectra analyzed, the first stage of the analysis provides a comparative overview of all the spectra of the field tests from 0 to 30 percent clay.

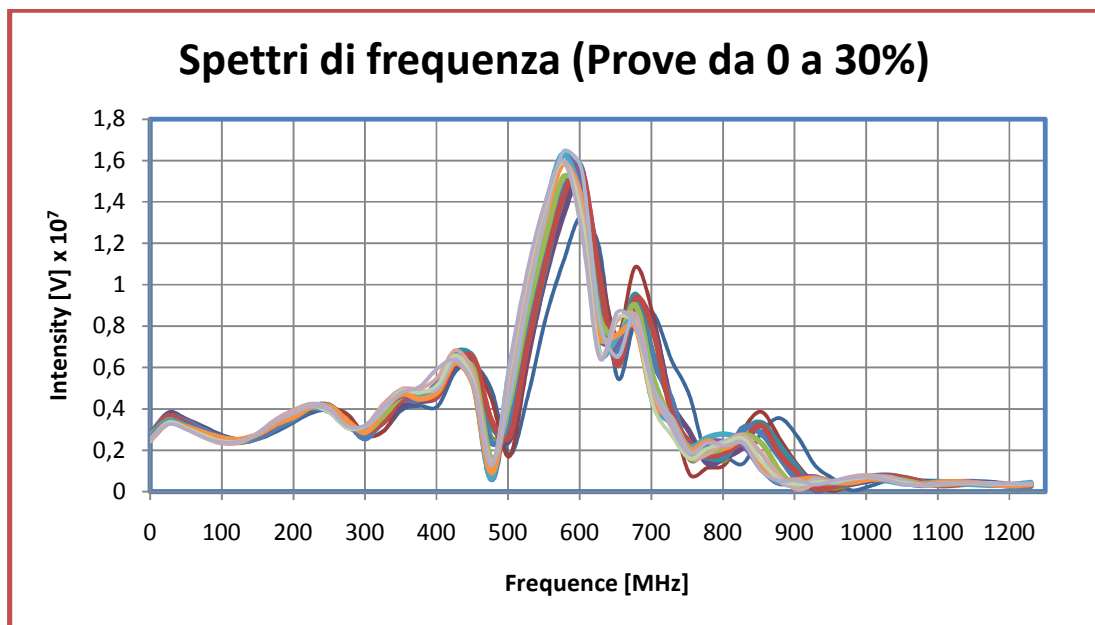


Figure 3.9. Frequency spectrum from 0 to 30% of clay

As easily deduced from the figure above, the peak frequency not undergoes significant changes and equal about around of the 600 MHz frequency of the GPR survey. Nevertheless, the next step was to check if the change of slight value of the frequency spectrum that takes maximum intensity, could provide useful information directly linked with increased percentage of clay into the formwork:

It can be seem that with increasing clay content, the trend of the peak frequency is decreasing: this trend is entirely the initial forecasts, but the magnitude of the values, together with the step distribution of points, clearly poses in front a problem of signal resolution in the frequency domain, similar to what happened in the time domain for the interpretation of reflection delay.

As demonstrated in studies conducted in the past, if in the mixtures soil we had analyzed the presence of water, the rate would move substantially (up to values in the range of 300 MHz), in this case however, clay is added in dry conditions with minimum water content, but still present. The spectrum then changes to lower values, with a small difference as to be determining under respect to the sampling resolution of the FFT. The $\Delta f = (6.03 \text{ to } 5.77) \times 10^8 \text{ Hz}$, corresponds exactly to the sampling of the FFT between these two threshold values of resolution cannot be seen anything, and the only result which can be reference is linked to the fact that the peak frequency has a decreasing trend with increasing clay.

In general, however, we can say that an increase in clay carries a greater quantity of water, though not high in absolute terms, this value is very low at the beginning, we can assume that the peak moves, but always under the resolution of the FFT, and when this becomes sensitive, then the peak frequency, moves to the lower value ($5.77 \times 10^8 \text{ Hz}$).

Future studies may be directed to try to resolve the FFT at a higher resolution, so as to generate more sample points and be helpful in this type of investigation in

which the instrument seems to be less resolute in the detection of the phenomenon, and therefore less sensitive to presence of clay.

3.2.5. The Trend of the spectrum

Further analysis was performed for comparison of spectra, with reference to the configuration of the mixed unchanged, from time to time compared with the spectra of the soil under investigation to the various percentages of clay. The intent of this investigation was to try to interpret, from an analysis of all the different spectra, the major findings noted in the changes in their forms. For the various percentages, we took three figures (3.10, 3.11 and 3.12) that can have meaningful comparisons. A minimum percentage of clay, medium and maximum are analyzed. The results demonstrate the verification of theory and feel well for what it was predicted.

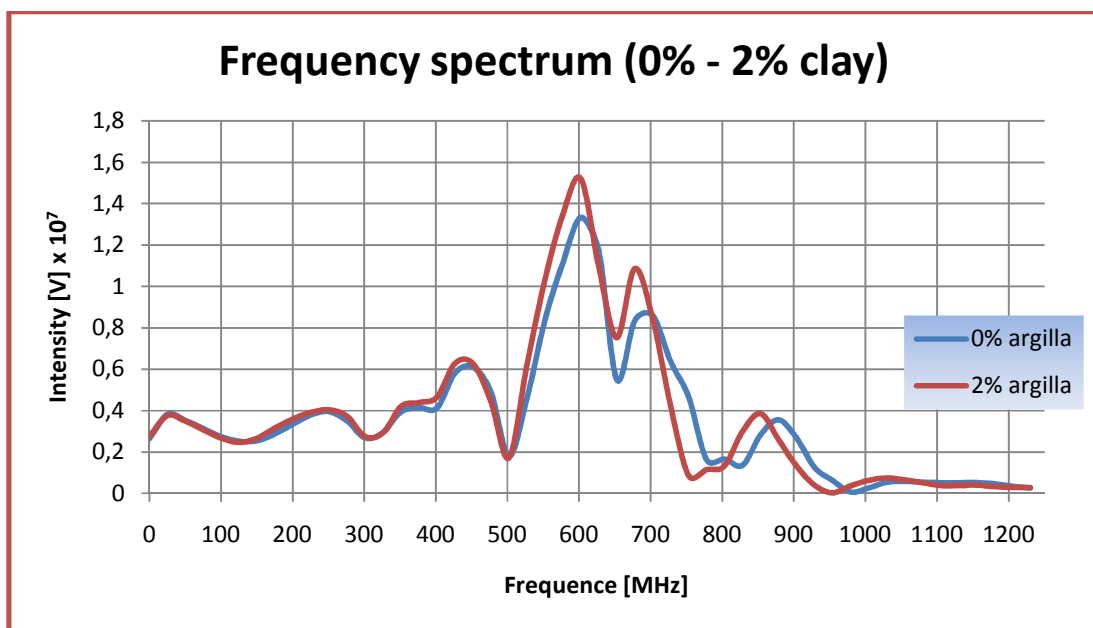


Figure 3.10. Comparison of frequency spectra (0%-2% argilla)

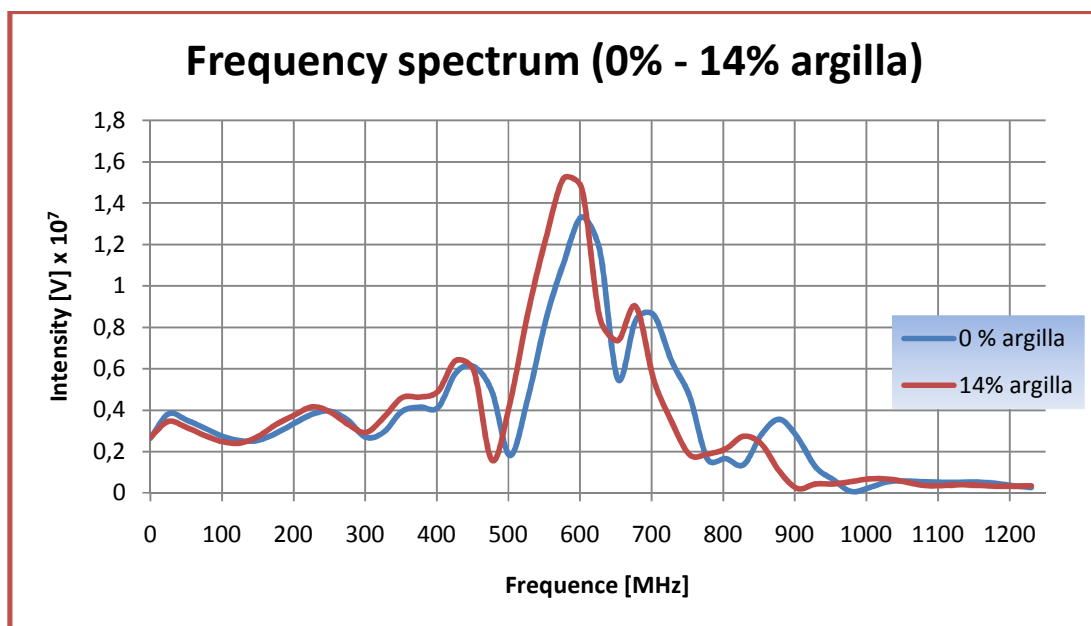


Figure 3.11 Comparison of frequency spectra (0%-14% argilla)

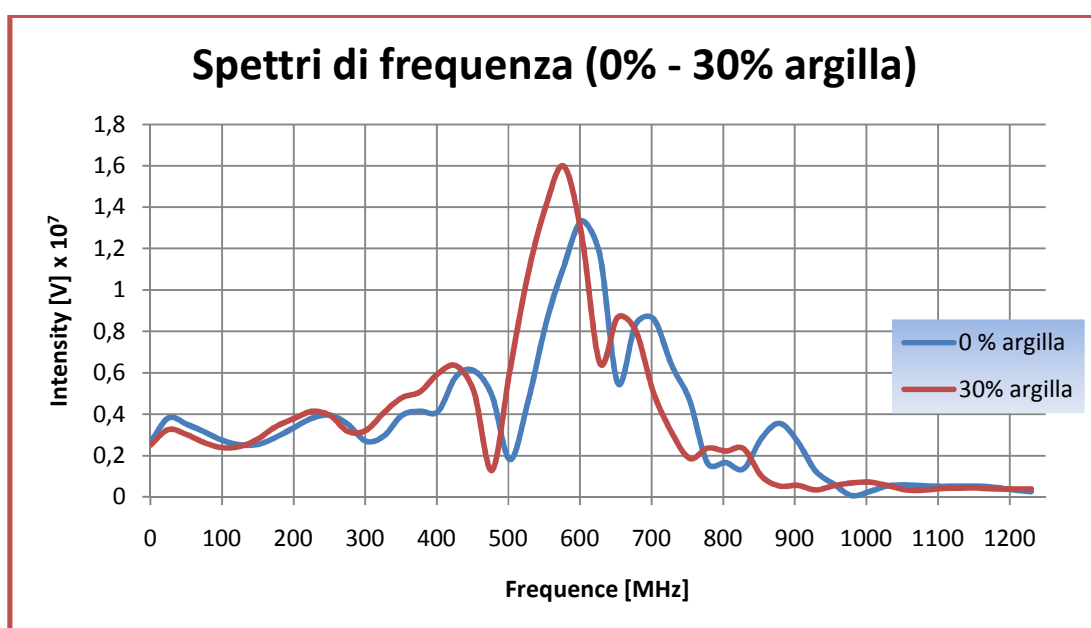


Figure 3.12. Comparison of frequency spectra (0%-30% clay)

Several considerations can be made on the observation of the figures above:

- it can be seen in the first harmonic signal, it does not change almost nothing in terms of both form and intensity;
- the more evidence, however, is related to the fact that the presence of clay, seems to attenuate the higher frequencies. In fact we have a secondary peak that, for higher percentages, goes to lower until it disappears completely. This fact probably is related to the phenomenon of attenuation of high frequencies;
- increased frequency of main peak (in terms of intensity). This trend could have two explanations:

1. be due to the calibration process carried out for the qualifying campaign, characterized by several phases of recalibration of the signal in reference to the trend of increasing values of the amplitudes with the percentage of clay in the time domain, thus also increasing the energy content of signal at 600 MHz;
2. for some physical phenomenon, the presence of clay could be selective with respect to frequencies, and then amplify the frequencies of 600 MHz, attenuates around of the 900 MHz. There is indeed a higher amplitude and a higher range, as if the clay would be to tighten the spectrum.

This last point may be a source of additional assumptions. The mechanism by which attenuation of the spectrum on the one hand, corresponds to the increase in the values of the same peak could be related to dispersed energy in addition to that is received, and then returns, loss less energy. Assuming, then, and the fact could be the subject of future investigations, that the energy losses are constant regardless of the clay content, the energy of the signal transmitted and received on a spectrum (eg. that at 0%), shall be equal to that characteristic of another spectrum. Of course, this reasoning remains in the field of hypotheses, as for most of the achievements of these are in fact empirical evidence for which it is difficult to provide a theoretical justification.

Chapter 4: Testing moisture with GPR for the stability of the road structure

4.1.Introduction

Measuring the water content of soils is important for applications such as flood defense, agriculture, determining the geomorphologic stability of slopes, construction, and finding the bearing capacity of structural foundations. Moreover, the variation of the water content in space cannot be neglected for most of these applications. In fact, it has been demonstrated that different spatial distributions of the moisture content produce different effects. Some examples include run-off generation for basins with spatially varying saturation zones[67], foundations of structures with variable moisture content[68] and non-homogeneous moisture distributions in the soil beneath road pavement[69].

It has been widely demonstrated that an increase in water content in the sub-asphalt layer can decrease the soil stiffness and cause pavement deflection. This deflection can damage the surface in different ways, depending on the temperature, the asphalt characteristics, the age, the repetitions and the loads weight. However, there is one problem which affects pavements universally: the infiltration of water through the pavement brings plastic material into the subgrade or the sub-base of the pavement. Furthermore, estimates of the water content in sub-asphalt soils are necessary to determine the performance of pavement drainage systems [70].

Only a few techniques have been used to monitor the water content in sub-asphalt soils in the past two decades. The sub-asphalt water content is often estimated via gravimetric sampling, time domain reflectometry, neutron probe logging and measuring the capacitance or resistance of devices. These methods are accurate, but they also have many disadvantages. It is often necessary to constrain traffic; they are expensive and projects can be time-consuming; the methods are invasive and assessments of the moisture content in a large area, such as several kilometers of road, are often unreliable.

Many authors measure the moisture content using GPR, which is a non-destructive technology. With GPR it is possible to collect data quickly on the road and obtain the volumetric water content of soil in unsaturated porous media, such as sub-asphalt soil[71]. This utility of GPR has been demonstrated for numerous applications in the time domain, based on an evaluation of the dielectric permittivity[72]. Assuming that the porous media is a mixture of three phases (solid, water and air), the dielectric constant of water is significantly different than that of solid materials and air, it is expected that the dielectric constant of the mixture is dependent on the water content.

The relationship between the dielectric constant of a soil and its volumetric water content has been extensively studied in the past. Various empirical correlations have been proposed, like the commonly used theory suggested by Topp, which is supposed to be valid for any type of soil [73]. Another theoretical approach that relates the soil water content to the soil permittivity is based on dielectric mixing. It uses the volume fractions and the dielectric permittivity of each soil constituent to derive an approximate correlation, using a self-consistent approximation that represents the medium with the multi-indicator mode[74].

These aforementioned correlations and models used to evaluate the water content in a porous medium are based on estimations of the dielectric permittivity.

The value of the permittivity is generally extracted from GPR measurements that compute the delay time of reflections once a value for the velocity propagation of the wave in the medium is determined [75]. In some cases, the dielectric permittivity is estimated from the amplitudes of the transmitted and reflected signals [76]. In any case, these methods require calibration steps because the signal velocity of propagation cannot be a priori assumed; in fact, it depends on the characteristics and conditions of the materials. A more efficient and self-consistent approach is based on the GPR processing in the frequency domain.

In this chapter we use the GPR technique for nondestructive monitoring of volumetric water content in the layers of road pavement. As we said earlier most of the models used to calculate the water content in a porous medium are based on the evaluation of electromagnetic properties of the material and the layers of the pavement. The parameter commonly used is the dielectric constant for typical operating frequencies and typical environments detection; is mainly influenced by water content in the soil. The value of permittivity is generally extracted from GPR measurements, calculating the time interval of reflection before determining a value for the wave velocity in the medium [77]

In other cases, the relative permittivity is estimated from the amplitudes of the signals transmitted and reflected[78]. In some cases, however, the volumetric water content can be extracted from a direct analysis of the electromagnetic signal in the frequency domain without the need of having to obtain the value of the dielectric layer.

For this reason, GPR techniques that can be used to estimate the volumetric water content within the layers of the road package can be analyzed and studied with respect to time domain or frequency domain.

Firstly, the signal is analyzed in the time domain: we study the amplitude variations of the received signal as a function of time. In this way the waveform that is obtained is like in the figure 4.1.

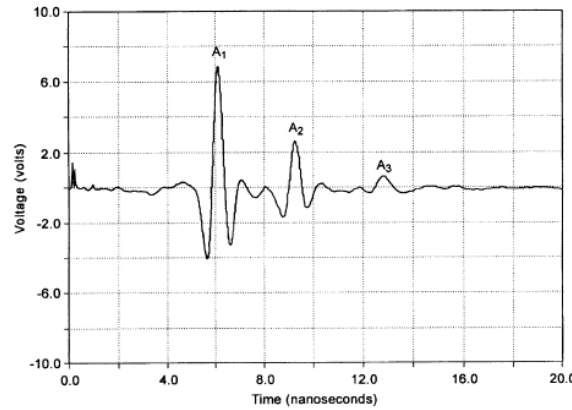


Figure 4.1. Waveform in the time domain

The waveform of the received signal that can be analyzed according to temporal distances of peak amplitude is based on the amount of the same magnitude. It is possible to calculate the differences of time arrival of reflections, this allows to evaluate the wave velocity in the medium and then to calculate the dielectric constant of the layer.

The unsaturated porous medium under investigation can be considered as a mixture of three phases (solid, water and air) which are characterized by a significant difference in the value of dielectric constant with water that has the greatest value of all three.

The methods in the time domain base the estimate of the amount of water on an evaluation of the dielectric constant ϵ , and assuming that the dielectric constant for water is significantly different from that of solid materials and air, we can relate the dielectric constant of the mixture with water content.

If the material has low electrical conductivity and GPR data are acquired using standard antennas operating in medium-high frequency range (~ 100 to 2000 MHz), it

is possible to estimate accurately in time domain the dielectric constant according to the time delay and amplitude of the signal.

In any case, this methods require calibration, because the speed of propagation of the signal cannot be assumed a priori as it depends on the characteristics and condition of the materials.

Secondly, the received signal is transformed into the frequency domain through Fourier transform and the remodeling of the frequency spectrum of the received signal with respect to the transmitted one is analyzed. The process is based on Rayleigh scattering of electromagnetic signal responsible for the remodeling applicable if the incident wave has a wavelength much larger than the size of the object that produces a shift of the frequency spectrum. This modulation is a function of water content in the stratum.

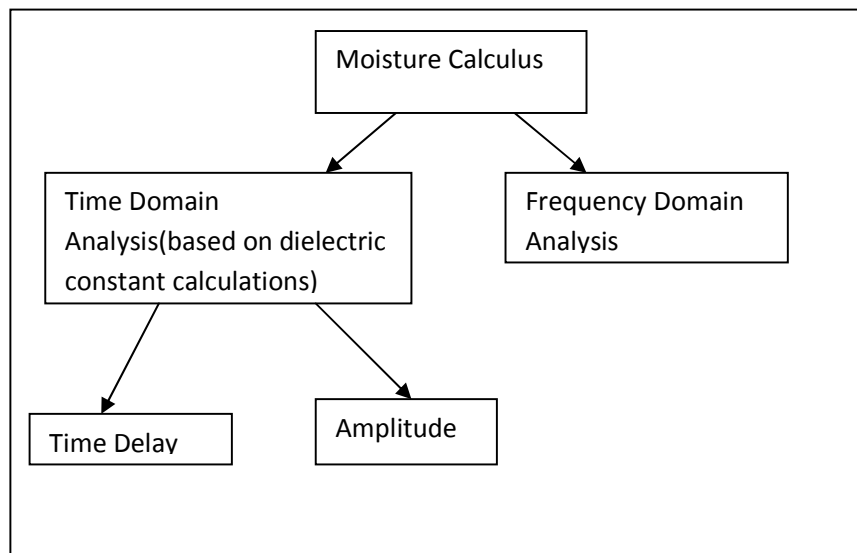


Figure 4.2. Block diagram of the methods of calculation of moisture with GPR.

4.2. Time Delay analysis in Time Domain

The travel time of electromagnetic energy through each layer was calculated as the difference in arrival times of the reflections from the layers of the interface[79]. The difference in arrival times is the distance of time that elapses between the signal transmitted from the antenna transmission and the same signal received by the antenna reception. The travel time of the double passage through the i^{th} layer with the data available is referred to as GPR Δt_i .

To calculate the dielectric constant of each layer, first we calculate the travel time through each level of layer estimating the velocity (v) of the electromagnetic wave in the medium at any point by using the travel time of the double passage and the known average thickness of the layer (h);

$$v = \frac{2h}{\Delta t} \quad (4.1)$$

The velocity of the electromagnetic wave in the medium is then converted to dielectric constant using the formula given by Davis and Annan[74], and the volumetric water content can be estimated using the dielectric constant by the processes that we will see in next section.

$$\varepsilon = \left(\frac{c}{v}\right)^2 \quad (4.2)$$

where c is the velocity of propagation of plane electromagnetic waves in free space ($c = 0.3 \text{ cm / ns}$) and v is the velocity of the electromagnetic wave within the previously estimated layer of pavement.

The test requires knowledge of the thickness h of the layers of the pavement through invasive testing such as on-site drilling or boreholes. If the thickness of the layers is unknown then we can assume a crossing speed v of the material according to

its characteristics and come to the calculation of layer thickness h , and the dielectric constant ε by the following formulas:

$$\begin{cases} h = \frac{2v}{\Delta t} \\ \varepsilon = \left(\frac{c}{v}\right)^2 \end{cases} \quad (4.3)$$

The method appears to be easy to use and apply immediately for almost any environment, without errors in the estimate of the dielectric constant due to attenuation of amplitude.

The data of travel time provide a precise evaluation of the dielectric constant for base layers formed from aggregate material and located underneath the asphalt. The result of the dielectric constant is quite accurate and fully reflects the value that calculated through laboratory analysis. Measurements of the dielectric constant through time travel are more accurate when the geometry of the subsurface is known or when data are collected with variable offset.

The GPR data with a higher frequency have a higher resolution and therefore lead to more accurate measurements of travel time compared to the data with lower frequency [80].

In contrast, the method requires calibration, because the speed of propagation of the signal cannot be assumed a priori as it depends on the characteristics and condition of the materials. So you need to associate to the measurements with GPR, destructive investigations like drilling in order to extract the necessary information as the true thickness of the layers and homogeneity of the material in each layer.

This means that only measurements made at the sample are really significant and not always the results are extendable to the whole domain of analysis due to the heterogeneity of the system.

4.3. Amplitude analysis in Time domain

The amplitude of reflection GPR data can be used to estimate the dielectric constant in many areas of detection. The amplitude of the GPR received signal is a function of the strength of the transmitted signal, the distance between the GPR antennas and the surface of land, the route of transmission, electromagnetic attenuation (α) of materials and interfaces encountered in the subsurface by the signal.

The amplitude decreases as the travel path and the attenuation increases, GPR signal cannot be detected after very short travel paths in environments with very high attenuation [81]. The dielectric constant of the layers can be determined directly through analysis of the amplitudes of reflection of the interface between two different layers. The amplitude of reflection is linked to the percentage of energy that is reflected from an interface or transmitted to the next level; high-amplitude reflections indicate a high contrast between the dielectric constants of the layers. For example, a wet layer (with high dielectric constant) in a dry layer (a low dielectric constant) would produce high amplitude reflections while the two layers with water content would give a reflection of low amplitude.

The amplitude of the reflection coefficient (Γ_{12}) can be used to quantify the percentage of energy reflected in an interface that features the top layer of dielectric constants (ϵ_1) and lower (ϵ_2):

$$\Gamma_{12} = \frac{\sqrt{\epsilon_1} - \sqrt{\epsilon_2}}{\sqrt{\epsilon_1} + \sqrt{\epsilon_2}} \quad (4.4)$$

To use the reflection coefficient in evaluating the dielectric constant of a lower layer, it is first necessary to determine the dielectric constant of the layer above. For GPR data of the first layer, the dielectric constant of the material above it (air), is known ($\epsilon_{\text{air}} = 1$). Thus, the extent of air-ground interface reflection can be used to determine

the dielectric constant of the surface material, after which the amplitude of air-ground reflection was calibrated with the amplitude of a reflection of a large metal plate.

The formula used for calculating the dielectric constant of the surface layer from the data by size of air-ground is given by[82]:

$$\varepsilon_a = \left(\frac{1 + A_1/A_m}{1 - A_1/A_m} \right)^2 \quad (4.5)$$

where A_m = amplitude of the reflection of a large metal plate in volts per meter (100% reflection wave EM) and A_1 = amplitude of the reflection interface air - surface in volts per meter.

After calculating the dielectric constant of the surface material, the dielectric constant can be estimated by the underlying layers using the amplitude of reflection of the deeper interfaces;

$$\sqrt{\varepsilon_b} = \sqrt{\varepsilon_a} \left[\frac{1 - \left(\frac{A_1}{A_m}\right)^2 + \left(\frac{A_2}{A_m}\right)}{1 - \left(\frac{A_1}{A_m}\right) + \left(\frac{A_2}{A_m}\right)} \right] \quad (4.6)$$

where, ε_b = the dielectric of the base layer; A_2 = the amplitude of reflection from the top of the base layer in volts per meter.

From the value of the dielectric constant found, we can calculate the thickness of the layers:

The first layer thickness (surface: layer a)

$$h_a = \frac{c \times \Delta t_a}{\sqrt{\varepsilon_a}} \quad (4.7)$$

The second layer thickness

$$h_b = \frac{c \times \Delta t_b}{\sqrt{\epsilon_b}} \quad (4.8)$$

where h_i is the thickness of the i^{th} layer, c is the velocity of the electromagnetic plane wave in the free space ($c = 0,3 \text{ m/ns}$), Δt_i the time delay between two peaks at the ends of the layer and ϵ_i is the dielectric constant of the i^{th} layer.

The formulas, very simple to apply, does not need to know the thickness of the layers and the velocity of EM wave through the medium. The amplitude of the reflections data of the interfaces can also be used to assess the spatial distribution of water content such as wet areas or dry immediately under the layer or any deposits of water trapped between each layer in order to understand the possible flow pattern. It is also possible to detect the degradation and deterioration in the road package and information about the homogeneity of the material [83].

These simple equations have proved to work well for flexible pavements over granular bases; it suggests that they give good results because there is no signal attenuation in the surface layers of bitumen mixture. This assumption seems reasonable for flexible pavements and also gives values for the dielectric base layers if the surface layer has a thickness greater than 6 cm. However, the calculations become less reliable for rigid concrete pavements and for calculations of the dielectric constant of a substrate under a layer of granular base [84].

However, the equations used to approximate the dielectric constant data from the amplitude of the reflections do not take into account the attenuation of the GPR signal in the air with increasing distance of propagation. This omission does not significantly affect the accuracy of the dielectric constant estimated since the attenuation of electromagnetic energy in the air is generally low[85].

The attenuation of GPR signal for the materials used for road pavement is often significant and may reduce the accuracy of estimates of the dielectric constant from

the amplitude data, especially for the deeper layers of the underground. For example the method of the amplitudes cannot be used to estimate the dielectric constant of the aggregate layers of pavement using the formulas previously described when the materials have a very high electrical conductivity and thus high attenuation. For this reason, the measurements are unreliable even for the rigid road pavement, for the substrates in granular layers and all conductive materials (clay and salt deposits of water).

Furthermore, since the frequency-dependent attenuation of electromagnetic wave, it is preferable to use low-frequency GPR signals to contain the losses of the field and increase the depth of investigation.

In cases where you cannot use the data to estimate the magnitude of the dielectric constant of the material, these can be qualitatively analyzed to indicate the degree of contrast between the dielectric constants of the different layers and then evaluate the difference between the different water content[86].

4.4. Frequency domain analysis

It is still a method under study and is very innovative because, regarding other methods previously described it does not require calibration for estimating the water content in a porous medium through a GPR system. It is assumed that by varying the moisture content in an unsaturated porous medium, there is a different absorption of the radar signal as a function of frequency. In other words, this corresponds to a reshaping of the frequency spectrum of the received signal than that transmitted as a function of water content. Therefore by knowing the content of the frequency spectrum of signals transmitted and received, is theoretically possible to extract moisture below the structure under study.

This method unlike the other does not require calibration because it does not estimate the dielectric permittivity of the unsaturated soil water content but directly by the frequency analysis[87].

4.4.1. Rayleigh scattering

It is well known that an electromagnetic wave passing through a medium deviates from a straight trajectory by one or more localized non uniformities. This general physical process is called scattering. When an electromagnetic wave is affected by only one localized scattering center the process is called single scattering; otherwise, when scattering centers are grouped together, the electromagnetic wave may scatter many times, which is known as multiple scattering. The wave propagation in dielectrics could be described by using the following model: the space is divided into two regions, or stratified media, separated by a surface. A first region contains the wave source; the wave propagates into the second region passing through the surface.

This is applied to GPR inspection, but any rigorous analytical approach should be much approximated because the media encountered in the second region is very heterogeneous, anisotropic and asymmetric in the spatial scale of soil particles and dispersed water. In the case of GPR, there are multiple scattering events for impulse propagation in a three-phase porous medium comprising numerous different materials, typically air and water. When the dimensions of the non-uniformities that cause the scattering are much smaller than the wavelength, the process is described as Rayleigh scattering. In this thesis Rayleigh theory is used to explain a new method applied to geophysical measurement of moisture content in porous media.

As it will be discussed later this approach introduces the measurement of the moisture content from frequency spectra analysis without any calibration of the system, which is always required when moisture content is calculated from the signal

amplitude or signal processing in time domain. From a practical point of view this is a relevant point of innovation for engineers and practitioners.

The intensity I of the electromagnetic wave scattered by a single particle for a beam of unpolarized waves with a wavelength λ and intensity I_0 is given by:

$$I(\theta) = I_0 \frac{1+\cos^2\theta}{2R^2} \left(\frac{2\pi}{\lambda}\right)^4 \left(\frac{n^2-1}{n^2+2}\right)^2 \left(\frac{d}{2}\right)^6 \quad (4.9)$$

where R is the distance from the observer to the particle, θ is the scattering angle, n is the refractive index of the particle and d is the diameter of the particle.

The angular distribution of Rayleigh scattering, governed by $(1+\cos^2\theta)$ term, is symmetric in the plane normal to the incident direction of the wave; thus, the forward scattering is equal to the backwards scattering. Integrating over a sphere surrounding the particle gives the Rayleigh scattering cross section[88]

$$\sigma_s = \frac{2\pi^5}{3} \frac{d^6}{\lambda^4} \left(\frac{n^2-1}{n^2+2}\right)^2 \quad (4.10)$$

4.4.2. Refractive index and dielectric permittivity

Assuming the following constitutive equations,

$$\mathbf{D} = \epsilon_0 \mathbf{E} + \mathbf{P} \quad (4.11)$$

$$\mathbf{B} = \mu_0(\mathbf{H} + \mathbf{M}) \quad (4.12)$$

under the hypotheses of a non magnetic medium, linear polarization, absence of free charge, null current density, the following equation derives from Maxwell equations for propagation in a medium:

$$\nabla^2 E - \epsilon_0 \mu_0 (1 + \chi) \frac{\partial^2 E}{\partial t^2} = 0 \quad (4.13)$$

where the refractive index n is given by:

$$n = \sqrt{1 + \chi} = \sqrt{\epsilon_r \mu_r} = \frac{c}{v} \quad (4.14)$$

In a three-phase porous medium such as soil the value of μ_r is approximately 1. The assumption of zero electrical conductivity is not valid for unsaturated and saturated soils. But if electrical conductivity is not too high, the effect on the reflection coefficients can be neglected on first approximation. However in this case it will still influence the wave attenuation.

The dielectric permittivity of a three-phase medium plays the most important role in determining n . Considering that the dielectric permittivity is 1 for air, approximately 3 to 6 for solid particles and 81 for water, the value of ϵ_r for a given medium is strongly influenced by the moisture content[89].

Moreover, water molecules are dipoles that can be oriented by an external electrical field. If this electric field varies with a significantly long period, then the dipoles have the time to change orientation and the physical process of dipolar polarization is observed. The time needed for dipoles to change their orientation is called the Debye relaxation time[90]. The change to the orientation of the dipoles is opposed by random molecular agitation.

If the period of the electric field is 10^{-3} to 10^{-12} s, the dipoles can be polarized. In the present case, the frequency of the EM field used for GPR is centered at 600 MHz, giving a period of 1.7×10^{-9} s; this period is long enough to allow for dipole polarization. Atomic and electronic polarizations are not induced in the medium if the period of the electric field is less than 10^{-14} and 10^{-16} s, respectively.

The polarization of a medium implies that the value of the dielectric permittivity of a three-phase medium depends on the frequency ν of the EM wave. The following Debye model will be assumed in this thesis, where τ is the relaxation time:

$$\epsilon_r = \epsilon_\infty + \frac{\Delta\epsilon}{1+j\nu\tau} \quad (4.15)$$

where

$$\Delta\varepsilon = \varepsilon_{static} - \varepsilon_{\infty} \quad (4.16)$$

is the difference between the value of the dielectric constant of the medium observed for a steady electromagnetic field and the value for a high frequency field when the medium is totally polarized.

Equation (4.15) can be written by separating the real and imaginary part of ε_r as follows:

$$\varepsilon_r = \left[\varepsilon_{\infty} + \frac{\Delta\varepsilon}{1+v^2\tau^2} \right] - \left[j \frac{v\tau\Delta\varepsilon}{1+v^2\tau^2} \right] \quad (4.17)$$

Considering the equation (4.14) and (4.17) , equation (4.9) can be rewritten as follows:

$$I(\theta, v) = I_0(v) \frac{1+\cos^2\theta}{2R^2} \left(\frac{2\pi v}{c_0} \sqrt{\mu_r \left(\varepsilon_{\infty} + \frac{\Delta\varepsilon}{1+v^2\tau^2} \right)} \right)^4 \times \left(\frac{\mu_r \left(\varepsilon_{\infty} + \frac{\Delta\varepsilon}{1+v^2\tau^2} \right) - 1}{\mu_r \left(\varepsilon_{\infty} + \frac{\Delta\varepsilon}{1+v^2\tau^2} \right) + 2} \right)^2 \left(\frac{d}{2} \right)^6 \quad (4.18)$$

4.4.3. The relaxation time

The relaxation time of a single molecule of water can be calculated according to Stokes law:

$$\tau = \frac{4\pi\eta R^3}{k_B T} \quad (4.19)$$

where k_B is the Boltzmann's constant, $\eta(T)$ is the viscosity, which varies with the absolute temperature T , and R is the approximate radius of the molecule; the value generally assumed for R is between 1.4 and 2.8 Å, depending on the temperature. Consequently, the relaxation time of a molecule in free water can vary between 1 to 10 picoseconds [91].

Of course, for the case of water droplets dispersed in a porous medium or for multiple water molecules adsorbed to solid particles by dipolar forces, the inertia of the water dipoles elongates the relaxation time. Analogous results have been found previously for biological materials [92].

In all these cases the relaxation time can be until 1000 times greater than in pure water. For clayey materials the relaxation time is found to vary to about 30 nanoseconds depending on the interfacial polarization [93,94]. Since there is no literature on the exact value of the relaxation time in the case of water dispersed in a soil or in a clayey soil, because it can vary depending on minerals concentrations and polarization according to the range of variability found in the cited literature, its value is considered in a calibrated parameter in the simulations that are presented in the next section.

4.5. Evaluation of volumetric water content with GPR

In order to verify the consistency of theory and to analyze the effectiveness of the methods described above on the calculation of volumetric water content in the layers pavement, GPR measurements was carried out in an existing real and flexible layer pavement (road located in the province of Rieti, and specifically in the town of Greccio). For measurements we use two type of GPR devices.

This GPR has been used both as a monostatic type and used the same antenna for transmitting and receiving, but with two different nominal frequencies. The first one, who belong to the Science of Civil Engineering Department of Roma Tre University, has used a frequency of 600 MHz while the second GPR who belong to the GEO 3D used a nominal frequency of 1000 MHz. The data were then processed using Matlab computing software, and displayed through the software module Gred/s.

Using the second and third method outlined in the section above for the calculation of moisture content, it was possible to analyze the variation in water content along the longitudinal and transverse tracks. It has also been made a comparison of results obtained through the use of two different methods.

Through an analysis of radar maps it was possible to identify the underground crossing, any manhole covers and decks of bridges. Finally, an analysis of radar data and the presence on a deteriorated pavement allow us to define a new perimeter of the landslide.

4.5. 1.The road under investigation

In this section, the GPR technique was used on a provincial road called "Reopasto" located in the province of Rieti in the town of Greccio at the foot of the Sabine Mountains, the road connecting the towns of Contigliano, Limits of Greccio and then finally take on state road 79 for a total length of 24.3 km.

The road section under investigation begin from the town of Spinaceto and limits to Greccio for a total length of 1.5 km (from km 9.2 to km 10.7). In this stretch the road deck has a mean width of 6.5 meters and consists of two lanes, one in each direction, a width of 3 meters each and a quay side of 0.25 meters. This section of road is affected by a large proportion of dormant landslide that fits over the entire hilly area located on the side immediately above the road between the villages of Greccio, Limits of Greccio and Castellina.

The landslide is composed of more landslides in different amounts each characterized by a specific type of movement, activity status and lithological characteristics. The lands involved are made up of clay reliefs alternating with marly

debris resting on clay, also with the presence of carbonate rocks, silt and pelitic flysch.

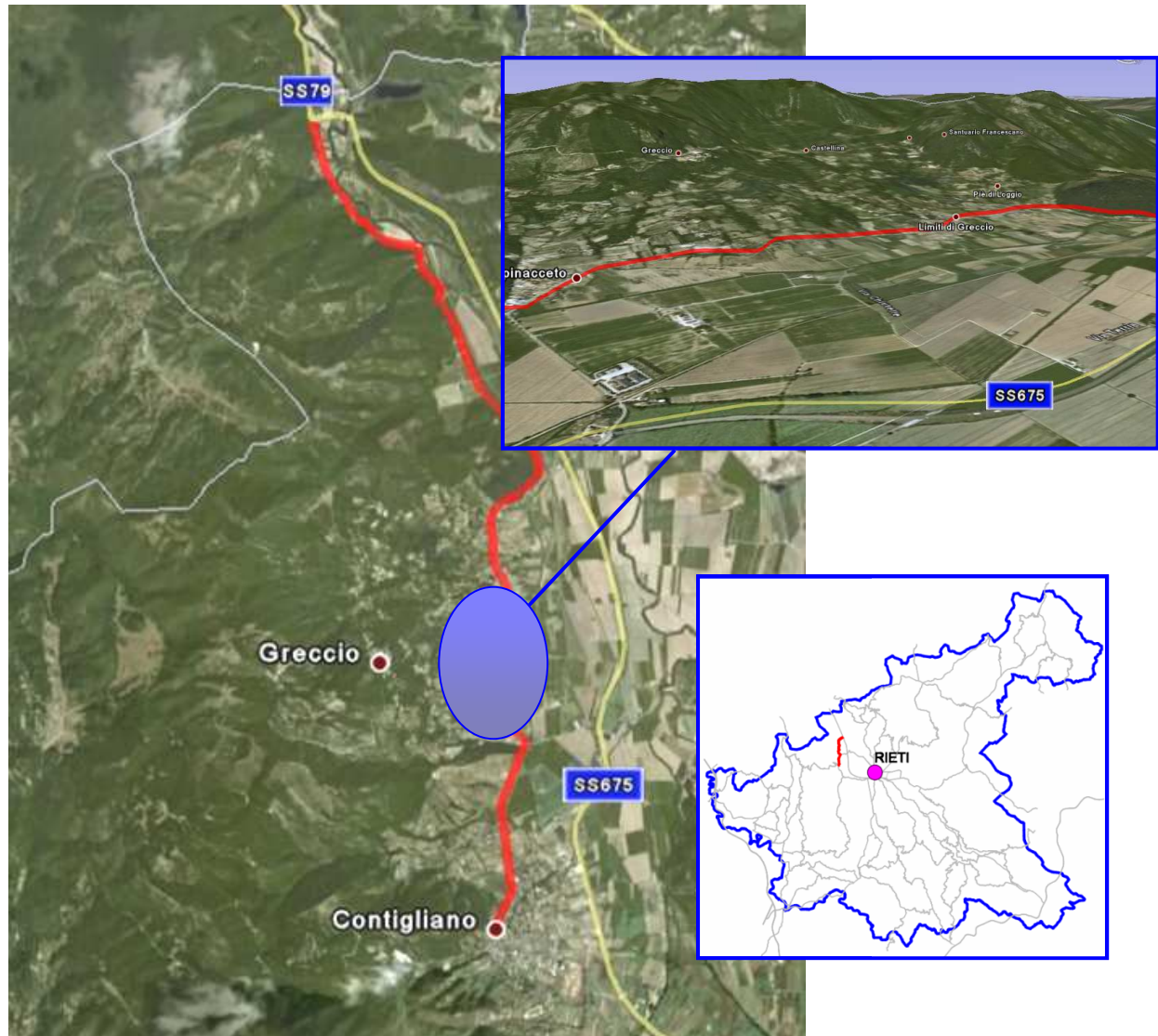


Figure 4.3: Image Google Earth for the classification of area



Figure 4.4 From satellite for area under study

The landslides are identified by a translational slide slow and regular debris cover the surface and were also observed rock falls in the area and the presence of major fault systems.

The road package pavement investigated is type flexible who consists of two layers having different characteristics resting on the background of land site. The surface layer is asphalt with the functions of absorbing the shear stress caused by the passage of vehicles; this layer has a thickness varying between 8 and 12 cm.

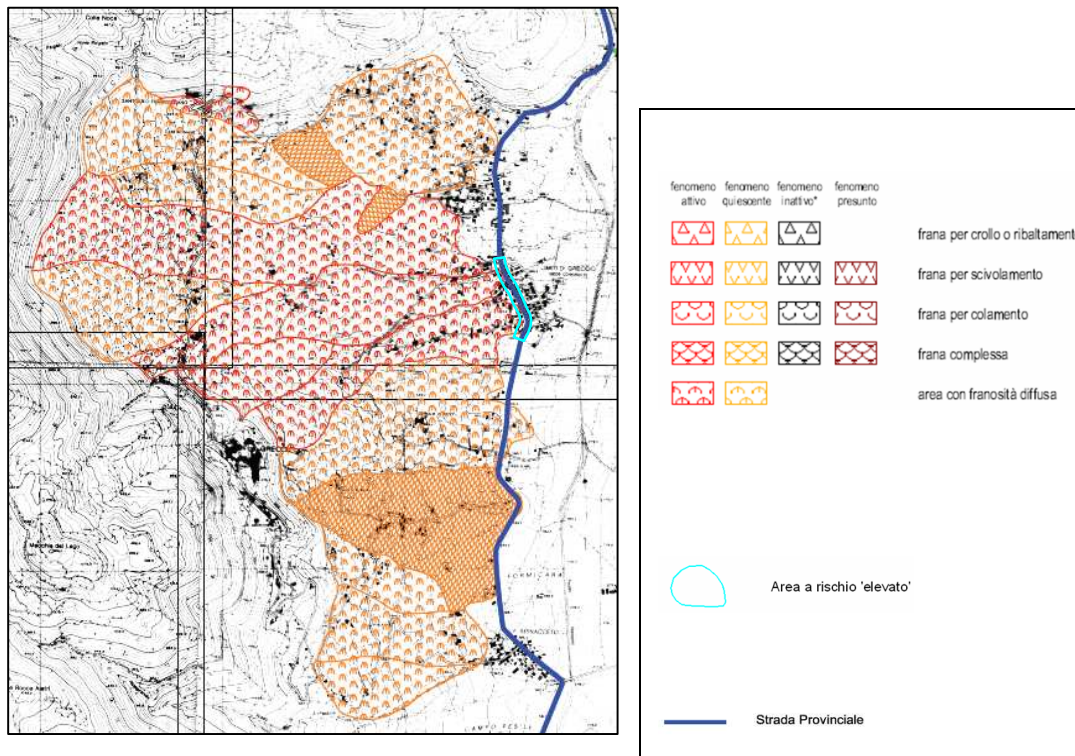


Figure 4.6. Delimitation area of the landslide interesting the road

The second layer is the foundation and its function is mainly to absorb normal stresses caused by the weight of vehicles and distribute loads on the substrate. This layer is mixed granular and has an average thickness of about 15 cm.

4.5.2. Used ground penetrating radar

The GPR equipment used to carry out the survey on road package were two:

The first property of Science of Civil Engineering Department of the Roma Tre University is a ground penetrating radar acquisition pitched RIS 99 IDS (Ingegneria Dei Sistemi spa) with data acquisition and control unit, a battery power supply and a block antenna in a mobile carriage for transportation. The block antenna contains two antennae for the transmitting and receiving the electromagnetic signal to the working

frequency of 600 MHz and 1600 MHz (both in transmission and reception). The task of the entire acquisition unit is pitched to acquire the data of the investigated area and to record on magnetic media and then transfer them on processor resident in the laboratory.

It is possible to move the device along the track of investigation at the base with four wheels in contact with the pavement. The radar measurements were conducted using four channels, two bistatic (transmission to one antenna to the other, and vice versa) and two monostatic (transmitter and receiver from the same antenna, 600 MHz or 1600 MHz). For the processing of data, we used monostatic channel with transmit and receive frequency of 600 MHz.

The second GPR used, property of the GEO 3D is a SIR 3000 with antenna GSSI (Geophysical Survey Systems Inc.) working at a nominal frequency of 1000 MHz. The GPR consists of a block antenna resting on the ground by four wheels with small diameter and a control unit for signal generation and real-time display of acquired data on screen.



Figure 4.7. Block antenna GSSI and unit control

4.5.3. Modality of execution of GPR measurements

The measurements were done as saying before for 1,5 Km on an existing flexible pavement consists of a top layer of asphalt of the average thickness of 10 cm, a foundation layer in granular mixture of the average thickness 15 cm resting on a foundation layer of variable thickness.

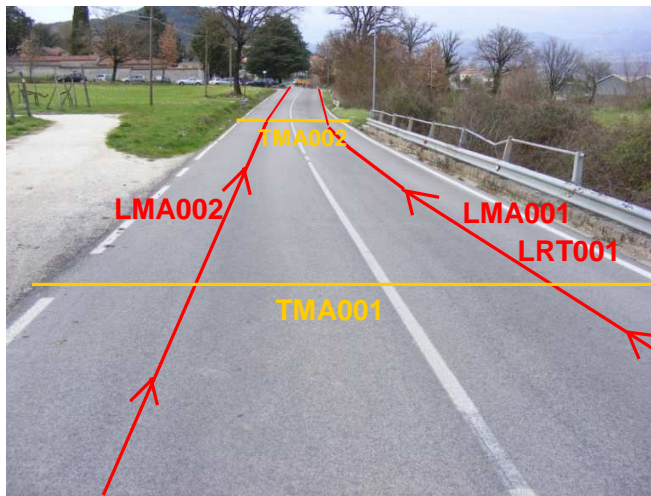


Figure 4.9: method of data acquisition

The measurement was performed by moving the GPR system with antennas at 600 MHz along a longitudinal track to the road for a total length of 1500 meters at a distance of 1 meter from the edge of the lane on both lanes. The investigation took place before in the right lane (direction Spinaceto – Greccio) along the track we called "LMA001" and then the left lane

(direction Greccio - Spinaceto) along the track we called "LMA002. The SIR 3000 GPR system was used only for the longitudinal right track that was called "LRT001.

It was subsequently made acquisitions along the GPR cross-sections placed at a constant distance of 100 meters for a total of 16 sections of about 6.5 meters long, each thus forming a grid and provide the longitudinal acquisition of which affect the whole width of the road platform. These acquisitions have been called with the statement that changes the value of a TMA001 to TMA016 according to section of detection.

As to the second GPR survey was carried out with a frequency of 1000 MHz only on the right track always at a distance of 1 meter from the edge of the right edge of the roadway.

Given the possibility of using two different GPR systems it was possible to work simultaneously with both, but without bringing the two systems over the limit of influence of the antennas. Thus it was possible to give the radar data, measured with different frequency, a contemporary character.

4.5.4 Data processing

For processing and analysis of GPR data acquired with measurement and the visualization on radar maps the Matlab software and the module Gred/s software have been used in order to represent the signal as matrix in an array of numbers. The Matlab software allows us to represent data as matrix and the GRED/S allow us to have an overview of the radar maps. This software is given with the GPR system and is available in the department of Science of Civil Engineering at Roma Tre University.

The acquired signal is composed of an array of numbers where each column corresponds to a single electromagnetic pulse received by the antenna whenever it is run through a constant distance of 2.4 cm displacement of the wheel, and each row is immediately on receipt of single-pulse by the antenna. In this way, the data obtained is composed of an array of numbers with a constant number of rows equal to 512 and a number of columns varies depending on the length of the track radar. The value inside each box of the matrix corresponds to the amplitude in volts per meter of a single instant of time signal reception.

The Matlab code used made it possible to find the average signal of all electromagnetic waves received, to apply the Fast Fourier transform (FFT) to transform the signal from time domain to frequency domain, to calculate the peak of the frequency spectrum of single signal and then calculate the dielectric constant of the surface layer, foundation and background.

For each track, in order to eliminate the air gap between the antenna and the first air-soil interface, appropriate translation or shifting of the signal is used to align the depth scale of the map at the current radar position of the plane surface investigated.

4.5.6. Results and discussion

Through the development of radar tracks using the procedures described above, could be determined, for each pulse of each trace, either the shift of the peak frequency, or the value of the dielectric constant, calculated by the method of the amplitudes of the three layers up the road package. These values were plotted on two-dimensional diagrams as a function of distance of investigation (in meters) for all tracks. For a better understanding of the values obtained, we built the polynomial trend line, also to facilitate the comparison of different graphs together.

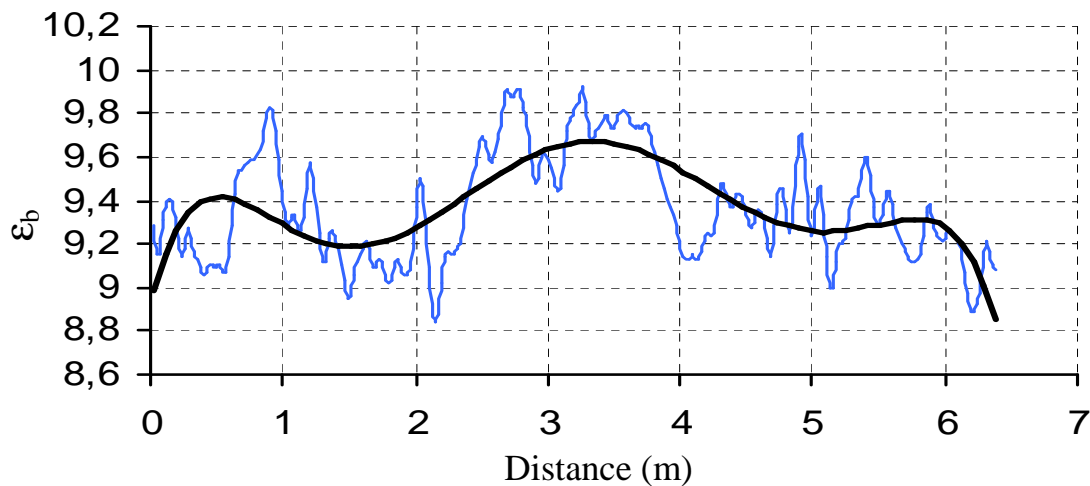


Figure 4.10. Dielectric constant of layer foundation

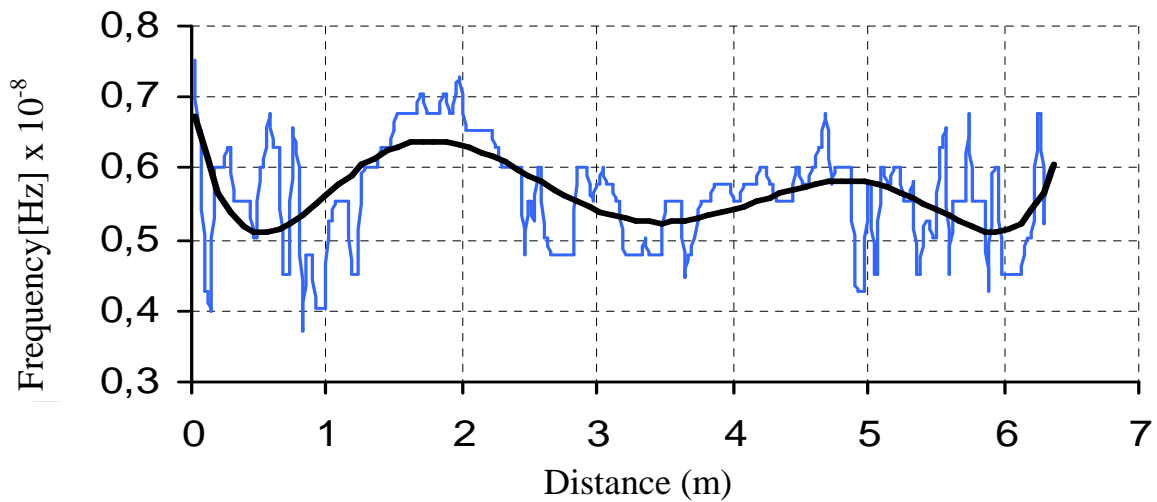


Figure 4.11. Peaks of frequency of layer foundation

It has been studied, in previous section, how to analyze the signal in both time domain and frequency domain and it is possible to obtain the volumetric water content at each point of the package of pavement and determine its spatial variation along the cross sections examined and along the total length of 1500 meters of road investigated.

Recalling what was previously said, we saw that a minimum presence of moisture in the material constituting the layer leads to substantial changes in the value of the dielectric constant as the water relative permittivity ($\epsilon_r = 81$) is much greater than that of any dry material used to the construction of the road structure ($\epsilon_r = 4 - 10$). Therefore high values of dielectric constant correspond to high water content and vice versa.

Unlike the case of the peak frequency as we have that, according to the Rayleigh scattering, with increasing moisture, the peak of the spectrum shifts toward lower frequencies.

An analysis of dielectric values and those of the peak values of the frequency spectrum made for all tracks performed (and the two longitudinal right and left, both the cross) has been able to confirm this theory in part because the two trends of the two graphs (dielectric constant and peak frequency) was virtually the opposite. This means that in one hand, with high values of dielectric constant we have obtained lower peak values of the frequency spectrum as the water content was higher. In another hand, for low values of dielectric constant we have obtained high peak values of the frequency spectrum as the water content was minimal. In addition, a comparison of the dielectric constant of the layer of foundation with that of the background shows that the trends are the same.

In this case we were not interested in the calculation of the absolute value of moisture content, but simply an assessment of the value in what appears to be directly proportional to the dielectric constant of the material through the polynomial relations that we saw in the section above.

For cross-sections it was possible, through the radar maps, to see the development of interfaces between surface layers and layer of foundation and between the foundation and background. In addition, having previously set a constant speed of propagation of electromagnetic wave inside the medium of 100 cm/ns, it was possible to approximately calculate the thickness of the layers making up the pavement.

The radar maps instead of longitudinal sections were used for the detection of any underground services crossing (electricity, gas, methane, etc) for the identification of decks of concrete bridges or culverts for crossing water side and spring from the mountain, and especially to see any level of groundwater and the presence of the landslide that more or less interested in the road. In fact, as we saw in the previous paragraphs, the stretch of road from km 9.200 to km 10.700 tested for moisture by GPR survey is affected by dormant landslide of vast proportions which

lies across the hilly area located on the side immediately above the road. The landslide is composed of more landslides in different amounts each characterized by a specific type of movement, activity status and lithological characteristics.

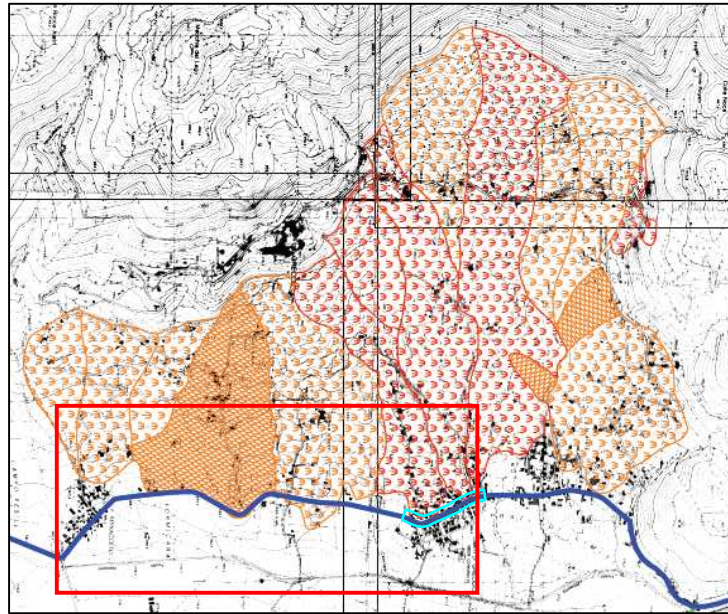


Figure 4.12. Delimitation of area of landslide Lazio Region

The perimeter of the landslide was carried out from the inventory of landslide areas of the Lazio region around the year 1998.

Through the GPR survey carried out on the road structure for the purposes of calculating the water content, it was also possible to determine if indeed the perimeter of the landslide is actually detected by the Lazio Region and if over time the phenomenon had been given a progress downstream.

To do this the first step was to analyze the longitudinal radar maps available to us and see if there were anomalies when the tracks ran through the area subject to landslide.

In fact, it was possible to note that the track of road affected by the landslide; in which we had radar map in which there was a additional interface placed deep in the soil background due to high amplitude values and caused most probably by increased water content. Here is an example of the radar map of the track from the left at km 1,216 to km 1,244.

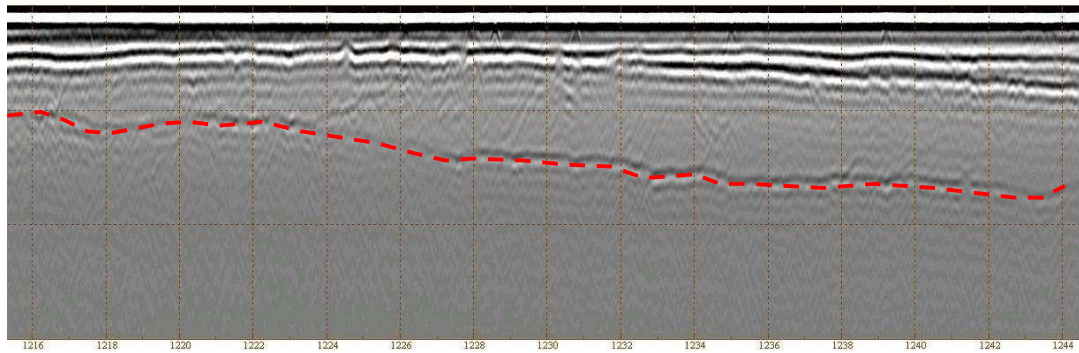


Figure 4.13. Delimitation area of landslide of S.P.1

It is seen very clearly that the interface we talked about previously and which we have outlined in red, which is an increase in moisture content. This may be associated with a condition that may suggest the presence of the landslide or less quiescent.

In a second phase, by analyzing the corresponding diagrams of dielectric constants and peak frequency, and at such interfaces which increases the moisture content, and where it is assumed that the soil is affected by the phenomenon of landslide, there are consequently high values of dielectric constant and a shift of the peak frequency towards lower values.

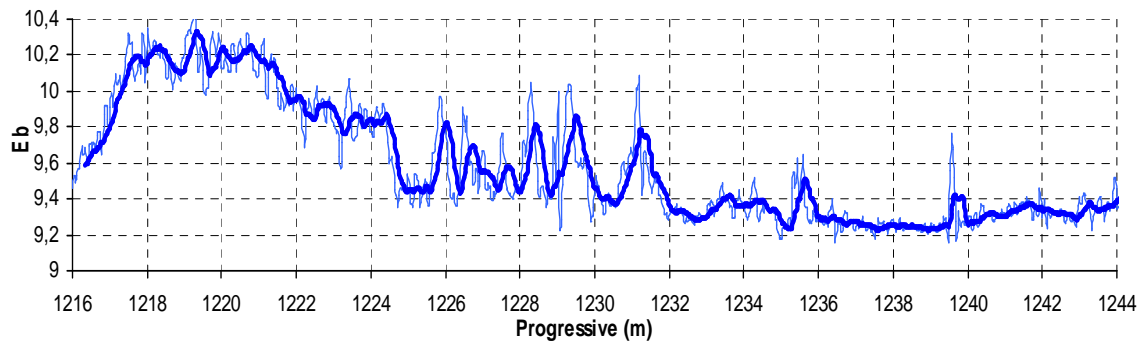


Figure 4.14. constant dielectric

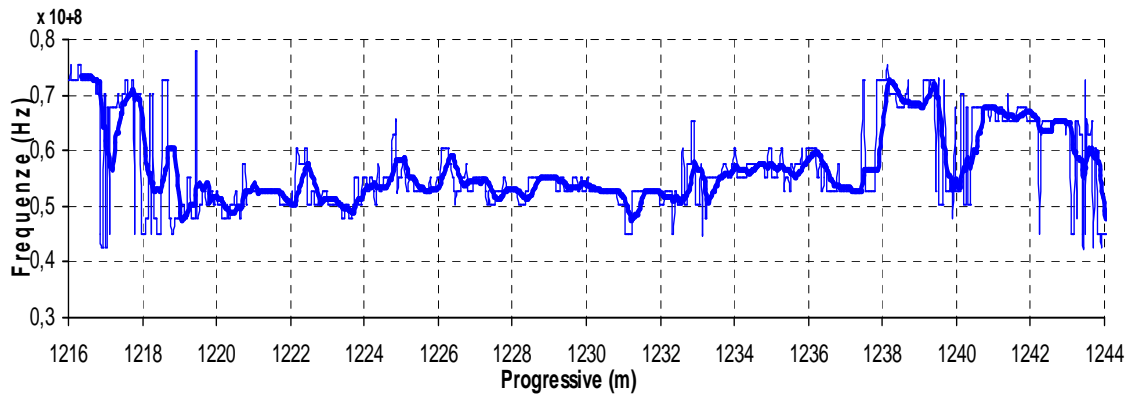


Figure 4.15. Peaks of frequency

In the final analysis, it was carried out an analysis of the surface instability and the inventory of all the cracks and holes in the plan of road pavement because it gives tangible proof of a background soil in the continuous movement. Based on the analysis procedure just explained we made a new perimeter of the landslide and highlighted in a plan an inventory of the deterioration of the pavement.

This demonstrates that the GPR techniques can help more to make an inventory of the deterioration pavement and to predict as soon as possible for the good monitoring of the road structure. This technique was helpful to understand the mechanism of the monitoring and how it is possible to make a study of road survey.

The experience shows that it is possible to extend the technique for others structure and domain studies.

Conclusion

In this thesis, a problem of an electromagnetic scattering by buried object has been studied. From the Maxwell's equation for which the theory of the electromagnetic scattering is founded, and the method of solving this equation, the one of many applications of this theory is the Ground Penetrating Radar.

After recalling the principle of a GPR, in this study a GPR was used to carry out on two important applications. The first one was the study of how to use the GPR for Landmine detection. In a sandbox filled with dry sand, where buried different object, it is seen that the GPR was capable to detect the object with a percentage of reduce false alarm. This was in good agreement with the simulation. This benchmarking laboratory allow us to have a good know how with the practice for working with a GPR instrumentation.

The case treated in this thesis was a controlled environment but in the reality, the environment in which the landmines are buried content moisture like in the tropical zone and the sandy area that content somehow the moisture. The results give us more curiosity and in the future we can investigate and use the GPR in the area with considerable moisture.

The second application was to use the GPR survey in the road monitoring. Nowadays, the GPR are becoming the major instrumentation to investigate in order to study the degradation of road pavement due to movements and instability of geomorphological nature. Usually it is easy to locate the damage whereas it is difficult to identify the causes. The rehabilitation can be compromised, if the cause is not removed.

In this thesis we use the GPR technique for nondestructive monitoring of volumetric water content in the layers of road pavement. The models used to calculate

the water content in a porous medium are based on the evaluation of electromagnetic properties of the material and the layers of the pavement. The parameter commonly used is the dielectric constant for typical operating frequencies and typical environments detection; is mainly influenced by water content in the soil. The value of permittivity is generally extracted from GPR measurements, calculating the time interval of reflection before determining a value for the wave velocity in the medium.

While in the Landmine detection, the GPR is still seen with most difficult to be used in the environment with great moisture, in the road monitoring as we have seen in our research, is most advanced and can be used by replacing the others techniques.

Bibliography

- [1] A. Q. Howard, "The electromagnetic fields of a subterranean cylindrical inhomogeneity excited by a line source," *Geophys.*, vol. 37, pp. 975–984, Dec. 1972.
- [2] B. P. D'Yakonov, "The diffraction of electromagnetic waves by a circular cylinder in a homogeneous half-space," *Bull. Acad. Sci. U.S.S.R., Geophysics*, pp. 950–955, 1959.
- [3] S. O. Ogunade, "Electromagnetic response of an embedded cylinder for line current excitation," *Geophys.*, vol. 46, pp. 45–52, Jan. 1981.
- [4] S. F. Mahmoud, S. M. Ali, and J. R. Wait, "Electromagnetic scattering from a buried cylindrical inhomogeneity inside a lossy earth," *Radio Sci.*, vol. 16, no. 6, pp. 1285–1298, Nov.–Dec. 1981.
- [5] N. V. Budko and P. M. van den Berg, "Characterization of a two-dimensional subsurface object with an effective scattering model," *IEEE Trans. Geosci. Remote Sensing*, vol. 37, pp. 2585–2596, Sep. 1999.
- [6] C. M. Butler, X.-B. Xu, and A. W. Glisson, "Current induced on a conducting cylinder located near the planar interface between two semi-infinite half-spaces," *IEEE Trans. Antennas Propag.*, vol. AP-33, no. 6, pp. 616–624, Jun. 1985.
- [7] K. Hongo and A. Hamamura, "Asymptotic solutions for the scattered field of plane wave by a cylindrical obstacle buried in a dielectric half-space," *IEEE Trans. Antennas Propag.*, vol. AP-34, no. 11, pp. 1306–1312, Nov. 1986.
- [8] I. N. Sneddon, *Mixed Boundary Value Problems in Potential Theory*. Amsterdam: North-Holland, 1966.

- [9] Q. A. Naqvi, A. A. Rizvi, and Z. Yaqoob, "Asymptotic solutions for the scattered field of plane wave by a cylindrical obstacle buried in a dielectric half-space," *IEEE Trans. Antennas Propag.*, vol. 48, no. 5, pp. 846–848, May 2000.
- [10] , "Scattering of electromagnetic waves from a deeply buried circular cylinder," *Progress in Electromagnetic Research*, vol. 27, pp. 37–59, 2000.
- [11] J. L. Tsalamengas, "Electromagnetic scattering from conducting circular cylinders in the presence of a stratified anisotropic medium—TM case," *IEEE Trans. Antennas Propag.*, vol. 37, no. 12, pp. 1582–1590, Dec. 1989.
- [12] J. D. Kanellopoulos and N. E. Buris, "Scattering from conducting cylinders embedded in a lossy medium," *Int. J. Electron.*, vol. 57, pp. 391–401, Mar. 1984.
- [13] G. Cincotti, F. Gori, M. Santarsiero, F. Frezza, F. Furnò, and G. Schettini, "Plane wave expansion of cylindrical functions," *Opt. Commun.*, vol. 95, pp. 192–198, Jan. 1993.
- [14] F. Ciambra, F. Frezza, L. Pajewski, and G. Schettini, "A spectral-domain solution for the scattering problem of a circular cylinder buried in a dielectric half-space," *Progress Electromagn. Research*, vol. 38, pp. 223–252, 2002.
- [15] R. Borghi, F. Gori, M. Santarsiero, F. Frezza, and G. Schettini, "Planewave scattering by a perfectly conducting circular cylinder near a plane surface: cylindrical-wave approach," *J. Opt. Soc. Amer. A*, vol. 13, pp. 483–493, Mar. 1996.
- [16] R. Borghi, F. Frezza, C. Santini, M. Santarsiero, and G. Schettini, "Numerical study of the reflection of cylindrical waves of arbitrary order by a generic planar interface," *J. Electromagn. Waves and Appl.*, vol. 13, pp. 27–50, Jan. 1999.
- [17] A. Taflove, *Computational electrodynamics: the Finite-Difference Time-Domain method*, Artech House 3rd Edition., Norwood, MA, 2005.
- [18] M. N. O. Sadiku, *Numerical techniques in electromagnetic*, CRC Press, London, 1992.

- [19] K. S. Yee, Numerical solution of initial boundary value problems involving Maxwell's equations in isotropic media, *IEEE Transactions on Antennas and Propagation*, vol. 14, 302-307, 1966.
- [20] G. Mur, Absorbing boundary conditions for the finite-difference approximation of the time-domain electromagnetic field equations, *IEEE Transactions on Electromagnetic Compatibility*, vol. 23, 377-382, 1981.
- [21] K. S. Kunz and R. J. Luebbers, *The finite difference time domain method for electromagnetics*, CRC Press, Tokyo, 1993.
- [22] D. J. Daniels, *Ground Penetrating Radar*, 2nd edition, London, IEEE, 2004
- [23] I Moller, P.R Jakobsen, Sandy till characterized by ground penetrating radar. In Koppenjan S K, Lee H (eds.): *Ninth International Conference on Ground Penetrating Radar. Proceedings of SPIE 4758*: 308– 312, 2002.
- [24] *Guidebook on Detection Technologies and Systems for Humanitarian Demining*, GICHD, Geneva, March 2006
- [25] D.G Smith, H.M Jol, Ground penetrating radar: antenna frequencies and maximum probable depths of penetration in Quaternary sediments. – *Journal of Applied Geophysics* 33: 93–100, 1995.
- [26] J.M.H Hendrickx,., R.L. Van Dam, B. Borchers, J.O. Curtis, H.A. Lensen, and R.S. Harmon. Worldwide distribution of soil dielectric and thermal properties. in *Detection and Remediation Technologies for Mines and Minelike Targets VIII*. Orlando: SPIE 2003.
- [27] D.J. Wilson, A.W. Western, R.B. Grayson, A.A. Berg, M.S. Lear, M. Rodell, J.S. Famiglietti, R.A. Woods, and T.A. McMahon, Spatial distribution of soil moisture over 6 and 30 cm depth, Mahurangi river catchment, New Zealand. *Journal of Hydrology*. 276(1-4): p. 254-274, 2003.
- [28] Cole, K.S. and R.H. Cole, Dispersion and adsorption in dielectrics! alternating current characteristics. *Journal of Chemical Physics*. 9: p. 341-351, 1941.

- [29] P. Debye, *Polar Molecules*. New York: Dover Publ., 1929.
- [30] Jones, S.B. and D. Or, Frequency domain analysis for extending time domain reflectometry water content measurement in highly saline soils. *Soil Science Society of America Journal*. 68: p. 1568–1577, 2004.
- [31] T.J. Heimovaara, W. Bouten, and J.M. Verstraten, Frequency domain analysis of time domain reflectometry waveforms 2. A four-component complex dielectric mixing model for soils. *Water Resources Research*. 30(2): p. 201-209, 1994.
- [32] Hasted, J.B., *Aqueous dielectrics*. London: Chapman and Hall. 302, 1973.
- [33] S.S. Staff, *Soil taxonomy: A basic system of soil classification for making and interpreting soil surveys*. SCSUSDA, U.S. Gov. Print. Office: Washington, DC 1994.
- [34] F. Roth, P. van Genderen, and M. Verhaegen. Analysis of the Influence of Mine and Soil Properties on Features extracted from GPR Data. in *Detection and Remediation Technologies for Mines and Minelike Targets VI*. Orlando, FL: SPIE 2001.
- [35] T.J. Heimovaara, Frequency domain analysis of time domain reflectometry waveforms 1. Measurement of the complex dielectric permittivity of soils. *Water Resources Research*. 30(2): p. 189-199, 1994.
- [36] Sheriff, R.E., *Encyclopedic Dictionary of Applied Geophysics*. 429 ed, ed. E.F. Scherrer. Tulsa, OK: Society of Exploration Geophysicists, 2002.
- [37] Olhoeft, G.R. and S.S. Smith. Automatic processing and modeling of GPR data for pavement thickness and properties. in *GPR2000, 8th International Conference on Ground Penetrating Radar*. Gold Coast, Australia: SPIE 2000.
- [38] Stillman, D.E. and G.R. Olhoeft. EM Properties of Magnetic Minerals at RADAR Frequencies. in *Workshop on radar investigations*. Houston, TX 2005.

- [39] Iben, I.E.T., W.A. Edelstein, and P.B. Roemer, Dielectric properties of soil: application to radio frequency ground heating. General Electric Company. p. 33 1996.
- [40] H. Bohl, and K. Roth. Evaluation of dielectric mixing models to describe the $\theta(\epsilon)$ -relation. in Time Domain Reflectometry in environmental, infrastructure and mining applications. Evanston, Illinois: United States Department of Interior Bureau of Mines 1994.
- [41] A.Martinez, and A.P. Byrnes, Modeling dielectric-constant values of geologic materials: an aid to groundpenetrating radar data collection and interpretation, in Current Research in Earth Sciences. Kansas Geological Survey. p. 16 2001.
- [42] M.A. Hilhorst, C. Dirksen, F.W.H. Kampers, and R.A. Feddes, New dielectric mixture equation for porous materials based on depolarization factors. Soil Science Society of America Journal. 64: p. 1581-1587, 2000.
- [43] T.J. Heimovaara, Time domain reflectometry in soil science: theoretical backgrounds, measurements and models, in Physical Geography. Universiteit van Amsterdam: Amsterdam. p. 169 1993.
- [44] MAJ Bakker, The internal structure of Pleistocene push moraines. A multidisciplinary approach with emphasis on ground penetrating radar. PhD thesis, Queen Mary, University of London, 177 pp, 2004.
- [45] H.M. Jol, C.S. Bristow, GPR in sediments: advice on data collection, basic processing and interpretation, a good practice guide. – In Bristow C S, Jol H M (eds.) Ground penetrating radar in sediments. Geological Society, London Special Publications 211: 9– 27, 2003.
- [46] I. Moller, F. Jorgensen, Combined GPR and DC-resistivity imaging in hydrogeological mapping. – In proceedings of 11th International Conference on Ground Penetrating Radar, June 19–22, 2006, Columbus Ohio, USA, 5 pp, 2006.

- [47] R.E. Sheriff, L.P. Geldart, *Exploration Seismology*. Second Edition. Cambridge University Press, New York, 1995.
- [48] I Moller, H Vosgerau, Testing ground penetrating radar for resolving facies architecture changes – a radar stratigraphic and sedimentological analysis along a 30 km profile on the Karup Outwash Plain, Denmark. *Near Surface Geophysics* 4: 57–68, 2006.
- [49] D.G. Smith, H.M. Jol, Ground penetrating radar: antenna frequencies and maximum probable depths of penetration in Quaternary sediments. – *Journal of Applied Geophysics* 33: 93–100, 1995.
- [50] M. Beres, F.P. Haeni, Application of ground penetrating- radar methods in hydrogeologic studies. – *Ground Water* 29: 375–386, 1991.
- [51] A. Neal, Ground-penetrating radar and its use in sedimentology: principles, problems and progress. – *Earth-Science Reviews* 66: 261–330, 2004.
- [52] A. Giannopoulos, GprMax, A Ground Penetrating Radar Simulation Tool, Ver. 2.0, 2005, <http://www.gprmax.org>.
- [53] M. Balsi, M. Corcione, P. Dell'Omo, S. Esposito, and L. Magliocchetti, "Preliminary experimental validation of a landmine detection system based on localized heating and sensing," in *Proc. SPIE Defense + Security, Detection and Sensing of Mines, Explosive Objects, and Obscured Targets XIII*, Orlando, FL USA 16-20 March 2008, vol. 6953.
- [54] G. Nesti and P. Verlinde, Joint Multi-Sensor Mine-Signature Measurement Campaign Test Protocol (MsMs-Test Protocol) Annex E: Technical drawings of APL surrogates, revised 10 March 2003 by Adam Lewis (JRC), <http://demining.jrc.it/msms/>.
- [55] J. Behari, *Microwave Dielectric Behaviour of Wet Soils*, Springer: Berlin, 2005.
- [56] M. Balsi, et al., "FDTD simulation of GPR measurements in a laboratory sandbox for landmine detection", 2009 5th International Workshop on Advanced

Ground Penetrating Radar (IWAGPR 2009), University of Granada, Granada, Spain, Proc., pp. 45-49, 27-29 May 2009.

- [57] G. Nesti and P. Verlinde, Joint Multi-Sensor Mine-Signature Measurement Campaign Test Protocol (MsMs-Test Protocol) Annex E: Technical drawings of APL surrogates, revised 10 March 2003 by Adam Lewis (JRC), <http://demining.jrc.it/msms/>.
- [58] D. A. Robinson, S. B. Jones, J. M. Wraith, D. Or, and S. P. Friedman, “A review of advances in dielectric and electrical conductivity measurements in soils using Time Domain Reflectometry”, *Vadose Zone Journal*, vol. 2, pp. 444-475, 2003.
- [59] J. Behari, *Microwave Dielectric Behaviour of Wet Soils*, Berlin: Springer, 2005.
- [60] Z. Zyadal and T. Fukuda, “3D template based automatic landmine detection from GPR data”, *SICE Annual Conference 2007*, Kagawa University, Japan, Proc., pp. 1552-1557, 17-20 September 2007.
- [61] A. V. Oppenheim and R. W. Schaffer, *Discrete-Time Signal Processing*, 2nd ed., Upper Saddle River: Prentice-Hall, Inc., 1999.
- [62] N. Agmon, 1996. Tetrahedral displacement: the molecular mechanism behind the Debye relaxation in water. *Journal of Physical Chemistry* 100 (3), 1072–1080.
- [63] I.L. Al-Qadi, S. Lahouar, A. Loulizi, M.A. Elseifi, J.A. Wilkes, Effective approach to improve pavement drainage layers. *Journal of Transportation Engineering* 130 (5), 658–664, 2004.
- [64] G. Barbero, I. Lelidis, Debye's relaxation frequency: a poor man's approach. *Physics Letters A* 372 (12), 2079–2085, 2008.
- [65] G. Bekefi, A.H. Barrett, Waves in dielectrics. in *Electromagnetic Vibrations, Waves, and Radiation*. MIT Press, Cambridge, MA, pp. 426–440, 1987.
- [66] A. Benedetto,. Theoretical approach to electromagnetic monitoring of road pavement. Proc. 10th Int. Conference on Ground Penetrating Radar. Delft. The Netherlands, 2004.

- [67] A. Benedetto, F. Benedetto, GPR experimental evaluation of subgrade soil characteristics for rehabilitation of roads. Proc. IX International Conference on Ground Penetrating Radar. Santa Barbara. California. USA, 2002.
- [68] A. Benedetto, S. Pensa, Indirect diagnosis of pavement structural damages using surface GPR reflection techniques. *Journal of Applied Geophysics* 62, 107–123, 2007.
- [69] A. Benedetto, F. Benedetto, M.R. De Blasiis, G. Giunta, Reliability of radar inspection for detection of pavement damages. *International Journal of Road Material and Pavement Design*, Hermes Science 5 (1), 93–110, 2004.
- [70] A. Benedetto, F. D'Amico, F. Fattorini, Measurement of moisture under road pavement: a new approach based on GPR signal processing in frequency domain. Proc. Intern. Workshop Adv. Ground Penetrating Radar, May 2009 Granada, Spain.
- [71] A. Beneduci, Which is the effective time scale of the fast Debye relaxation process in water? *Journal of molecular liquids* 138 (1–3), 55–60, 2008.
- [72] C.F. Bohren, D. Huffman, Absorption and scattering of light by small particles. John Wiley, New York, 1983.
- [73] S. Chakraborti, Verification of the Rayleigh scattering cross section. *American Journal of Physics* 75 (9), 824–826, 2007.
- [74] J.L. Davis, A.P. Annan, Ground-penetrating radar for high resolution mapping of soil and rock stratigraphy. *Geophys. Prospect.* 37, 531–551, 1989.
- [75] B. K. Diefenderfer, K. Galal, D.W. Mokarem, Effect of subsurface drainage on the structural capacity of flexible pavement, VTRC 05-R35. Project 66818: pp. 29, 2005.
- [76] P. Drude, The theory of Optics. Longmans, Green, and Co, New York, pp. 268–396, 1902.

- [77] A. Fiori, A. Benedetto, M. Romanelli, Application of the effective medium approximation for determining water contents through GPR in coarse-grained soil materials. *Geophysical Research Letters* 32, L09404, 2005.
- [78] S.P. Friedman, A saturation degree-dependent composite spheres model for describing the effective dielectric constant of unsaturated porous media. *Resources Research* 34, 2949–2961, 1998.
- [79] K. Grote, S. Hubbard, Y. Rubin, GPR monitoring of volumetric water content in soils applied to highway construction and maintenance, *Leading Edge Exploration* 21 (5), 482–485, 2002.
- [80] K. Grote, S. Hubbard, Y. Rubin, Field-scale estimation of volumetric water content using GPR ground wave techniques. *Water Resources Research* 39 (11), 1321, 2003.
- [81] K. Grote, S. Hubbard, J. Harvey, Y. Rubin, Evaluation of infiltration in layered pavements using surface GPR reflection techniques. *Journal of Applied Geophysics* 57, 129–153, 2005.
- [82] K.C. Ho, P.D. Gader, J.N. Wilson, Improving landmine detection using frequency domain features from ground penetrating radar. *Proceedings. 2004 IEEE International Geoscience and Remote Sensing Symposium, IGARSS '04*, 3, pp. 1617–1620, 2004.
- [83] S. Hubbard, K. Grote, Y. Rubin, Estimation of nearsubsurface water content using high frequency GPR ground wave. *Leading Edge of Exploration Society of Exploration Geophysics* 21 (6), 552–559, 2002.
- [84] J.A. Huisman, S.S. Hubbard, J.D. Redman, A.P. Annan, Measuring soil water content with ground penetrating radar: a review. *Vadose Zone Journal* 2, 476–491, 2003.

- [85] T. Ishida, T. Makino, C. Wang, Dielectric-relaxation spectroscopy of kaolinite, montmorillonite, allophane, and imogolite under moist conditions. *Clays and Clay Minerals* 48 (1), 75–84, 2000.
- [86] A. Ishimaru, Theory and application of wave propagation and scattering in random media. *Proceedings Of the IEEE* 65 (7), 1030–1061, 1977.
- [87] A. Kyritsis, M. Siakantari, A. Vassilikou Dova, P. Pissis, P. Varotsos, Large low frequency dielectric constant exhibited by hydrated rock materials. *Proceedings of the Japan Academy, Series A* 77B (2), 19–23, 2001.
- [88] S. Lambot, E.C. Slob, I. van den Bosch, B. Stockbroeckx, M. Vanclooster, Modeling of ground-penetrating radar for accurate characterization of subsurface electric properties, *IEEE Transactions on Geoscience and Remote Sensing* 42, 2555–2568, 2004.
- [89] S. Lambot, L. Weihermüller, J.A. Huisman, H. Vereecken, M. Vanclooster, E.C. Slob, Analysis of air-launched ground-penetrating radar techniques to measure the soil surface water content. *Water Resources Research* 42, W11403, 2006.
- [90] T.L. Lyon, H.O. Buckman, *The Nature and Properties of Soils*, Macmillan, New York. p. 391, 1937.
- [91] R.T. Martin, Adsorbed water on clay: a review. *Clays and Clay Minerals* 9 (1), 28–70, 1960.
- [92] K.R. Maser, Condition assessment of transportation infrastructure using ground penetrating radar. *Journal of Infrastructure Systems* 2 (2), 94–101, 1996.
- [93] T. Saarenketo, T. Scullion, Road evaluation with ground penetrating radar, *Journal of Applied Geophysics* 43 pp. 119–138, 2000
- [94] A. Benedetto, Water content evaluation in unsaturated soil using GPR signal analysis in the frequency domain, *Journal of Applied Geophysics* 71, pp. 26-35, 2010